# Black Silicon optical properties, growth mechanisms andapplications

David Abi Saab

## To cite this version:

David Abi Saab. Black Silicon optical properties, growth mechanisms andapplications. Electronics. Université Paris-Est, 2015. English. NNT : 2015PESC1001 . tel-01400179

HAL Id: tel-01400179
https://theses.hal.science/tel-01400179v1
Submitted on 21 Nov 2016

Ecole Doctorale MSTIC

Mathématiques, Sciences et Technologies de l'Information et de la Communication

THÈSE

Pour obtenir le grade de

**Docteur de l'Université Paris-Est**

Specialité: Électronique, Optronique et Systèmes (CNU 63)

Présentée et soutenue publiquement par

**David ABI SAAB**

Le 04/03/2015

# Propriétés optiques, mécanismes de formation et applications du silicium noir

## Black Silicon optical properties, growth mechanisms and applications

Thèse dirigée par:

Prof. Dan E. ANGELESCU
Prof. Elodie RICHALOT

et suivie par:

Dr. Philippe BASSET

**Jury**

| | | |
|---|---|---|
| Prof. Remi DUSSART | Université d'Orléans | Rapporteur |
| Prof. Andreas TÜNNERMANN | Université Jena | Rapporteur |
| Prof. Serge BERTHIER | Université Sorbonne Paris Cité | Examinateur |
| Prof. Pere ROCA i CABARROCAS | Ecole Polytechnique | Examinateur |
| Prof. Jürgen RÜHE | Université de Freiburg | Examinateur |
| Prof. Dan E. ANGELESCU | Université Paris-Est | Directeur |
| Prof. Elodie RICHALOT | Université Paris-Est | Co-directrice |
| Dr. Philippe BASSET | Université Paris-Est | Encadrant de thèse |
| Dr. Shermila MOSTARSHEDI | Université Paris-Est | Invitée |

# Acknowledgements

This thesis was realised within the teams "Sensors and Microsystems" at ESIEE Paris and "Electromagnetic applications and measurements" at Université Paris-Est Marne-la-Vallée, both research teams belonging to ESYCOM Laboratory at Université Paris-Est.

First, I would like to acknowledge the MSTIC doctoral school of Université Paris-Est for their financial support and the ESYCOM Laboratory Committee for supporting my candidature.

I would like to offer my sincerest gratitude to my advisors Prof. Dan E. Angelescu and Prof. Elodie Richalot, for allowing me to be part of their research teams, for sharing their precious knowledge and providing their continuous support, guidance and motivation, crucial for the completion of this manuscript.

I would like to thank my supervisor Dr. Philippe Basset for introducing me to the world of MEMS and providing his enormous help and guidance throughout the thesis.

I offer my gratitude to Prof. Matthew Trawick of University of Richmond, for sharing his knowledge on microscopy and image processing and his enormous support while performing the three-dimensional reconstruction of Black Silicon samples and the formation simulation model.

I extend my thanks to Dr. Shermila Mostarshedi for her time and effort during the investigation on the electromagnetic simulation modelling techniques of black silicon.

I also extend my gratitude to Prof. Tarik Bourouina for his useful discussions and advice during the research and elaboration of the manuscript.

I would like to thank Prof. Serge Berthier and his PhD student Magali Thome from the Nanoscience institute of Paris (INSP) for their support in the optical constants measurements of the black silicon samples.

I would like to thank Prof. Pere Roca i Cabarrocas from the Ecole Polytechnique, for his useful discussions and advice during the initial fabrication steps of the Black Silicon photovoltaic cell.

I offer my sincere gratitude to the Reviewers and Examiners for taking their valuable time to read the manuscript and accepting to be part of the jury.

A special thanks goes to Frédéric Marty for his support on the Black Silicon samples fabrication with the reactive ion etcher, Bruno Mercier for providing the formation on the scanning electron microscope and Stéphane Protat for his support with the electromagnetic

simulation software.

I offer my gratitude to all members of the Sensors and Microsystems team at ESIEE Paris and the Electromagnetic Applications and Measurements team at Université Paris-Est Marne-la-Vallée, particularly to my colleagues: Dr. Kim Nguyen, Dr. Jayalakshmi Parasunaman, Dr. Julien Pagazani, Dr. Noha Gaber, Dr. Francesco Cottone, Dr. William Cesar, Sebastian Wahl, Maíra Pôssas Abreu and Dr. Myline Cottance for their kindness, support and the good moments shared. I also extend my gratitude to Dr. Thierry Alves and Dr. Rafael Quiroz from Université Paris-Est Marne-la-Vallée, Dr. Carlos Viana and Dr. Oscar Gomez from ESIEE Paris and Dr. Hamlet Medina from ParisTech for their friendship and support.

Finally, I would like to thank all my family and friends, specially my parents, my brother and sisters for being my source of inspiration: Jacinto, Glenda, Maria Gabriela, Elizabeth, Atilano and Maria Alejandra.

# Résumé

## Chapitre 1. Introduction

Dans ce chapitre, nous présentons l'état de l'art de plusieurs aspects du silicium micro/nano structuré, aussi appelé silicium noir (BSi), tels que ses méthodes de fabrication, applications, méthodes de caractérisation, la modélisation optique et la modélisation de sa formation. Les chapitres suivants présentent les contributions de ce manuscrit à l'état de l'art.

**Méthodes de fabrication du BSi:** Les méthodes de fabrication du BSi sont classées en trois catégories: la gravure à base de plasma, la gravure humide et la gravure laser-chimique. Dans la gravure à base de plasma, des ions et des radicaux (formés à partir des composés gazeux) sont projetés sur l'échantillon pour produire une gravure chimique, physique ou la combinaison des deux. Les différentes techniques de gravure à base de plasma peuvent être classées selon le procédé de génération des ions, l'accélération des ions vers la plaquette, les composés gazeux utilisés et la configuration de la chambre [1]. La fabrication du BSi par gravure humide implique l'utilisation d'une solution liquide pour graver l'échantillon combinée avec des techniques supplémentaires pour obtenir une gravure anisotrope des structures submicrométriques. Un autre procédé de fabrication du BSi a été démontré en utilisant des impulsions laser de courte durée (100 fs) et avec une densité d'énergie de 10 $kJ/m^2$ [2]. Bien que ce procédé a besoin de la présence des composés gazeux pour la gravure du silicium (telles que $SF_6$ ou $Cl_2$), le substrat n'a pas besoin d'être sous vide comme dans les techniques de gravure par plasma.

**Applications du BSi:** La première application proposée après la présentation de la structuration du silicium pour obtenir des surfaces avec faibles réflectances [3], comprend l'amélioration de l'efficacité (PCE) des cellules solaires. Une cellule solaire à simple jonction utilisant du silicium microstructuré a été fabriquée sur un substrat polycristallin, avec une PCE obtenue de 17.1%, offrant une augmentation de 0.7% par rapport à une cellule solaire de surface structurée en utilisant la photolithographie [4]. Une autre propriété intéressante mentionée est l'augmentation du coefficient d'absorption dans la lumière visible et proche infrarouge [5]. La capacité d'absorber plus de lumière avec des substrats minces a conduit à des nouvelles techniques de conception de cellules solaires sur films minces pour réduire les coûts de fabrication [6]. Une grande amélioration de la sensibilité en proche infrarouge en utilisant un photodétecteur à base du BSi a été aussi démontrée [7]. À partir de mesures de l'activité catalytique, la surface totale du BSi peut être 10 fois plus élevée qu'une surface plane de mêmes dimensions [8], ce qui implique que les surfaces BSi ont de grandes applications potentielles dans la miniaturisation des dispositifs utilisés pour les réactions catalytiques et les capteurs. En raison de sa topographie complexe composée de structures denses avec de forts rapports d'aspect (HAR), le BSi est une technique efficace pour créer des surfaces super-hydrophobes avec de nombreuses applications telles que des structures autonettoyantes [9] ou des supports de gouttelettes liquides utilisés dans les capteurs microélectromécaniques [10], actionneurs électrostatiques [11] et systèmes optiques [12]. Récemment, des cellules solaires autonettoyantes ont été obtenues par la combinaison de la faible réflectivité et des propriétés hydrophobes d'une surface nanostructurée [9].

**Caractérisation du BSi:** Les méthodes actuelles utilisées pour caractériser et d'obtenir des représentations précises en trois dimensions des nanostructures HAR (tels que le BSi) présentées dans ce manuscrit comprennent l'imagerie par microscope électronique à balayage (MEB) à différents angles de vue, la reconstruction tridimensionnelle à partir de l'analyse des niveaux de gris et la nanotomographie de faisceau d'ions focalisé (FIB). L'imagerie MEB est la méthode la plus utilisée pour caractériser la topographie des échantillons du BSi. Des images MEB du BSi en vue de dessus peuvent être utilisées pour estimer le diamètre et la séparation moyenne des structures, des images en vue de coupe permettent d'estimer la hauteur des structures et des images en vues inclinées donnent une idée générale sur la forme des structures et leur uniformité. Le rapport d'aspect des structures est déduit de la hauteur et du diamètre des structures. Dans des études antérieures où des caractérisations du BSi ont été faites, la mesure de la séparation moyenne, la hauteur et le diamètre des structures est basée sur des images MEB avec différents angles de vue [13]. L'analyse du niveau de gris est une technique de reconstruction à partir de laquelle un modèle en trois dimensions qui représente la topographie de la surface des échantillons du BSi peut être obtenu. Cette méthode comprend la déduction de la hauteur des structures en fonction du niveau de gris d'une image MEB en vue de dessus. En utilisant les valeurs connues de hauteur pour les niveaux plus brillant et plus sombre de l'image MEB, les hauteurs intermédiaires peuvent être déduites par interpolation linéaire. L'analyse des niveaux du gris a été effectivement utilisée dans la reconstruction d'échantillons BSi [14]. Toutefois, il existe certaines limites sur la profondeur maximale du trou détectable en raison de la gamme dynamique limitée de l'appareil MEB. Par conséquence, alors que l'analyse des niveaux de gris peut donner des informations précises sur la topographie, elle est limitée à des échantillons BSi avec des rapports d'aspect petits ou moyens. La nanotomographie FIB combine les capacités de gravure contrôlables du FIB et les capacités d'imagerie non destructive du MEB dans le même processus. Elle comprend des étapes alternées de gravure FIB et d'acquisitions des images MEB réalisées sur un échantillon afin d'obtenir une série d'images en coupe à différents niveaux de gravure. Un traitement ultérieur de la série des images MEB permet la reconstruction d'une représentation en trois dimensions de l'échantillon BSi. Cette technique offre une résolution nanométrique du même ordre que les images MEB ($<$ 10 nm sur un échantillon de $>$ 20 x 20 $\mu$m) sur deux axes, et sur le troisième axe avec une résolution qui dépend de la longueur de chaque pas de la gravure ($\sim$ 10 nm) et de l'intervalle d'acquisition des images MEB. La nanotomographie FIB a été utilisée dans des nombreuses applications telles que la caractérisation d'alliages métalliques, de surfaces poreuses, la reconstruction d'un tissu biologique, et autres [15].

**Modélisation optique du BSi:** Les méthodes utilisées pour calculer les constantes optiques des échantillons micro/nano structurées comprennent la méthode des différences finies dans le domaine temporel (FDTD), la méthode des éléments finis (FEM) et l'analyse rigoureuse d'ondes couplées (RCWA). Chaque méthode a ses avantages et ses limites, mais en général les trois méthodes sont capables de calculer des paramètres optiques tels que la réflectance totale, la transmittance et l'absorbance sur des structures tridimensionnelles arbitraires. Afin de simuler de grandes surfaces micro/nano-structurées avec une de ces méthodes, il faut modéliser une cellule unitaire qui représente la figure prédominante dans la surface, tels qu'un cylindre, une pyramide, un cône, etc. Des conditions aux limites périodiques sont imposées dans cette cellule élémentaire pour représenter une grande surface périodique. Des valeurs de la partie réelle et imaginaire de la permittivité relative des matériaux en fonction de la fréquence sont nécessaires pour la modélisation. Lorsque que la surface nano-structurée est apériodique (tel que le BSi) avec des variations de la séparation entre les structures, une cellule unitaire peut être modélisée en se basant sur une partie réelle de la topographie [16, 17]. Cependant, les dimensions de la cellule unitaire peuvent être limitées par les ressources de calcul disponibles dans certaines méthodes numériques. Une autre approche pour déterminer les paramètres optiques d'une structure apériodique est de modéliser une cellule équivalente simple obtenue à partir de l'analyse statistique d'une grande région de la surface et qui prenne en compte la topographie irrégulière [18].

**Modélisation de la formation du BSi:** Bien que les effets de chaque paramètre de la cryo-DRIE sur la formation du BSi aient déjà été décrits, ainsi que les interactions moléculaires entre les plasmas et le substrat qui permettent la formation de microstructures, le mécanisme par lequel une topographie complexe tel que BSi peut être générée à partir d'une surface plane n'est actuellement pas bien comprise. De multiples hypothèses ont été proposées concernant les mécanismes de la formation initiale du BSi, tels que des micromasques formés par l'oxyde natif sur silicium ou des impuretés [16, 19, 20], ou en raison de ré-dépôt des produits réactifs dans certains endroits qui renforce la couche de passivation [21].

## Chapitre 2. La reconstruction de la topographie et la caractérisation du BSi

Dans ce chapitre, nous présentons des résultats expérimentaux obtenus à partir de différentes techniques de reconstruction tridimensionnelle d'échantillons de BSi, comprenant la conversion des niveaux du gris à partir des images de microscope électronique à balayage (MEB) et de la nanotomographie de faisceau d'ions focalisé (FIB).

Nous présentons également une nouvelle méthode plus simple pour obtenir une reconstruction tridimensionnelle précise d'échantillons BSi basée sur la nanotomographie FIB, avec une préparation minimale des échantillons et sans l'exigence d'un dépôt de couche de contraste. L'avantage de cette technique est qu'elle conduit à la délocalisation de la direction du faisceau de gravure à un angle perpendiculaire aux structures (ou parallèle au plan du substrat), ce qui réduit les exigences de résolution dans la direction de gravure en raison du rapport d'aspect élevé des structures.

En comparant les reconstructions de modèles tridimensionnelles des échantillons du BSi avec leurs images MEB pour différents angles de vue, nous démontrons que la nanotomographie FIB peut être utilisée pour des reconstructions précises des échantillons complexes avec des grands rapports d'aspect. Cette méthode supprime la limitation sur le rapport d'aspect qui est inhérent à toutes les méthodes de reconstruction tridimensionnelles par la conversion des niveaux du gris à partir des images MEB en raison de la gamme dynamique qui est limitée dans les détecteurs. La nanotomographie FIB fournit des informations extrêmement précises sur la profondeur de trous profonds et étroits typiques dans les échantillons du BSi, mais avec l'inconvénient de la destruction de l'échantillon pendant le processus de gravure par FIB. La marge d'erreur observée sur la profondeur du trou, étant liée à l'intervalle d'acquisition des images MEB, est autour de

100 nm pour nos expériences.

En utilisant des modèles tridimensionnels obtenus par nanotomographie FIB, nous calculons les paramètres topographiques du BSi tels que les histogrammes de la hauteur et de l'espacement des structures, le rapport entre les surfaces de silicium et d'air en fonction de la hauteur, la moyenne du rapport d'aspect des structures et la surface d'échange avec l'air. Des mesures de la surface totale des échantillons de BSi montre qu'elle peut atteindre des valeurs dix fois supérieures à celles d'une structure plane, de sorte que le BSi peut avoir des implications importantes dans la fabrication de microréacteurs catalytiques, où une meilleure zone de contact peut fournir une amélioration importante de l'efficacité.

Avec l'analyse des images obtenues à partir de la nanotomographie FIB, on montre que les échantillons BSi sont formés par la génération de trous cylindriques arrondis, qui sont gravés dans le substrat du silicium à des profondeurs différentes comme s'ils étaient réalisés par une "nano-perceuse". Les aiguilles observées dans les échantillons du BSi représentent donc la différence entre le volume initial de la surface du silicium et l'union de tous les trous gravés.

## Chapitre 3. Caractérisation optique du BSi

Nous étudions aussi l'influence de la topographie du BSi sur ses propriétés optiques de surface. Tout d'abord, nous fournissons des résultats expérimentaux sur les constantes optiques des échantillons BSi telles que leur réflectance hémisphérique, la transmittance et l'absorbance mesurées avec un spectromètre et une sphère d'intégration. Nous présentons ensuite les différentes méthodes de modélisation de cellules unitaires du BSi utilisées pour la simulation de la réflectance et la transmittance avec la méthode des éléments finis et deux méthodes de homogénéisation différents. Pour ces cellules unitaires basées soit sur la topographie réelle du BSi soit sur une figure équivalente, les dimensions choisies et la forme sont conformes à une analyse statistique réalisée sur une large région de l'échantillon BSi, pour obtenir une meilleure concordance entre les simulations et les données expérimentales.

La première technique, basée sur des simulations numériques de cellules unitaires sur la base de régions de la topographie réelle du BSi, fournit une concordance partielle avec les mesures à certaines longueurs d'onde mais avec des tendances différentes. Les différences dans la réponse en réflectance entre les régions sont attribuées à la taille limitée de la structure simulée.

La deuxième technique de modélisation, basée sur une structure équivalente bipériodique constituée d'une seule figure (cône, cône inversé, etc.), montre une meilleure concordance entre les réflectances simulées par rapport à des mesures lorsque la distribution de la hauteur est similaire à la distribution globale de la hauteur du BSi (ex. cône inversé). En particulier, on a obtenu une meilleure concordance lorsque la hauteur de la structure équivalente est basée sur l'écart type de la hauteur globale du BSi, par rapport au cas où la hauteur est fonction de la profondeur moyenne globale ou de l'angle moyen de la surface normale. Ce résultat suggère que, en utilisant l'écart type de la hauteur, il compense les fortes variations locales de la hauteur moyenne observée dans la topographie du BSi.

Dans la troisième technique de modélisation, des cellules unitaires composées de quatre cônes inversés sont utilisées afin d'introduire des variations de la hauteur et du diamètre de la structure et éviter les effets provoqués par les cellules unitaires parfaitement périodiques, et donc augmenter la ressemblance avec la topographie réelle du BSi. Les résultats obtenus montrent une amélioration de la tendance lisse observée dans les mesures, alors que la réflectance moyenne n'est pas modifiée puisque la cellule est conçue avec le même moyenne et écart type de la hauteur que utilisée dans la cellule unitaire d'une seule figure. Les deux configurations des cellules multi-structurées simulées fournissent environ la même réponse de réflectance avec un écart-type normalisé par rapport aux mesures expérimentales inférieur à 0.25%, étant évalué pour des longueurs d'onde entre 450 nm et 950 nm. Les variations résiduelles représentent le compromis entre la simplicité de la conception et la précision de la cellule équivalente. La cellule unitaire multi-structurée donne huit degrés de liberté ce qui permettrait d'avoir des distributions de hauteurs plus proches de celles mesurées à partir des échantillons du BSi, ce qui impliquerait une amélioration supplémentaire de la réflectance par rapport à des mesures.

La réflectance spéculaire obtenue à partir des approximations des structures multicouches, en utilisant des modèles d'homogénéisation basés sur le rapport des surfaces silicium–air et la capacité synthétisée, montre un accord amélioré entre simulations et mesures quand nous utilisons le rapport silicium–air mesuré à partir de surfaces réelles du BSi obtenus par nanotomographie FIB. L'utilisation de cette méthode d'homogénéisation permet de gommer l'effet de la périodicité introduite de façon artificielle lors de la simulation d'une structure composée de cônes inversés, alors que la structure réelle n'est pas périodique mais désordonnée.

La faible réflectance obtenue pour une large gamme d'angles d'incidence, observée dans les simulations des cellules unitaires multi-structurées et la cellule simple, suggère que des surfaces avec une distribution de structure désordonnée et des hauteurs différentes (tels que le BSi) sont préférables dans le cas où des réflectances faibles sont nécessaires sur une large gamme d'angles de incidence, par rapport aux surfaces avec des structures parfaitement périodiques et de même hauteur.

## Chapitre 4. Aspects statiques et dynamiques de la formation du BSi

Nous présentons un modèle capable de simuler l'évolution de la topographie du BSi à partir d'un substrat plat, en concordance avec des données obtenues expérimentalement. L'évolution observée du BSi à partir d'un substrat plat peut être modélisée avec précision en incluant les effets non locaux de l'occlusion géométrique (ou auto-ombrage). À notre connaissance, c'est la première tentative réussie de modéliser la formation de structures à haut rapport d'aspect. La combinaison des données expérimentales et des simulations obtenues avec ce modèle nous a permis d'expliquer certaines des propriétés du BSi, et de mieux comprendre les mécanismes derrière sa formation par la cryo-DRIE.

Bien que de nombreux paramètres de la cryo-DRIE aient des effets directs ou indirects sur la formation de BSi, le modèle se concentre sur les trois principaux processus qui se produisent: la formation d'une couche de passivation, la gravure de la couche de passivation et la gravure du silicium. Ces processus, qui se produisent simultanément dans la cryo-DRIE, sont discrétisés dans le modèle par incréments de temps infinitésimaux, jusqu'à ce que le temps du procédé préétabli soit atteint. Les données du modèle sont enregistrées dans deux matrices bidimensionnelles correspondant à la hauteur du substrat de silicium (avec des valeurs initiales imposées par la géométrie de substrat choisi), et, respectivement, l'épaisseur de la couche de passivation, mesurée normale au substrat (généralement avec une valeur initiale nulle). Parce que la fonction de la hauteur a une valeur unique, des structures saillantes (que nous n'observons jamais expérimentalement) ne peuvent pas être modélisées avec cette approche.

Différentes topographies initiales du substrat ont été utilisées: des surfaces du silicium poli avec une rugosité résiduelle basée sur la caractérisation par microscopie à force atomique (AFM) et des modèles tridimensionnels du BSi à des stades initiaux de gravure obtenus par l'analyse des niveaux du gris des images MEB. À partir de l'analyse AFM des plaquettes du silicium poli, une variation de hauteur moyenne $\sim$0.5 nm a été rapportée [22], qui correspond à la valeur typique utilisée dans notre modèle.

Avec ce modèle, nous étudions les aspects statiques de la formation du BSi tels que l'influence de la variation des paramètres du procédé de simulation dans les structures du BSi obtenues pendant un temps de gravure fixe, et des calculs des rapports des surfaces silicium–air en fonction de la hauteur. En faisant varier la vitesse de passivation $v_{\mathrm{pe}}$ et la vitesse de gravure de la couche de passivation $v_{\mathrm{pf}}$ et avec une valeur fixe de vitesse de gravure du silicium $v_{\mathrm{Si}}$ et du temps de procédé $t_{\mathrm{proc}}$, nous simulons la gravure des structures BSi à partir de surfaces planes avec différentes conditions de plasma. La variation de $v_{\mathrm{pf}}$ est analogue à un changement du rapport de débits des gaz $O_2/SF_6$ dans le plasma et les variations de $v_{\mathrm{pe}}$ est analogue à un changement dans le potentiel (bias). Afin de récupérer les combinaisons de $v_{\mathrm{pe}}$ et $v_{\mathrm{pf}}$ qui produisent du BSi, nous faisons un diagramme de phase avec les calculs du rapport d'aspect de la surface. La zone où des rapports d'aspect élevés sont obtenus définit la zone où le BSi est formé. Avec ce diagramme de phase, nous sélectionnons plusieurs conditions de formation du BSi pour observer la formation de la structure à différentes valeurs de $v_{\mathrm{pf}}$. Nous comparons les vues en coupe des résultats de simulation à différentes valeurs de $v_{\mathrm{pf}}$ avec des images MEB d'une étude paramétrique précédente, où l'effet du rapport de débits $O_2/SF_6$ sur la topographie résultante du BSi a été mesurée [13]. Nous observons dans les simulations et expériences que le BSi obtenu dans un processus avec de faibles débits d'oxygène (basse $v_{\mathrm{pf}}$) comprend des structures pointues avec des rapports d'aspect élevés, qui deviennent progressivement moins profondes et plus arrondies quand le débit d'oxygène (ou, de façon analogue, $v_{\mathrm{pf}}$) est augmenté. Le modèle montre aussi que la phase du BSi disparaît pour des combinaisons des grandes valeurs du $v_{\mathrm{pe}}$ et $v_{\mathrm{pf}}$, ce qui suggère que le passage progressif de sans gravure au comportement de gravure uniforme est possible sans la phase du BSi intermédiaire.

Le deuxième aspect statique de la formation du BSi comprend la comparaison du rapport Silicium–air *vs.* hauteur entre les échantillons réels du BSi (obtenus par nanotomographie FIB) et les surfaces BSi simulées, montrant un bon accord et prouvant que la géométrie du BSi simulée fournit, en effet, une transition très lisse entre silicium et air. Cette transition est une conséquence directe des structures du BSi, comprenant une combinaison d'"aiguilles" pointues en haut et de "trous" arrondis au fond, avec hauteurs et profondeurs différentes.

Pour mieux comprendre les mécanismes de formation du BSi, deux études dynamiques ont était réalisées. Nous avons d'abord simulé l'évolution de la géométrie BSi *vs.* $t_{\mathrm{proc}}$, suivi par une série de simulations avec des structures initiales qui comprennent des modèles tridimensionnels du BSi à des stades initiaux de gravure, obtenues avec des traitements du substrat du silicium par la cryo-DRIE sur une courte période. Nous simulons l'évolution de la géométrie du BSi avec le temps, à partir d'un substrat initial plat. Nous trouvons un bon accord entre les surfaces simulées et les mesures réelles effectuées sur des échantillons différents par la cryo-DRIE avec différents temps de processus, en comparant des images MEB avec différents angles de vue [13]. Dans ce cas particulier, nous observons dans l'expérience et la simulation que du BSi apparaît après quelques minutes de temps de traitement, et son rapport d'aspect augmente rapidement au cours des minutes suivantes avant de finalement se stabiliser. Les simulations révèlent la structure détaillée du BSi à différents stades de son évolution: au $t_{\text{proc}} = 7$ min, la taille de la rugosité initiale est amplifiée par un facteur d'environ 20, suivie par la génération d'un réseau de trous sur la surface plane, qui se développe et devient plus dense alors que les trous sont gravés progressivement plus profondément dans le substrat. Quelques minutes après, toutes les parties plates du substrat sont gravées, laissant apparaître le réseau d'aiguilles caractéristique du BSi, en cohérence avec les observations expérimentales [13, 16]. Simultanément, les trous initiaux continuent d'être gravés plus profondément dans le substrat, ce qui provoque la géométrie observée dans la partie inférieure des structures du BSi. Finalement, le rapport d'aspect a tendance de se stabiliser vers une configuration équilibrée des taux de gravure des trous et des aiguilles. Le rapport d'aspect final que nous pouvons obtenir dépend du processus.

Dans la deuxième étude dynamique, nous utilisons des modèles tridimensionnels du même échantillon traité à des étapes partielles de gravure cryo-DRIE de courte durée, obtenus par l'analyse des niveaux de gris des images MEB vues de dessus. Nous effectuons des simulations avec ces topographies initiales, au lieu de surfaces polies, qui ont certaines structures déjà formées. Cette procédure nous permet d'observer, de façon dynamique, comment la gravure se produit sur un échantillon qui a déjà développé du BSi et nous permet de comparer les résultats avec des échantillons réels en comparant les endroits où la gravure se produit. Après l'introduction de l'échantillon initial du BSi, nous simulons la cryo-DRIE pendant le temps nécessaire pour atteindre l'étape suivante. La topographie des modèles de simulation résultante est ensuite comparée avec des images MEB obtenues expérimentalement, montrant une remarquable ressemblance. Nous notons également que le modèle est capable de reproduire la formation préférentielle de nouveaux trous, qui a été observée dans certaines régions des images MEB, et l'évolution de nouveaux trous formés aux points de selle topographique.

Après avoir expliqué les méthodes de calcul des trois procédés différents qui se produisent simultanément dans la cryo-DRIE, nous décrivons comment l'instabilité fournies par la combinaison de ces différents processus peut conduire à la formation du BSi et les nouveaux points de gravure sur des monticules formés précédemment. La phénoménologie observée peut être expliquée par le fait que la surface plane initiale de l'échantillon du silicium est instable à la formation de trous selon la cryo-DRIE puisque la gravure de la couche de passivation est anisotrope (bombardement ionique), et donc pas affectée par la formation de trous, tandis que la formation de la couche de passivation se produit par la diffusion au fond des trous. Les fonds des trous subissent une passivation réduite, et donc la condition de gravure est effectivement déplacée vers un régime de gravure uniforme. Par ailleurs, les sommets des aiguilles sont fortement passivés par leur exposition aux composants de passivation diffus, alors que l'exposition aux composants de gravure restent essentiellement inchangée. Cela pousse la condition de gravure pour les sommets des aiguilles vers un régime lent (ou inexistant) de gravure. Cependant, sur un échantillon qui a déjà développé la topographie du BSi caractéristique, les points de selle sont les seules régions où les taux de croissance de passivation et gravure effectives sont équilibrés, ce qui permet la formation de nouveaux trous et explique la densification observée des motifs de trous avec le temps.

## Chapitre 5. Fabrication d'une cellule solaire basée sur le BSi

Pour finir, nous présentons le processus de fabrication d'une cellule solaire qui incorpore du BSi sur sa surface avant afin de réduire la réflectance de la surface pour de grands angles d'incidence et augmenter son efficacité. Le développement de cette cellule est un objectif partiel pour démontrer la faisabilité d'une cellule solaire autonettoyante qui combine les propriétés hydrophobes/hydrophiles du BSi et sa faible réflectance afin de fournir une cellule qui puisse maintenir son efficacité dans le temps avec des interventions minimales. Nous commençons par la caractérisation du substrat comprenant les mesures de la durée de vie des porteurs minoritaires et la caractérisation de la profondeur de jonction par spectroscopie des ions de masse secondaire. Ensuite, nous présentons les étapes de fabrication du dispositif avec les dimensions optimisées basées sur des simulations avec un logiciel de modélisation des cellules solaires (PC1D), des rapports précédents trouvés dans la littérature et le savoir-faire fourni par plusieurs groupes de recherche. La fabrication réelle n'était pas possible au cours de la période de cette thèse.

# Contents

This page intentionally left blank

# List of Figures

This page intentionally left blank

# List of Tables

This page intentionally left blank

# List of Abbreviations

| | |
|---|---|
| **AFM** | Atomic force microscopy |
| **ALD** | Atomic layer deposition |
| **AR** | Aspect ratio |
| **BSi** | Black Silicon |
| **cryo-DRIE** | Cryogenic deep reactive ion etching |
| **CVD** | Chemical vapour deposition |
| **DRIE** | Deep reactive ion etching |
| **FDTD** | Finite-difference time-domain |
| **FEM** | Finite element method |
| **FIB** | Focused ion beam |
| **HAR** | High aspect ratio |
| **ICP** | Inductively coupled plasma |
| **MEMS** | Micro-electro-mechanical systems |
| **NEMS** | Nano-electro-mechanical systems |
| **NRMSE** | Normalised root mean squared error |
| **PCE** | Power conversion efficiency |
| **PSD** | Power spectral density |
| **RCWA** | Rigorous coupled-wave analysis |
| **RF** | Radio frequency |
| **RIE** | Reactive ion etching |
| **SE** | Secondary electrons |
| **SEM** | Scanning electron microscope |
| **SIMS** | Secondary ion mass spectrometry |
| **STD** | Standard deviation |

This page intentionally left blank

# Chapter 1

# Introduction

**Contents**

## 1.1 State of the art

A large amount of research has been conducted into micro/nano-textured surfaces because of the interesting properties provided by their topography independently of their material composition. Such properties include their optical reflectance and water repelling capability that drastically change in micro/nano-textured surfaces compared to untreated or polished surfaces. It is believed that taking advantage of these properties, they can lead to the improvement of the evolving requirements of miniaturized systems and sensors, as well as solar cells.

By texturing a surface with micro/nano-structures, it is possible to reduce its optical reflectance to low values, below 1%. This reflectance reduction has been studied since several decades in materials such as Silicon (Si), obtained after a texturization process resulting in an array of densely-packed high aspect ratio (AR) micro/nano-structures [3]. The reflectance is reduced when the width of the structures are in the same order of magnitude of the visible light wavelengths or smaller; this effect can be interpreted as a result of the multiple wave scattering induced by the rugosity diffraction [23] or the smooth transition between the air and the silicon substrate achieved through surface patterning [24]. Many dark surfaces have been produced with different texturing methods such as electro-deposition and sputtering, using different materials other than silicon such as: aluminium, nickel, beryllium, graphite and many others. [25]. Up to this date, the darkest manufactured surface consists of vertically aligned carbon nanotubes with a 0.045% total reflectance reported [26].

Silicon is currently one of the preferred materials used in the development of micro/nano electromechanical systems (MEMS and NEMS), due to its availability and to well-established fabrication processes and modelling techniques. Several forms of micro/nano-textured silicon surfaces with near-zero reflectance have been demonstrated, such as periodic arranged silicon nanopillars patterned with soft-imprint lithography [27], high AR periodic nanowires obtained by a specialized metal evaporation patterning technique [28] and maskless formation of randomly arranged silicon needle-like micro/nano-structures also known as black silicon (BSi) [19].

In contrast to lithography-based patterning techniques, BSi surfaces are the result of a self-patterning generation of disordered needle-like high AR subwavelength structures, obtained at special process conditions on non-masked silicon surfaces. The reflectance of BSi surfaces is reduced over a broad wavelength and angles of incidence range, and the surfaces appear black when directly observed. Due to the submicrometer size of BSi structures, they can only be observed with devices such as a scanning electron microscope (SEM). The shape, dimensions and the spacing of these structures may vary according to the fabrication method used, which also has an effect on the reflectance behaviour at visible light wavelengths as previously demonstrated in simulations and measurements [13, 29].

In this introductory Chapter we review several aspects of BSi surfaces obtained from a thorough bibliography study, such as its fabrication methods, applications, topography characterization methods, modelling techniques for optical simulations, and growth mechanisms. We also describe the contributions that this thesis brings to the state of the art: a better understanding of BSi topography, optical behaviour and insights into its formation mechanism.

### 1.1.1 BSi fabrication

A wide variety of techniques employed to fabricate BSi have been demonstrated, which can be classified in three general categories: plasma-based etching, wet etching and laser-chemical etching.

#### 1.1.1.1 Plasma-based etching

In plasma-based etching, ions and radicals (formed from gaseous compounds) are projected to the sample to produce reactive etching, ion milling or the combination or both. The different plasma-based etching techniques can be classified according to the method of ions generation, ions acceleration towards the wafer, the gaseous compounds used and the chamber configuration [1]. The first reports of low reflectance surfaces produced by mask-less silicon patterning were obtained by sputtering-etching and reactive ion etching (RIE) [3, 30].

- Conventional Reactive Ion Etching (RIE)

RIE is a plasma-based etching method used in MEMS and integrated circuit (IC) fabrication, where the ions generation and acceleration towards the wafer are controlled with the same radio frequency (RF) power source. There are several combinations of gas compounds used in RIE, one example being the use of sulphur hexafluoride $SF_6$ for silicon etching, oxygen $O_2$ that generates a conformal passivation layer and fluoroform $CHF_3$ used for the directional passivation layer etching [19].

In order to find the right amount of each gas flow that provides anisotropic etching with vertical profiles on masked Si wafers, a method was proposed called “the black silicon method” [19], from which the name “black silicon” originated. This method consists of, while maintaining the other process parameters fixed, gradually increasing the oxygen flow until BSi is observed (since BSi is formed in overpassivating regimes), followed by slightly decreasing the oxygen flow until the BSi is not longer observed. The oxygen gas flow obtained when BSi is not longer observed provides the calibration point for vertical profile anisotropic etching.

Based on the influence of the temperature in the anisotropy of the etching profile [31], BSi fabrication by RIE, using $SF_6/O_2$ plasmas at low and cryogenic temperatures (cryogenic RIE), was demonstrated [20, 32].

The molecular interactions during BSi formation in $SF_6/O_2$ based plasmas in cryogenic RIE have been previously described [20, 32]: the plasma mixture produces $SF_x^+$ ions and $F^*$ radicals, which diffuse to the substrate producing an isotropic chemical etching reaction on Silicon. Simultaneously, the $O^*$ radicals produced by oxygen also diffuse to the substrate creating a passivation layer $Si_xO_yF_z$ that protects the silicon from being etched (the formation of the passivation layer being enhanced at cryogenic temperatures). While this layer cannot be removed by the $F^*$ radicals, it is sensitive to physical directional etching by the $SF_x^+$ ions. Due to the ions' trajectory, the etching is stronger on horizontal surfaces than on vertical walls. When the passivation layer formation and etching rates are only slightly different (controlled by the $SF_6/O_2$ gas flow ratio), the competition between the two processes leads to anisotropic etching and the formation of high aspect ratio (HAR) structures such as BSi. A schematic of BSi formation process is shown in Figure 1.1.

The initial appearance of BSi structures in a cryogenic RIE process (with gas compounds consisting of $SF_6/O_2/CHF_3$ or $SF_6/O_2$ at cryogenic temperatures) was attributed to micromasking produced by native oxide and dust, followed by the formation of needles due to the isotropic passivation layer growth combined with directional etching [19, 20].

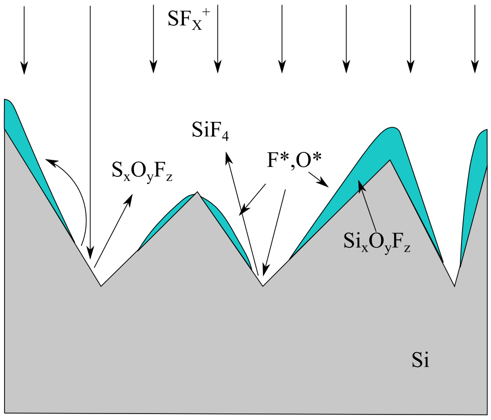

**Figure 1.1.** BSi formation by RIE (reproduced from [20]).

- Inductively coupled plasma Reactive Ion Etching (ICP-RIE)

Current plasma-based techniques to produce BSi with very high aspect ratios involve the use of an inductively coupled plasma (ICP) RIE chamber (Figure 1.2). In ICP-RIE the generation of ions and their acceleration towards the sample are controlled independently by the ICP RF power and the voltage bias. Two BSi formation methods used with ICP-RIE are: Continuous deep reactive ion etching at cryogenic temperatures (cryo-DRIE) [21, 33] and, respectively, time-multiplexed deep reactive ion etching also called the “Bosch” process (DRIE-Bosch) [34].

In cryo-DRIE, the usual gas compounds consist of $SF_6$ to etch the silicon, $O_2$ that forms a conformal passivation layer at cryogenic temperatures, and the directional etching of the passivation layer is controlled with the adjustable voltage bias. DRIE-Bosch is, by contrast, performed at ambient temperatures and uses a discretized series of etching and passivation steps: $SF_6$ gas is used in the etching step and octofluoro cyclobutane $C_4F_8$ is used in the passivation deposition step. In the DRIE-Bosch technique, the possibility to adjust the duration of the time steps provides greater control on the anisotropic etching profile; however, the discontinuity between passivation and etching steps may result in a scalloping effect in vertical walls.

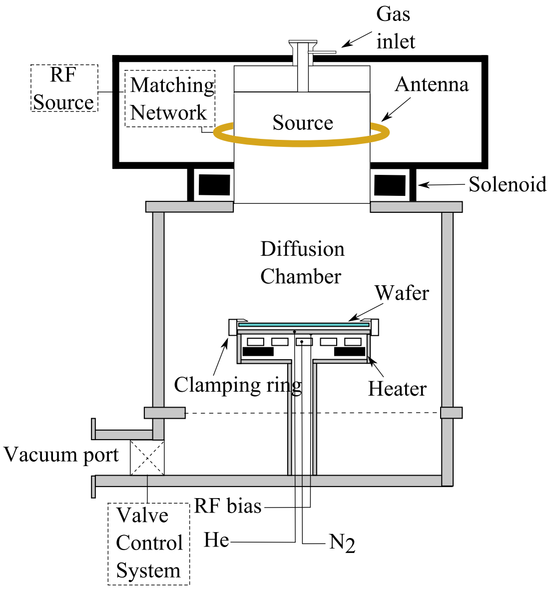

**Figure 1.2.** Schematic of Alcatel cryo-DRIE reactor (reproduced from [35])

While the molecular interactions that produce anisotropic etching and result in the formation of HAR structures in cryogenic RIE also apply to cryo-DRIE, the use of the ICP reactor implies different process parameters. The cryo-DRIE process parameters with typical values range are summarized in Table 1.1.

**Table 1.1.** Typical range of cryo-DRIE parameters

| cryo-DRIE parameters | Typical values | |
|---|---|---|
| | Minimum | Maximum |
| Temperature (°C) | -120 | 30 |
| ICP Power (W) | 350 | 2000 |
| DC bias Voltage (V) | -50 | 0 |
| Pressure (Pa) | 1.2 | 10 |
| $O_2$ flow (sccm) | 5 | 30 |
| $SF_6$ flow (sccm) | 100 | 300 |
| Process Time (minutes) | 1 | 30 |

Parametric analysis of the different cryo-DRIE parameters have provided information on their influence in the BSi topography, and SEM images observations suggest that the needle-like structures are the residual silicon from the etching of a disordered network arrangement of holes in the substrate [13, 21]. While the holes etching follows the mechanism described previously, the formation of the initial roughness that derives in the final BSi structures has not been yet clearly explained. A link has been suggested between the initial formation of BSi structures and the roughness observed in planar Si surfaces after isotropic plasma etching [36].

#### 1.1.1.2 Wet etching

BSi fabrication by wet etching, as the name suggests, involves the use of a liquid solution to etch the sample combined with customized techniques to achieve the anisotropic etching of submicrometric structures. Initial wet etching silicon texturization techniques consisted in anodic etching of Si substrates in HF solutions to produce a low reflectance porous silicon with nanometric structures [37] and the etching of Si wafers coated with a nanometric gold layer in a $HF{:}H_2O_2{:}H_2O$ solution [6, 38]. Variants to these techniques were later reported such as a pulsed electrochemical etching using a $HF{:}C_2H_5OH{:}H_2O$ solution [39], where the topography can be controlled by adjusting the duration and current density of the pulsed etching process, by replacing the Au deposition with a wet etching step in $PdCl_2$ [40], by controlling the size of

Au particle by liquid-phase chemical reduction method [41], or by coating the Si substrate with $HAuCl_4$ solution instead of evaporated Au deposition [42].

#### 1.1.1.3 Laser-chemical etching

Another Si texturing method that results in an array of micrometric structures has been demonstrated using laser pulses duration of 100 fs and energy density of 10 kJ/$m^2$ [2]. While this method requires the presence of Si etching gases such as $SF_6$ or $Cl_2$, the substrate does not need to be in vacuum as in plasma etching techniques. The structures obtained by this process consist of cones height of approximately 40 $\mu$m and diameter of 1$\mu$m. Larger structures (40 $\mu$m of height and 20 $\mu$m of diameter) can be obtained by using laser pulses of longer duration (30 ns) [43]. Due to sulphur doping and texturization process, BSi samples produced by this technique exhibit greater absorbance with respect to untreated Si substrate [5]. It was later reported that submicrometric and nanometric size structures can be obtained with femto seconds laser pulses by submerging the Si substrate in distilled water during the irradiation process [44, 45].

### 1.1.2 BSi applications

Since the initial reports on patterning Si to produce low reflectance surfaces [3], an application has been proposed to improve the power conversion efficiency (PCE) of silicon solar cells. Taking advantage of the BSi formation using reactive ion etching (RIE), which is unaffected by the crystalline orientation of the Silicon substrate, a single-junction solar cell using RIE patterned silicon was fabricated on a poly-crystalline Si substrate, with a reported PCE of 17.1%, providing an increase of 0.7% compared to a solar cell with structured surface using photolithography [4]. An increase of the PCE was also demonstrated on poly-crystalline solar cells, based on porous Si surface produced by an anodic etching technique [46]. Due to the BSi low reflectance over a wide range of incident angles, a study suggests, based on current density measurements, that a BSi solar cell can perform better than a conventional solar cell at oblique incident angles, which can be an attractive feature for solar cells without mechanisms to follow the sun trajectory [47, 48].

While BSi-based solar cells perform better than planar solar cells, there are many challenges that have prevented them from becoming a standard product. First, there is a trade-off between the reflectance reduction and the surface carrier recombination levels that limits the structures height to a small range for optimal PCE [49, 50]. Second, the increase of the surface area caused by the BSi structures increases the sheet resistance when using shallow junctions therefore increasing power losses [32]. Several attempts to overcome these challenges have provided important improvements in the PCE, such as a wet-etching step (damage removal etching) after RIE patterning in order to increase the minority carrier lifetime of the surface [51], yielding a PCE of 17.6% [52]. Measurements of the current density in solar cell with different nano-structure dimensions show the possibility to overcome the losses caused by surface recombination when using periodic silicon nanowires [53]. Another approach is to avoid the losses caused by the front surface recombination by placing the junction on the back surface of the substrate [54]. Recent improvements in the PCE were obtained in BSi solar cells based on metal-assisted chemical etching on crystalline Si wafers, with a PCE reported of 18.2% [55]. The high surface recombination levels observed in textured cells are partially attributed to conventional passivation layer deposition techniques that are not conformal to the structure shape. Measurements of high minority carrier lifetime on BSi with a conformal passivation layer ($Al_2O_3$) applied by atomic layer deposition (ALD) show a great potential for improved PCE in BSi solar cells [56]. Figure 1.3 summarizes the PCE obtained from textured silicon solar cells in the last decades.

In addition to the low reflectance at visible wavelengths that is obtained by patterning silicon, another interesting property reported is the increase of the absorption coefficient in both visible light and near infrared wavelengths [5]. The ability to absorb more light in thinner wafers provides new techniques to design thin films solar cells to reduce fabrication cost [6]. A great improvement in the near infrared sensitivity by using BSi based photodetector was demonstrated [7]. While the increase of the surface absorption coefficient is partially due to the surface texturization, the substrate doping level plays in important role when absorbance near to unity values are required. The substrate doping level can be increased in the front surface during the texturization process, resulting in absorbance greater than 90% (for a wavelength range between 0.4 $\mu$m and 2.5 $\mu$m) [60]; higher absorbance (greater than 99% for wavelength range

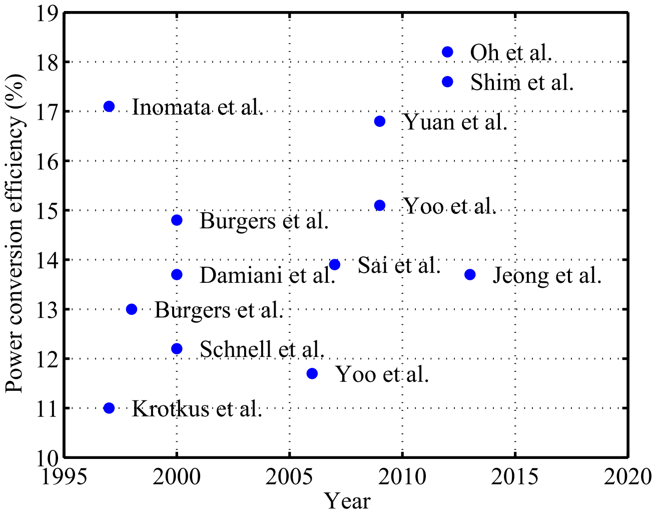

**Figure 1.3.** Power conversion efficiency evolution of BSi based solar cells in the last decade (Inomata *et al.* [4], Krotkus *et al.* [46], Burgers *et al.* [49], Burgers *et al.* [57], Damiani *et al.* [50], Schnell *et al.* [32], Yoo *et al.* [58], Sai *et al.* [48], Yoo *et al.* [51], Yuan*et al.* [59], Shim *et al.* [52], Oh *et al.* [55], Jeong *et al.* [54]).

between 0.25 $\mu$m and 2.25 $\mu$m) are obtained when using heavily doped silicon substrates [61].

Based on measurements of catalytic activity, BSi structures increase the surface area to more than 10 times with respect to a planar surface [8], which implies that BSi surfaces have great potential applications in the miniaturization of devices used for catalytic reactions and sensing. A capacitor fabricated with textured electrodes, having a surface area enhancement of 2, increased its capacitance by 30% when compared to a capacitor with planar electrodes of same dimensions [62]. BSi-based biosensors have been demonstrated with the development of a highly sensitive glucose detector based on nano-textured silicon [63] and a BSi-based surface enhanced Raman spectroscopy detector for algae cells [64]. BSi surfaces have also been used to enhance the surface activity in catalytic microreactors [8] and fuel cells electrodes [65]. Other biological applications of BSi surfaces such as a support for entrapping kidney cells have been demonstrated [66].

Due to its complex topography that consists of dense high aspect ratio structures, BSi has been a fast and convenient technique to create super-hydrophobic surfaces with many applications such as self-cleaning mechanisms [9] and as a support for liquid droplets used in microelectromechanical sensors [10], electrostatic actuators [11] and optical systems [12]. The air pockets between the structures provide an enhanced contact angle of water droplets with values greater than 170° reported [67]. In addition, BSi structures can be either super-hydrophilic by creating a $SiO_2$ layer with $O_2$ based plasma or super-hydrophobic by creating a teflon-like layer with $C_4F_8$ based plasma. Complex droplet shapes can be created by combining the two processes on the sample surface [68]. BSi fabricated with Bosch process exhibits super-hydrophobicity without any further treatment due to the use of $C_4F_8$ as a passivation agent [69].

Despite the nanometric dimensions of BSi structures, they have a considerable mechanical resistance allowing the use of BSi surfaces as a reversible bonding material showing retention forces greater than 1000 $N/cm^2$ [70].

Only recently, works related to self-cleaning solar cells by combining both the low reflectance surface and hydrophobic properties provided by a lithography nano-patterning of the surface has been proposed [9]. Self-cleaning solar cells have great potential for applications in remote locations, such as small cells installed in street lights in arid climates, where maintenance is difficult or expensive. Studies of the power efficiency decrease due to dust accumulations have been previously performed [71, 72], where reductions of the PCE by 17.4% per month has been reported due to dust deposition on 45° tilted solar cells [71].

### 1.1.3 BSi characterization

As previously mentioned, the characterization of the nanometric-sized structures of BSi samples requires specialized microscopy techniques such as imaging with a scanning electron microscope (SEM). Compared to other microscopy techniques such as field-ion and atom-probe, SEM is a more appropriate method for BSi structures visualization and characterization due to its combination of large image scanning size, good resolution and it is a non-destructive technique. While atomic force microscope (AFM) could also be used for BSi visualization, samples having high aspect ratio such as BSi, cannot be accurately observed due to the limited angle of AFM tips which prevent them from reading the bottom of the structures. In this Section we will present the current methods employed to characterize and to obtain accurate three-dimensional representations of HAR nanostructures such as BSi.

#### 1.1.3.1 SEM imaging

The SEM allows the observation of metallic or semiconductor surfaces at very small scale (images of resolution less than 10 nm and size more than 20 x 20 $\mu$m). The sample to be analysed is placed in a high-vacuum chamber where it is bombarded with a fine electron beam that scans the sample surface. While the sample is bombarded with electrons, some of them are back scattered and others interact with the sample producing secondary electrons. Different detectors placed in the chamber allow to collect these backscattered and secondary electrons and convert them into an electric signal which is then converted to an image based on the quantity of electrons detected per sampled area. The advantage of using SEM to observe irregular surfaces is that the quantity of secondary electrons detected depends of the local tilt angle of the surface allowing us to observe images (also called micrographs) that represent the topography of the surface. Although several types of signals can be detected with SEM, in this manuscript we focus in the in-lens and Everhart-Thornley (SE2) secondary electron detectors.

The difference between the in-lens and the SE2 detector being their location, the former detects secondary electrons that are emitted back to the same direction of the electron beam, and the latter detects secondary electrons that are emitted to one side of the chamber. The location of the detectors affects the illumination appearance of the SEM micrographs, so the illumination of an in-lens micrograph appears to occur from the same axis of the observer's line of sight and the illumination, whereas the illumination of a SE2 micrograph appears to occur at a tilted angle of the observer's line of sight [73].

Another feature of the SEM imaging is that the amount of secondary electrons detected in irregular surfaces depends on the surface occlusion or exposure solid angle, meaning that structures that are highly exposed to the electron beam will appear brighter than areas that are highly occluded due to surrounding structures (such as the bottom of holes in BSi). This effect can be observed with both in-lens and SE2 detectors and is the feature that allows inferring the structure height as function of the top-view SEM pixel intensity.

Since the initial reports on subwavelength structures in silicon, SEM has been the most utilized method to characterize the topography of BSi samples. Top-view micrographs of the sample can be used to estimate the diameter and the average spacing of the structures, cross-section views allow the estimation of the height of the structures and tilted views of the samples provide a general idea of the structures' shape and uniformity. The aspect ratio of the structures is deduced from both the height and diameter of the structures.

In previous studies where characterizations of BSi structures were made, the measurement of the average height, diameter and structure spacing is based on SEM images at different viewing angles [13]. The measurement of height based on cross-section view of SEM micrographs can be misleading due to the dense agglomeration of structures and the non-uniform nature of BSi topography that cannot be observed from a single cross-section micrograph. Three-dimensional reconstruction methods can be employed to obtain an accurate representation of the structures height.

#### 1.1.3.2 SEM grey-scale analysis

SEM grey-scale analysis is a reconstruction technique from which a three-dimensional model that represents the surface topography of BSi samples can be obtained. This method consists of inferring the structures height based on the grey-scale level of a top-view SEM image, using the known height values of the SEM brightest and darkest grey-level as bounds of an interpolating range. While other non-destructive methods of reconstruction such as the ones based on multiple images taken at different viewing angles have been demonstrated, they require repositioning the sample at different viewing angles and robust algorithms to detect the same features in the different images [74].

SEM grey-scale analysis has been effectively used in the reconstruction of BSi samples [14]; however, there are some limitations of the maximum hole depth detectable that are due to the limited SEM dynamical range. Therefore, while the SEM grey-scale analysis provides accurate topography information, it is limited to BSi samples with small or medium aspect ratios.

#### 1.1.3.3 FIB-SEM nanotomography

FIB-SEM nanotomography, or serial sectioning, combines the controllable etching capabilities of the focused ion beam (FIB) and the non-destructive imaging capabilities of the

SEM in a single process. It consists of alternating steps of FIB etching and SEM image acquisitions performed on a sample in order to obtain a series of cross-section images at different etching levels. Further processing of this stack of images allows the reconstruction of a three-dimensional representation of the sample. This technique provides a nanometric resolution of the same order of the SEM image (<10 nm with sample size of >20 x 20 $\mu$m) along two axes, and the third axis resolution depends of the etching step length ($\sim$10 nm) and the SEM micrograph acquisition interval. FIB-SEM analysis has been used in many applications such as the characterization of metal alloys, granular and porous surfaces, reconstruction of biological tissue, and others [15].

BSi topographical reconstruction using FIB-SEM analysis implies a simpler procedure than the previous mentioned applications since it consists of a single material without air inclusions or overhanging structures. However, due to the lack of contrast difference between the etched and non-etched material a FIB-assisted metal deposition step (usually Platinum) is applied before the FIB-SEM analysis procedure [75]. Additional preparation steps are required such as etching the material surrounding the area to be analysed [76] and the formation of horizontal alignment marks to have a feedback on the amount of material etched between steps, which is also used to calculate the displacement caused by the tilted positioning [77].

### 1.1.4 BSi optical modelling

Optical modelling of subwavelength structures is a crucial step to find the optimal topographic parameters that provide reduced reflectance, increased absorbance and that meet additional constrains imposed by the application. The topographic parameters necessary for BSi optical modelling are the structure shape, height, diameter, spacing and surface area enhancement factor. One example of a constraint imposed by the application is the surface area enhancement factor in solar cells applications, which has to be kept to a minimum in order to avoid excessive surface recombination that leads to a reduced minority carrier lifetime. The contrary is true in light absorbers used in devices such as telescopes and other optical instruments, where the objective is to reduce reflectance to a minimum regardless of the topography, therefore samples with enhanced surface area can be used.

While optical modelling of BSi samples can provide general guidelines of the best topographical parameters for the application, due to constraints imposed by the cryo-DRIE fabrication process the optimal topography parameters cannot always be achieved. Therefore, it is a common practice to numerically simulate the optical parameters of models based on already fabricated samples, which are then validated with measurements, to find the fabrication parameters that provide the most appropriate BSi sample for the application.

From the various methods of modelling the optical parameters of textured samples, the most utilized are the finite difference time domain (FDTD) method, the finite element method (FEM) and rigorous coupled wave analysis (RCWA). Each method has its advantages and limitations but in general all three methods are capable of calculating optical parameters such as total reflectance, transmittance and absorbance on arbitrary three-dimensional structures. In order to simulate micro/nano-textured surfaces with any of these methods, they require the modelling of a unit cell that represents a typical structure shape that is present in the surface, such as cylinder, pyramid cone, etc. Periodic boundaries are imposed in this unit cell in order to represent an infinite array of structures. The second requirement for optical modelling is to provide the material bulk complex relative permittivity and permeability in function of frequency. When the micro/nano-textured surface is aperiodic with a strong variation of the topographic parameters along the surface (such as BSi), an unit cell can be modelled with a portion of the surface topography [16, 17], however the unit cell dimensions might be limited by the computational resources available in certain numerical methods. Another approach to solve the optical parameters of an aperiodic structure is to model an artificial equivalent single cell that is deduced from a statistical analysis of a large region of the surface and takes in account the variations of the topographical properties [18].

Both FDTD and FEM are numerical modelling methods, based on a discretization of the geometry into a mesh of volumetric elements, capable to solve the Maxwell's equations to obtain the electromagnetic field quantities. The total reflectance, transmittance and absorbance are deduced from the electromagnetic field. Previous reports on simulated optical parameters of nanostructured surfaces using the FDTD method demonstrate a good agreement with measurements. Examples of such reports are the total reflectance simulations of single structured unit cell based on periodic cylindrical silicon nanostructures [27], the total reflectance simulations on single conic structures based on nanostructured silicon, showing similar tendency with measurements with discrepancies at certain wavelengths [78] and simulations of super cells based on BSi topography [16]. Good agreement is observed between simulations and measurements.

RCWA is a semi-analytic method capable to calculate the reflectance, transmittance and absorbance of unit cells consisting of arbitrary geometries by dividing the structure in a multilayered stack and solving each layer analytically. Several reports show that the simulated optical parameters of nanostructured surfaces using the RCWA method can provide good agreement with measurements, examples of such reports are the transmittance simulations of equivalent single structure unit cells based on nanostructured fused silica [18], the specular reflectance simulation at different angles of incidence on unit cells based on nanostructured surfaces of GaN ($\lambda = 632.8$ nm) [17], and specular reflectance at normal incidence of unit cells based on cylindrical periodic silicon structures [79]. While a good agreement between simulations and measurements of specular reflectance is found in the TE polarization, some discrepancies are found in the TM polarization which is one of the drawbacks of the RCWA method [80].

Previous studies of BSi modelling based on a single geometric shape provided reflectance values with similar general qualitative tendencies to the ones obtained by measurements but with considerable quantitative discrepancies [81].

### 1.1.5 BSi growth modelling

While the effects of each cryo-DRIE parameter on the formation of BSi have been previously described, including the molecules interactions between the plasmas and the substrate that allow the formation of microstructures, the mechanism by which a complex topography such as BSi can be generated from a flat surface is not currently well understood. Multiple hypotheses have been proposed regarding the formation mechanisms for BSi topography, such as micromasks originated from native oxide or dust [16, 19, 20], or due to re-deposition of reaction products in certain areas that reinforces the passivation layer [21].

Roughness formation has been observed and characterized in Si surfaces treated with conventional RIE with $CF_4$ and $O_2$ plasmas [82]. A Monte Carlo simulation was proposed that was capable to predict the dynamic evolution of the roughness during the etching process, based on a shadowing factor previously proposed for the three-dimensional growth rate of arbitrary interfaces [83]. This factor is defined as the exposure solid angle that reflects the occlusion level in a certain region of the sample due to surrounding structures. A sticking factor less than 100% was also incorporated to the model, taking into account secondary emissions of etchant products and their redistribution in the surface. In order to determine the dynamic evolution of the roughness, certain topographic parameters were measured at different etching times using the height-height correlation parameters: lateral correlation length and interface width [82].

This model was later expanded to simulate growth processes such as sputtering deposition [84]. Several simulations of deposition processes were performed using both numerical calculations and Monte Carlo simulations, however the results did not agree well with sputtering deposition experiments.

A similar formation model based on shadowing was proposed to simulate the roughness growth during chemical vapour (CVD) or sputtering depositions, where similar tendencies were found in the dynamical scaling parameters between simulations and experiment [85]. It was also demonstrated that the structure lateral correlation length and spacing do not evolve at the same rate.

All the previously mentioned models however, do not explain the high AR's ($> 3$) observed in BSi [13, 21].

## 1.2 Contributions to the state of the art

In Chapter 2, we present experimental results obtained from different BSi samples three-dimensional reconstruction techniques, such as non-destructive SEM grey-level [14] and conventional serial sectioning FIB-SEM analysis [16]. We also present a new simpler method to obtain accurate three-dimensional reconstruction of BSi samples, based on serial sectioning

FIB-SEM analysis, that requires minimum sample preparation steps and provides accurate topography information without the requirement of a contrast layer deposition. The advantage of this technique is that leads in the relocation of the etching beam direction to an angle perpendicular to the BSi structures (or parallel to the plane of the substrate), which reduces the resolution requirements in the etching direction due to the structures' high aspect ratio. We provide discussions of the results obtained with this technique and compared with other attempts to reconstruct different regions of the same sample using the conventional positioning FIB-SEM analysis, and with non-destructive reconstructions based on top-view SEM image grey-scale analysis. Based on the three-dimensional models obtained by FIB-SEM nanotomography, in this manuscript we calculate the topographic parameters of several BSi samples such as the structures' height and spacing histograms, silicon–air fill factor in function of height, aspect ratio and surface area enhancement, the latter being the largest value reported up to this date to our knowledge.

In Chapter 3, we study the influence of the BSi topography on the surface optical properties. First, we provide experimental results of the BSi samples optical properties such as their hemispherical reflectance, transmittance and absorbance, measured with a spectrometer and an integrating sphere. We then present different methods of modelling BSi unit cells used for reflectance and transmittance simulations with the finite element and synthesized capacitance methods [86]. For these unit cells based either on real surface topography [16] or an equivalent structure shapes [29], the chosen dimensions and shape are according to a statistical analysis performed on large regions of the BSi sample topography, providing improved matching between the predictions and the experimental data. We also show an improved matching between simulated and measured reflectances when using an unit cell consisting of multiple structures to take into account the strong variations of the BSi topographic parameters.

In Chapter 4, we present a model that is backed up by detailed experimental data, and that is capable of simulating the entire evolution of a surface from a planar substrate to fully-developed BSi topography. To our knowledge, this is the first successful attempt to model HAR structure formation. We show that the observed evolution of BSi from a planar substrate can be accurately modelled by including the long-range effects of geometric occlusion (or self-shadowing). The resulting simulation model corroborated with experimental observations allows us to create a phase diagram that indicates the combination of control parameters giving rise to BSi formation, and their effect on the final BSi aspect, consistent with experimental observations. The complex geometry of BSi, consisting of needles and holes of various heights and depths, is captured by the model and explains the exceptionally low reflectivity of BSi. The dynamics of BSi formation, including the early-stage development of new etch fronts at topological saddle points (reported here for the first time), as well as the late-stage evolution of aspect ratio with process time, are correctly predicted by the model.

In Chapter 5, we present the fabrication process of a solar cell that incorporates BSi in the front surface in order to reduce the surface reflectance at broad angles of incidence and therefore increases its PCE. The development of this cell is a partial objective to demonstrate the proof of concept of a self-cleaning solar cell that combines the hydrophobic/hydrophilic properties of BSi and its reduced reflectance in order to provide a cell that can sustain its PCE in time without maintenance. We start by characterizations studies of the substrate such as measurements of the minority carrier life time, characterization of the p-doped junction depth by secondary mass ion spectroscopy, and the device fabrication steps with optimized dimensions based on simulations with PC1D [87], previous reports found in the literature and the know-how provided by several research groups. The actual fabrication was not possible during the time frame of this thesis.

Finally, we present the conclusions of this manuscript and the perspectives for future research in this subject.

# Chapter 2

# BSi topography three-dimensional reconstruction and characterization

**Contents**

In the present chapter we describe several reconstruction techniques such as focused ion beam (FIB) nanotomography and non-destructive SEM grey-level analysis, to obtain a three-dimensional model of the BSi topography. While these methods provide accurate reconstructions, each one has its advantages and limitations that are discussed in the following sections. The obtained three-dimensional models allow us performing further characterization of the BSi topography such as statistical analysis of the micro and nanostructures dimensions, accurate estimation of the surface area enhancement factor, and insights of the BSi formation mechanism. In the next section we describe the process parameters of the BSi samples used throughout the manuscript.

## 2.1 BSi sample fabrication

In this section we present the fabrication methodology of the BSi samples used in the manuscript. A total of four samples are fabricated, two of which were characterized by FIB nanotomography and the two others were used in a time-lapse experiment to observe the dynamic morphology changes from planar silicon to the final BSi structures. In the time-lapse cryo-DRIE BSi fabrication, we obtain the topography information at several intermediate etch times by acquiring SEM micrographs of the same sample area at different viewing angles and performing three-dimensional reconstructions using SEM grey-level analysis.

The BSi samples used for three-dimensional reconstruction by FIB nanotomography consist of two Czochralski-grown, p-doped, <100> oriented, silicon wafers of thickness 525 $\mu$m and bulk resistivity 1 - 20 $\Omega$.cm, labelled S01 and S02. The wafers are etched by cryo-DRIE with different process parameters (Table 2.1) in order to produce BSi with different structure dimensions. Top and tilted views SEM micrographs of BSi samples S01 and S02 are shown in Figure 2.1.

**Table 2.1.** BSi cryo-DRIE fabrication parameters

| **cryo-DRIE parameters** | **BSi samples** | |
|---|---|---|
| | **S01** | **S02** |
| Temperature (°C) | -110 | -120 |
| ICP Power (W) | 1000 | 1000 |
| Bias Voltage (V) | -20 | -10 |
| $O_2$ flow (sccm) | 20 | 10 |
| $SF_6$ flow (sccm) | 200 | 200 |
| Pressure (Pa) | 1.6 | 1.5 |
| Processing time (minutes) | 15 | 10 |

From the SEM micrographs (Figure 2.1) we observe that both BSi topographies consist of cylindrical sub-micrometric holes. The intersection of these holes results in the needle-like dense sub-wavelength high aspect ratio (HAR) structures characteristic to BSi producing a

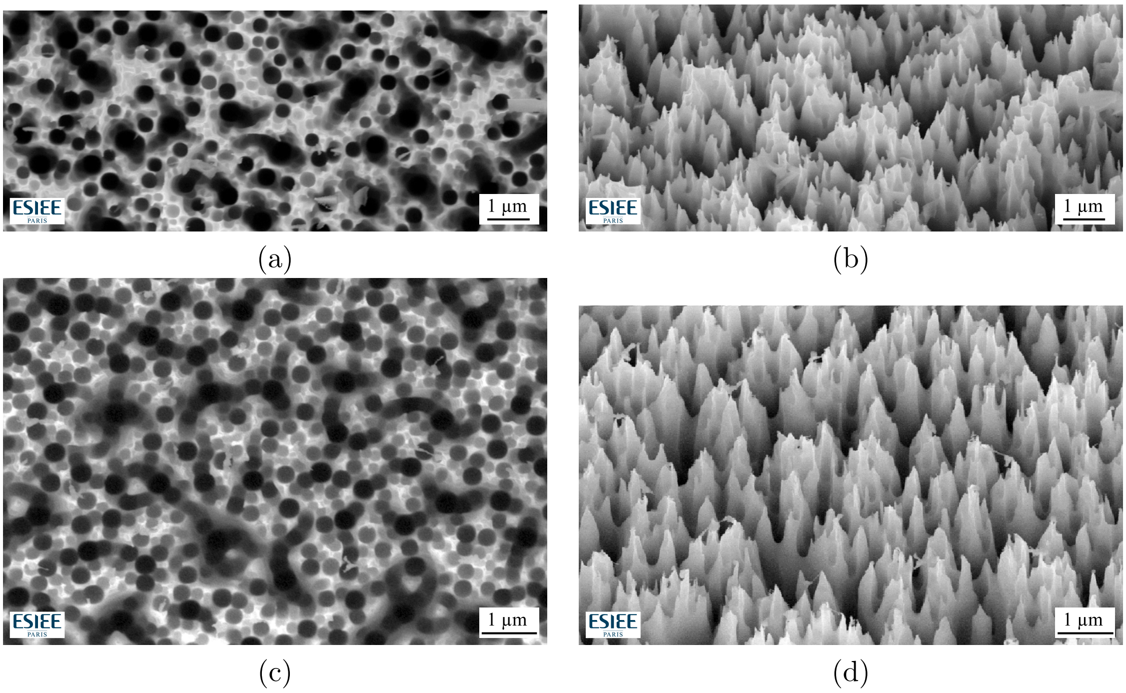

**Figure 2.1.** SEM micrographs of BSi samples: Sample S01 (surface 15.7$\mu$m x 8.8$\mu$m) (a) top-view and (b) 20° tilt view. Sample S02 (surface 10.8$\mu$m x 9.5$\mu$m) (c) top-view and (d) 20° tilt view

diffuse scattering effect on incident light. The reflectance of BSi surfaces is drastically reduced compared to Silicon planar surfaces in broad wavelengths and incident angles ranges (discussed in Chapter 3).

The SEM micrographs of the BSi samples at different viewing angles provide partial information of the topography such as average structure spacing (discussed in Section 2.4.3) and a general idea of the structure height and shape; however, the dense HAR structures induce difficulties for observing the shape of deep holes surrounded by tall structures. In Section 2.2 we present the three-dimensional reconstructions results of BSi samples S01 and S02, which allow to fully characterize their topography in Section 2.4.

The BSi samples used for time-lapse analysis consist of silicon wafers with the same specifications as the ones used for BSi sample S01 and S02 and they are labelled S03 and S04. In order to acquire SEM images of the same region at different process times, we have previously deposited by photolithography certain fiducial markers on the wafer in order to facilitate the localization of the region being studied. The wafers are then etched by cryo-DRIE with different process parameters (Table 2.2) in order to produce BSi with different structure dimensions.

**Table 2.2.** Time-lapsed BSi cryo-DRIE fabrication parameters

| **cryo-DRIE parameters** | **BSi samples** | |
|---|---|---|
| | **S03** | **S04** |
| Temperature (°C) | -120 | -120 |
| ICP Power (W) | 1000 | 1000 |
| Bias Voltage (V) | -10 | -10 |
| $O_2$ flow (sccm) | 40 | 20 |
| $SF_6$ flow (sccm) | 200 | 200 |
| Pressure (Pa) | 1.5 | 1.5 |
| Time-lapse (minutes) | 2 - 4 | 2 - 3 |

At each time-lapse we obtain several SEM micrographs at different viewing angles of the same portion of the samples. During fabrication of BSi sample S03, top-view and 20° tilted view SEM micrographs are taken at t = 2 min and t = 4 min (Figure 2.2); in BSi sample S04, top and tilted views (20°) SEM micrographs are taken at t = 2 min and t = 3 min (Figure 2.3).

One difficulty encountered during the time-lapse analysis of the samples was the differences observed in the topography between regions of the sample already exposed to SEM and regions that were not previously observed. This effect has been previously reported and it is caused by a passivation of the sample, during SEM observation, due to hydrocarbon contamination combined with electron bombardment [73]. In order to minimize this effect, an $O_2$ plasma cleaning step is performed between each cryo-DRIE etching step, and the SEM exposure is kept as brief as possible.

## 2.2 Three-dimensional BSi reconstruction by Serial sectioning FIB-SEM analysis

Serial sectioning FIB-SEM nanotomography is a technique where alternating steps of etching and image acquisition are performed on a sample in order to obtain a stack of cross-section images at different etching levels [15]. Further processing of these stacks of images allows the

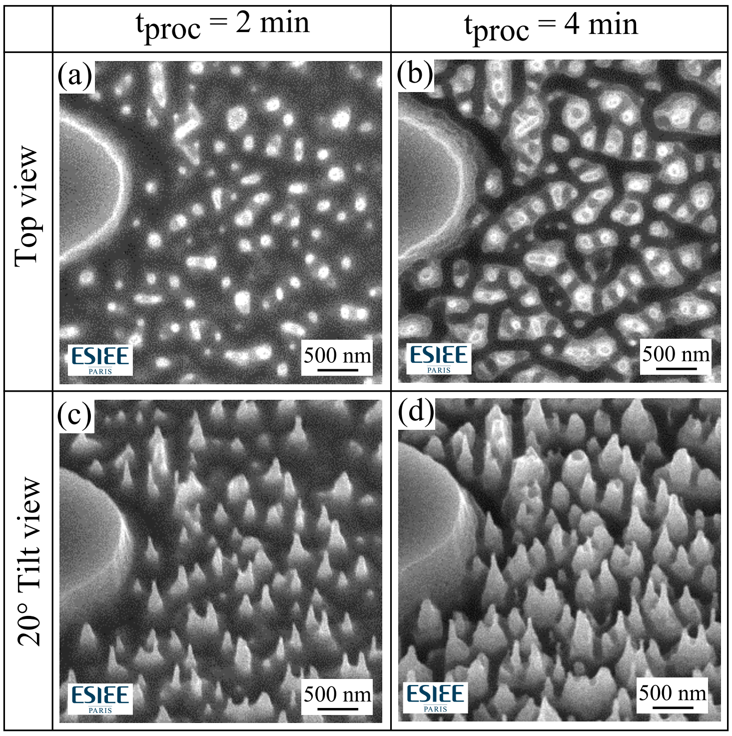

**Figure 2.2.** Time-lapse cryo-DRIE fabrication of BSi sample S03. Top-view SEM micrographs at $t = 2$ min (a) and $t = 4$ min (b). 20° tilt view SEM micrographs at $t = 2$ min (c) and $t = 4$ min (d)

reconstruction of a three-dimensional model of the surface. This technique provides a resolution on the nanometre scale, while being capable of processing samples with approx. 10 x 10 x 10 $\mu$m of size. The typical dual-beam arrangement of the FIB-SEM device (Zeiss NEON 40) comprises one focused ion beam perpendicular to the sample for etching and one electron beam tilted by 54° from the sample used for cross-section micrographs acquisition. In this manuscript we develop a new simpler method to obtain accurate three-dimensional reconstruction of BSi samples, based on serial sectioning FIB-SEM analysis, that requires minimum sample preparation steps and provides accurate topography information without the requirement of a contrast layer deposition. The advantage of this technique is that it relocates of the etching beam direction to an angle perpendicular to the BSi structures (or parallel to the plane of the substrate), which reduces the resolution requirements in the etching direction due to the structures' high aspect ratio (Figure 2.4).

Typical applications of FIB-SEM analysis involve the edge detection of clearly defined boundaries between two materials, where the reconstruction is represented by a volumetric

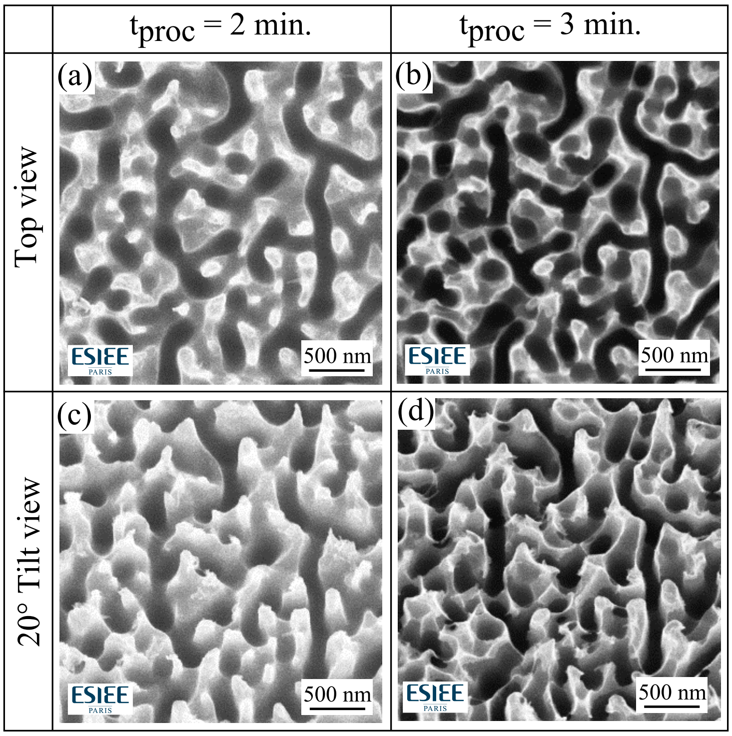

**Figure 2.3.** Time-lapse cryo-DRIE fabrication of BSi sample S04. Top-view SEM micrographs at $t = 2$ min (a) and $t = 3$ min (b). 20° tilt view SEM micrographs at $t = 2$ min (c) and $t = 3$ min (d)

model in cases where one material is embedded in the other. BSi topography being composed of a single material with no overhanging structures, its reconstruction is restricted to the edge detection of a single interface between etched and non-etched material. It is important, however, to have a large contrast difference between etched and non-etched material for accurate boundary detection. Once the boundaries are detected in each serial-sectioning micrograph, the discrete data points representing the elevation of the sample are converted into a three-dimensional representation of the BSi topography.

In the following Sub-sections we present the three-dimensional reconstruction results obtained with several sample positioning methods, using different regions of the BSi samples S01 and S02 presented in Section 2.1.

### 2.2.1 Conventional sample positioning

In the conventional sample positioning, the substrate is perpendicular to the FIB beam (as shown in Figure 2.4a). The dual-column microscope arrangement allows an entire wafer to be tilted by 54 degrees to position the wafer perpendicularly to the FIB column. SEM micrographs are taken between FIB etching steps on a predefined region of size approx. 10 x 10 $\mu$m, from which a series of 54° tilted images of the BSi sample are obtained at different etching levels. These micrographs are later processed to obtain the cross-sectional aspect of the structures.

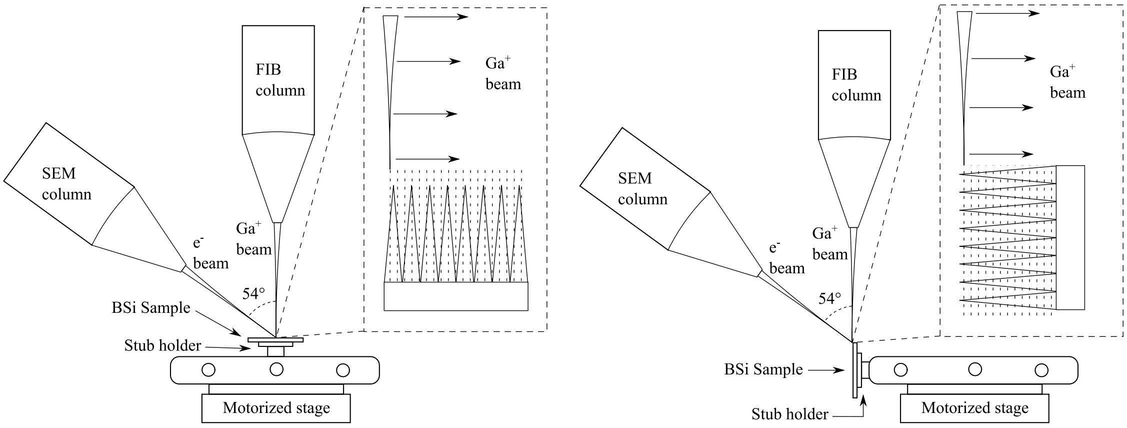

(a) (b)

**Figure 2.4.** FIB-SEM nanotomography BSi sample orientations (a) Perpendicular (b) Parallel

Once the SEM micrographs are obtained from the FIB nanotomography process, we proceed to a series of image processing that allow determining the three-dimensional representation of the BSi sample [15]. As previously mentioned, since BSi samples are surfaces that rarely contain overhanging structures, the image processing is restricted to the detection of a single interface between etched and non-etched silicon. A Matlab program was developed that performs the following tasks (illustrated in Figure 2.5):

- SEM micrographs stack registration

The SEM micrograph stack registration aligns the sample movements or drifts between consecutive serial-sectioning micrograph that occur due to thermal changes and environmental vibrations. The registration process is based on a point location of the BSi surface outside of the etching area. The location of a characteristic shape such a the top of a peak is selected in the first SEM micrograph and then the rest of the images are displaced in order to have the top of the same peak in the same location as in the first micrograph (illustrated in Figure 2.6).

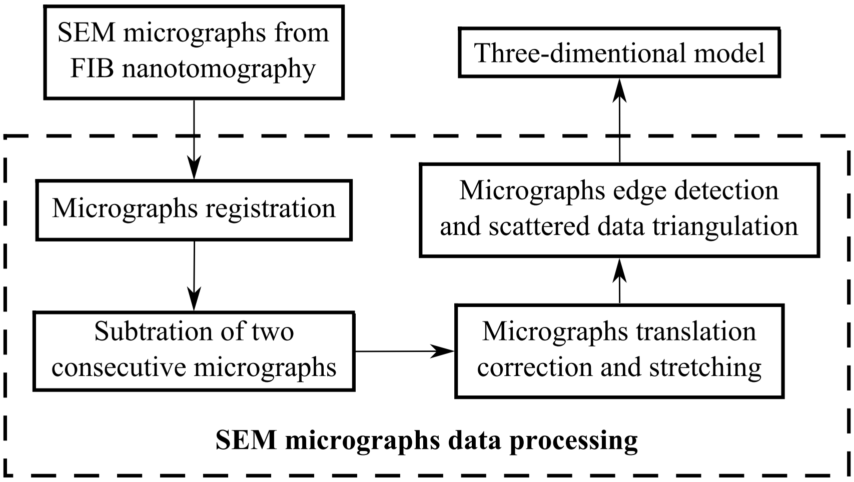

**Figure 2.5.** Flowchart for conventional three-dimensional reconstruction by FIB nanotomography

Once the images are aligned, the regions outside the etching area are removed since they are no longer necessary and in order to have every SEM micrograph with same dimensions.

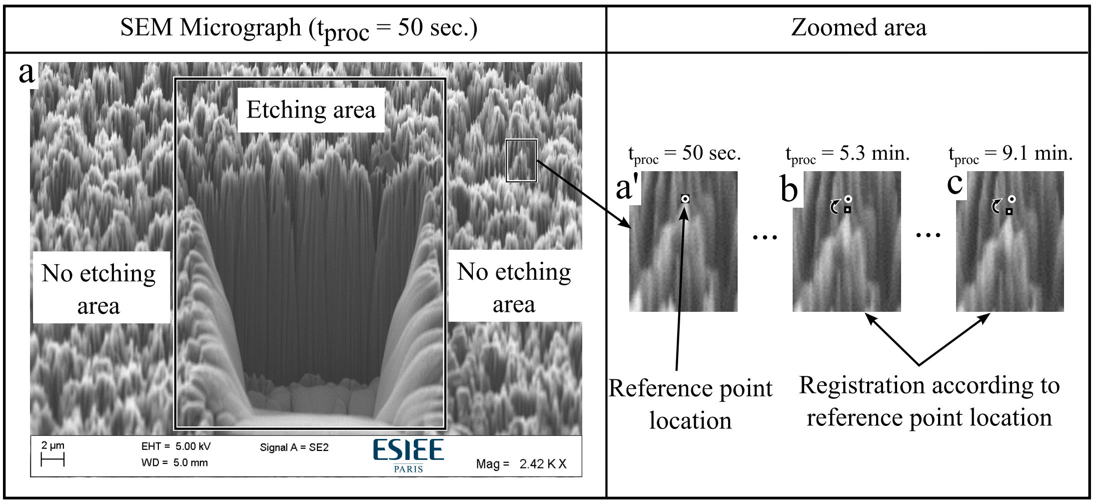

**Figure 2.6.** SEM micrographs registration for sample movement during FIB nanotomography. (a) SEM micrograph at $t_{\text{proc}} = 50$ seconds showing the etching and no-etching areas, (a') zoomed area of SEM micrograph at $t_{\text{proc}} = 50$ seconds where a peak is used as a reference point location, (b) and (c) corresponds to SEM micrographs (at $t_{\text{proc}} = 5.3$ minutes and $t_{\text{proc}} = 9.1$ minutes respectively) showing the peak displacement from the reference point location.

- SEM micrographs stack subtraction

Following the registration process, a pair-wise subtraction of consecutive SEM micrographs is applied to the entire stack to remove features that are not relevant to the edge detection and to enhance the area where the etching occurred, which facilitates the boundary detection as illustrated in Figure 2.7.

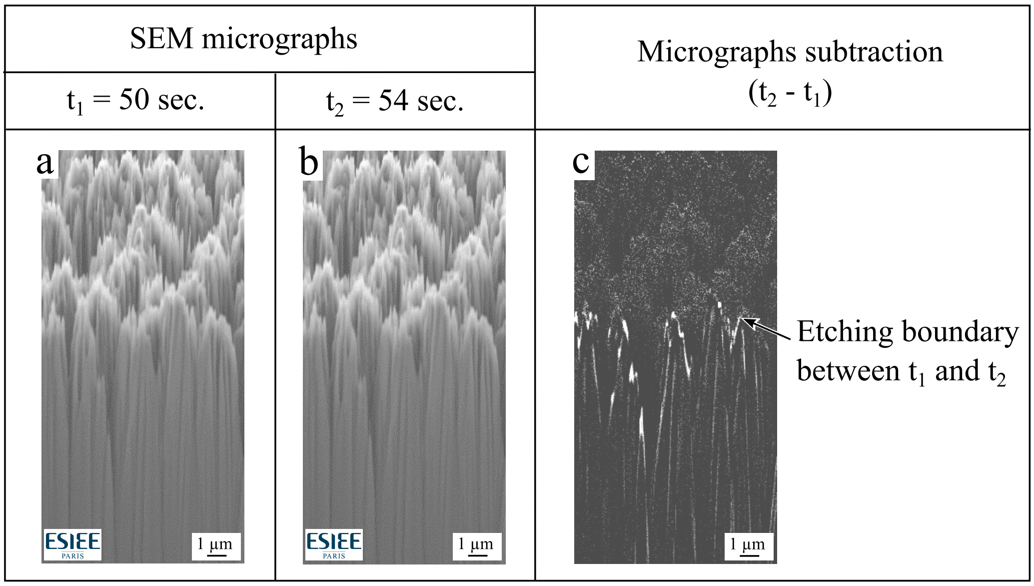

**Figure 2.7.** Pair-wise SEM micrographs subtraction to enhance etching boundary. (a) and (b) corresponds to SEM micrograph at $t_{\text{proc}} = 50$ seconds and $t_{\text{proc}} = 54$ seconds respectively. (c) Image resulting from subtraction of micrographs (a) and (b), where the bright contour represent the etching boundary

.

- SEM micrographs stack translation correction and stretching

Following the image subtraction step, we proceed to the stack translation correction which consists of a second image registration applied to correct the apparent vertical displacement of the structures due to the tilted position of the SEM column with respect of the cross-section view of the structures. The process starts with the last SEM micrograph as the reference position, a vertical displacement is applied to the rest of the SEM micrographs equivalent to $\delta z = \delta y \cdot n \cdot \sin(54°)$, where $n$ is the slice SEM number with respect to the last SEM and $\delta y$ is the FIB etch increment between images (which is set in the FIB-SEM machine before the etching process). After the images alignment each SEM micrograph is stretch in the vertical direction by a factor equivalent to $1/\cos(36°)$ in order to obtain the cross-section aspect ratio of the structure in normal view.

- SEM micrographs edge detection and height data triangulation

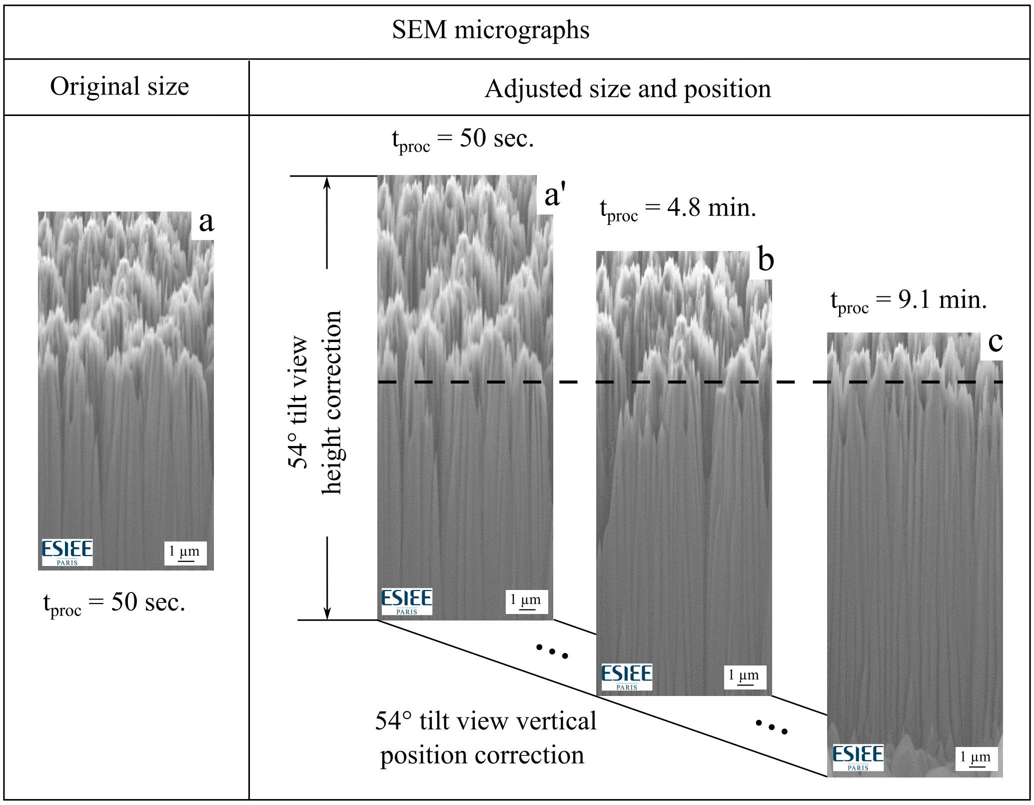

**Figure 2.8.** SEM micrographs 54° tilt-view size and vertical position correction. (a) SEM micrograph at $t_{proc} = 50$ seconds, (a') height adjustment of SEM micrograph at $t_{proc} = 50$ seconds to obtain cross-section view aspect ratio, (b) and (c) corresponds to SEM micrographs (at $t_{proc} = 4.8$ minutes and $t_{proc} = 9.1$ minutes respectively) with size and position adjustment due to the tilted view.

Finally, an edge detection is applied to determine the boundary between etched and non-etched silicon in each SEM micrograph. This detection produces a set of scattered points that represent the elevation in the $x$-$y$ plane. In order to have a bi-dimensional array that represents the BSi topography in the form of $z = f(x, y)$, we proceed to a Delaunay triangulation of the scattered data points [88].

#### 2.2.1.1 Without contrast enhancement layer

We proceed to a FIB-SEM nanotomography trial in a region of BSi sample S01 (labelled S01a), with an area size of 11 $\mu$m x 8.8 $\mu$m and without any prior contrast layer deposition. The FIB operates at 30 kV with a milling current set to 5 nA, the SEM aperture size is set to the default 30 $\mu$m in diameter and with one SEM micrograph acquisition every 100 nm of etched material. Additional FIB-SEM parameters are shown in Table 2.4.

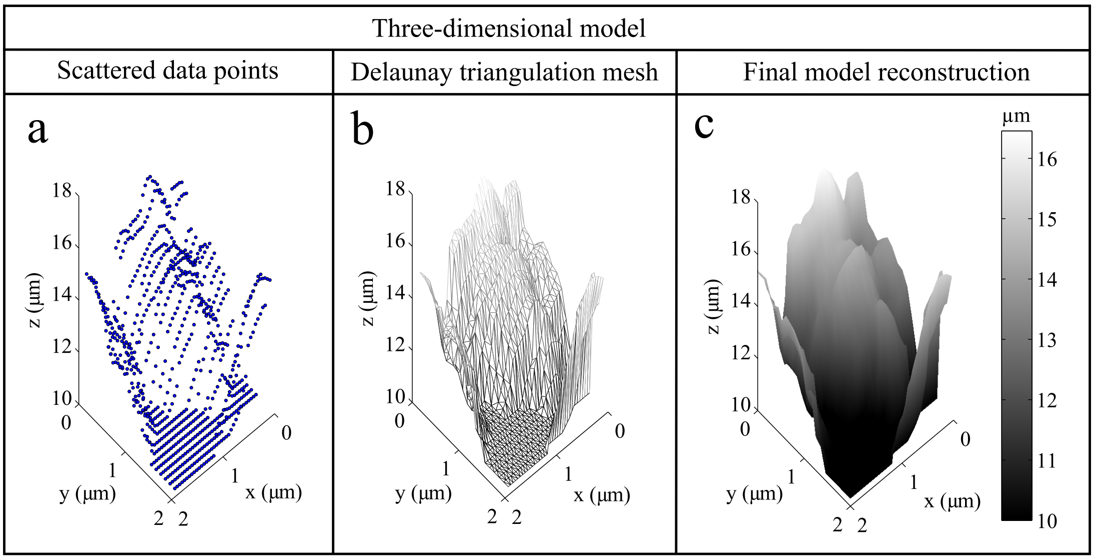

**Figure 2.9.** BSi height data triangulation. (a) Scattered data points of small BSi surface region, (b) BSi surface after Delaunay triangulation and (c) final view of model reconstruction.

In Chapter 1 we mentioned that the intensity of the pixels from the SE detector is highly dependent on the material topography. However, secondary electron reemissions from the sample also depends on the atomic number of the material; this relationship provides a useful method to detect elements on composite materials such as metal alloys [73]. In previous conventional serial-sectioning FIB-SEM analysis on BSi samples [16], a conformal layer is deposited on top of the sample in order to enhance the contrast which facilitates the boundary detection between etched an non-etched material. When using Platinum as a conformal layer on top of Silicon, it provides a very well defined boundary due to their difference in atomic number. In this test, we do not apply a contrast layer on top of the BSi surface, in order to test if the contrast difference provided by the surface angle between etched and non-etched material is sufficient for boundary detection.

Figure 2.10a shows the initial SEM micrograph of BSi sample S01a during FIB nanotomography, after image registration and before translation correction and stretching. In the same Figure, a line describes the boundary between etched and non-etched areas. Accurate detection of this boundary is difficult due to the presence of low brightness vertical lines observed in the SEM image, which are FIB artefacts called “Waterfall” caused by the irregular surface topography [89]. After processing all the serial sectioning SEM images with the process

**Table 2.3.** BSi S01a FIB-SEM etching parameters

| FIB-SEM Parameters | BSi sample S01a |
|---|---|
| Reconstruction size ($\mu$m) | 11 x 8.8 |
| FIB tension (kV) | 30 |
| Milling current (nA) | 5 |
| SEM image acquisition interval (nm) | 100 |
| Total milling time (minutes) | 9.2 |
| SEM aperture size ($\mu$m) | 30 |
| Contrast layer material | N/A |
| Contrast layer thickness (nm) | N/A |

described in the previous section, we obtain a three-dimensional model of the BSi sample S01a topography (Figure 2.10b and 2.10c).

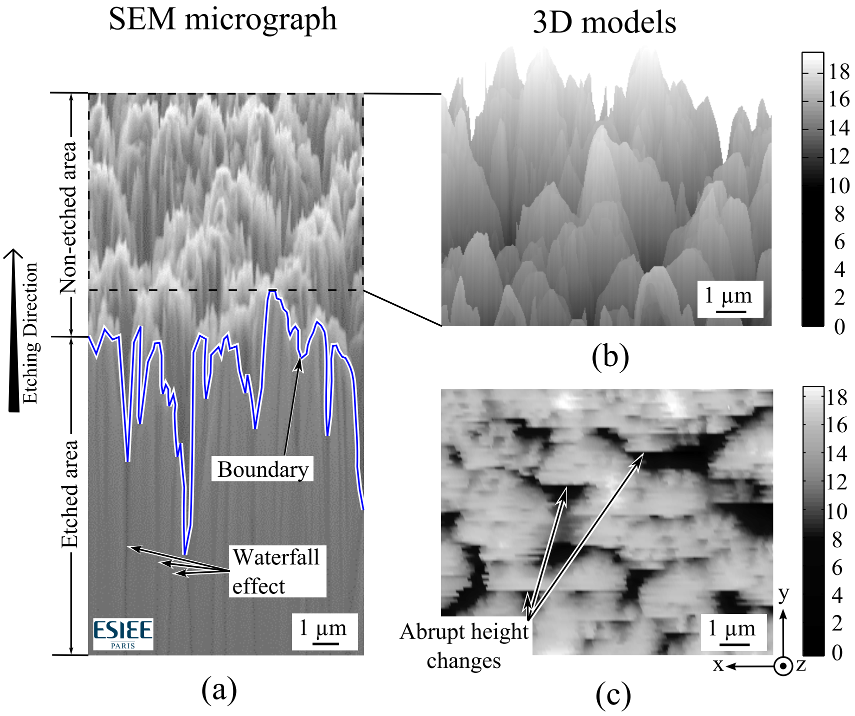

**Figure 2.10.** SEM micrograph of BSi sample S01a during conventional FIB-SEM process without contrast enhancement layer: (a) Initial SEM micrograph (54° tilt view). BSi S01a three-dimensional model 54° tilt view (b) and top-view (c)

The 54° tilted view of the three-dimensional model obtained from FIB nanotomography of BSi sample S01a (Figure 2.11b) shows certain resemblance to the SEM micrograph of the same region (Figure 2.11a); however, some structure details observed in the SEM are absent in the model. The abrupt height changes observed from Figure 2.10c in the etching direction ($y$-axis) demonstrate a poor reconstruction when compared to the axis perpendicular to the etching direction ($x$-axis), which suggest that the SEM micrograph acquisition interval of 100 nm is not sufficient to give an accurate representation of the topography. In addition, these abrupt height changes are only observed on half of the structures (the front portion when observing Figure 2.11b) whereas a smoother height change is observed in the other side of the structures. This effect is due to lack of contrast difference between the etched and non-etched portion of the structures that are facing the FIB beam, the interface boundary can be detected only after the highest point of the structure has been etched; as in this case, the contrast is high enough to recognize the etched area from the image background after the image subtraction step. To overcome this limitation, a contrast enhancement layer such as platinum is required to accurately detect the FIB-beam front-facing etching boundary.

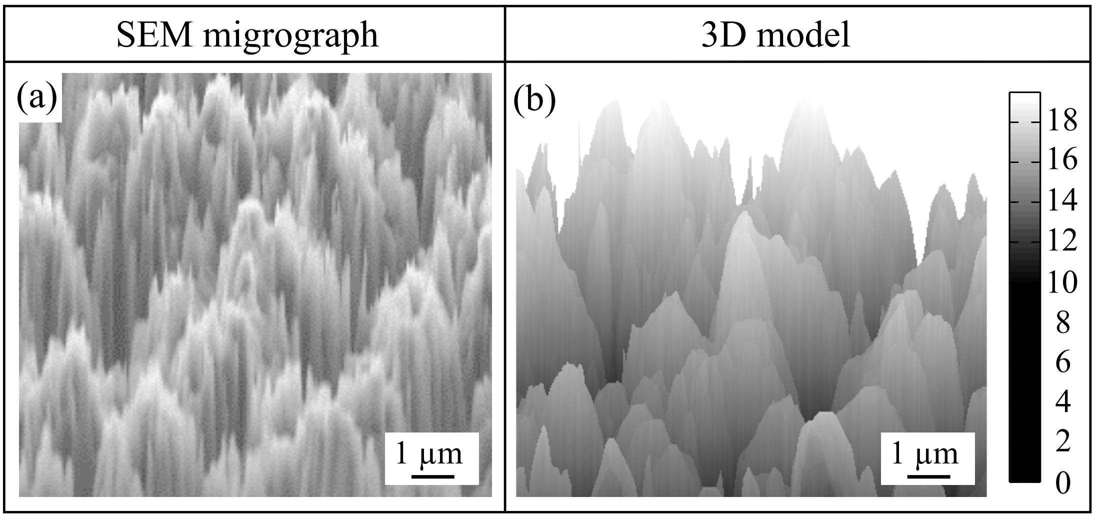

**Figure 2.11.** Three-dimensional reconstruction of BSi sample S01a with conventional FIB nanotomography: BSi sample S01a 54° tilted view of (a) SEM micrograph and (b) three-dimensional model

#### 2.2.1.2 With contrast enhancement layer

We proceed to another FIB nanotomography trial in a second region of BSi sample S01 (labelled S01b) with similar etching parameters previously applied except that the reconstruction size is reduced to 5 x 5 $\mu$m, the FIB milling current is reduced to 1 nA and the SEM image acquisition interval is reduced to 25 nm to increase the resolution of the three-dimensional model in the FIB etching direction. In addition, prior to the FIB nanotomography process, a 100 nm platinum layer is deposited on the sample by sputtering in order to enhance the contrast between the etched and non-etched areas of the FIB beam front-facing portion of the structures. The etching parameters are shown in Table 2.4.

**Table 2.4.** BSi S01b FIB-SEM etching parameters

| **FIB-SEM Parameters** | **BSi sample S01b** |
|---|---|
| Reconstruction size ($\mu$m) | 5.1 x 5.1 |
| FIB Tension (kV) | 30 |
| Milling Current (nA) | 1 |
| SEM Image acquisition interval (nm) | 25 |
| Total etching time (minutes) | 60 |
| SEM aperture size ($\mu$m) | 10 |
| Contrast layer material | Platinum |
| Contrast layer thickness (nm) | 100 |

Figure 2.12a shows the initial cross-section SEM micrograph of BSi sample S01b during FIB nanotomography. Both the increased resolution of the image and the use of the platinum layer facilitate the detection of the boundary between etched and non-etched areas. After processing all the serial sectioning SEM micrographs with the image processing steps described previously, we obtain a three-dimensional model of the BSi sample S01b topography (Figure 2.12b). As with the previous BSi sample, during the image processing, difficulties in the boundary detection between etched and non-etched areas were encountered due the presence of “waterfall” artefacts.

The top-view of the three-dimensional model obtained from FIB nanotomography of BSi sample S01b (Figure 2.13b) shows improved resemblance to a SEM micrograph from the same sample (Figure 2.13a), compared to the previous experiment without contrast enhancement layer. Similarities in the sub-micron features (holes) observed both top-view images suggest an accurate reconstruction. The abrupt height changes observed in the previous experiment are greatly reduced, however in Figure 2.13b some abrupt height changes can still be observed in deep areas between peaks. These detection errors are attributed to a non-conformal deposition of the contrast enhancement layer, which is evident when observing the low brightness in deep

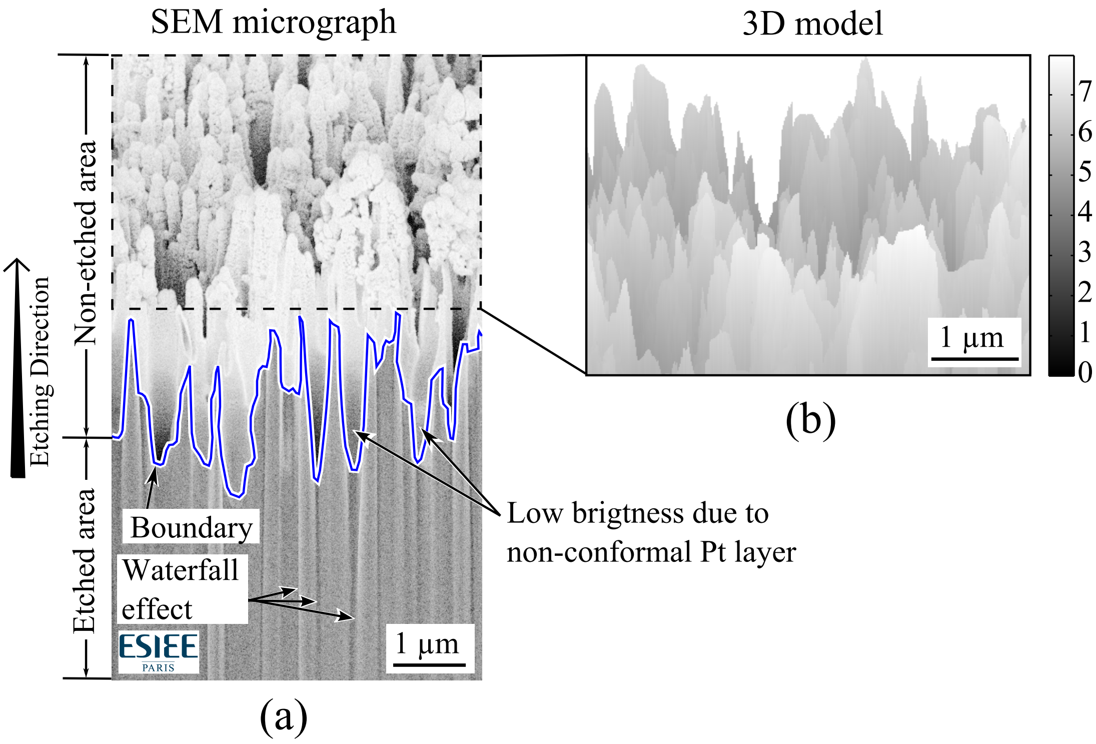

**Figure 2.12.** SEM micrograph of BSi sample S01b during conventional FIB-SEM process with contrast enhancement layer: (a) Initial SEM micrograph (54° tilt view), (b) 54° tilt view of BSi S01b three-dimensional model

areas at the cross-section SEM images (cf. Figure 2.12a). This problem can be solved by using a technique that provides a fully conformal platinum coating, such as ion beam enhanced deposition [16] or atomic layer deposition.

### 2.2.2 Improved sample positioning

While in the conventional sample positioning an accurate reconstruction of the BSi topography is obtained without cleaving the wafer, it requires a conformal platinum layer deposition and additional steps to prepare the sample for etching. Such steps comprises the sacrificial etching of a large area in front of the region to be analysed, which is necessary to obtain the cross-section view of the BSi sample. This sacrificial etching is usually performed with the FIB which increases the FIB total etching time per analysis. Another constraint of the conventional sample positioning is that a large portion of the etched region cannot be reconstructed due to redeposition of the sputtered silicon in the side areas of the etching region

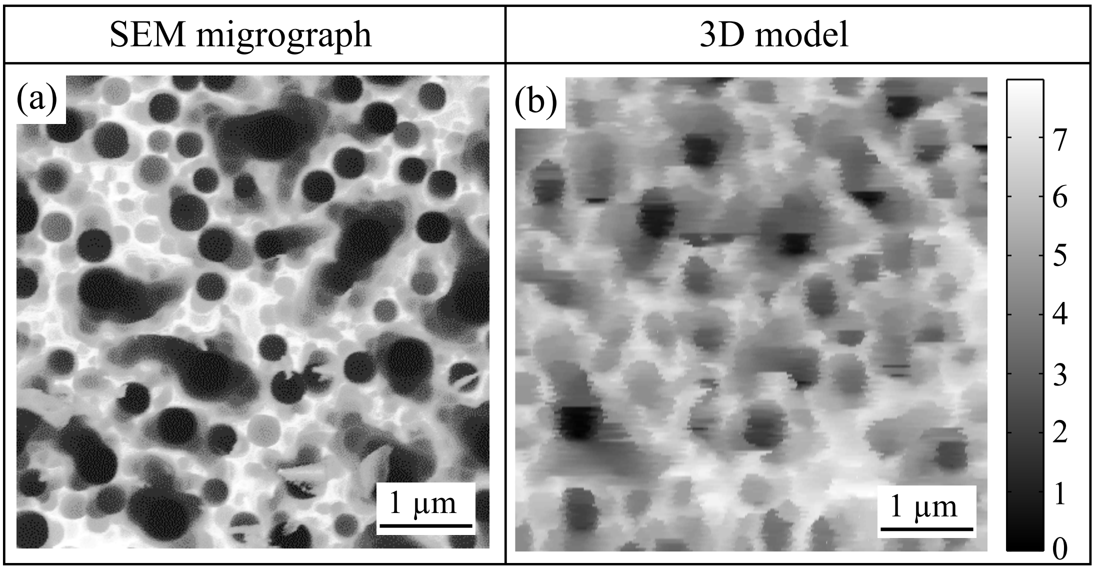

**Figure 2.13.** Three-dimensional reconstruction of BSi sample S01b with conventional FIB nanotomography: (a) SEM micrograph top-view of BSi sample S01 and (b) three-dimensional model top-view of BSi sample S01b

(as illustrated in Figure 2.14), progressively reducing the overall length of the cross-section acquired by the SEM.

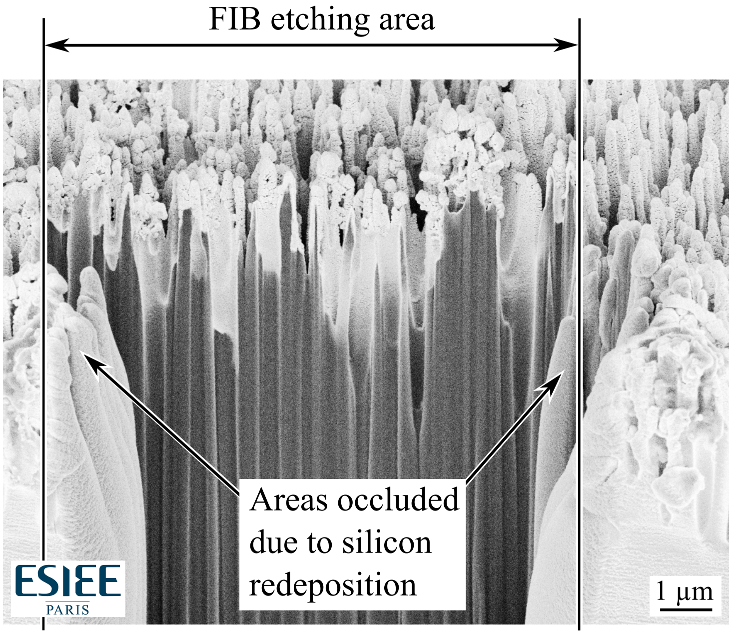

**Figure 2.14.** SEM micrograph of BSi sample S01b during conventional FIB-SEM process showing areas occluded due to silicon redeposition

In addition to the previous constraints, during the analysis of several samples we have observed certain deviations between the actual lengths of material etched between SEM acquisitions and the length that is set in the FIB-SEM software before the etching process. Since the conventional reconstruction explained in the previous section is based on the parameter that is set in the FIB-SEM software, these deviations decrease the accuracy of the reconstructions in both $y$- and $z$-axes. While this constraint can be avoided by etching a horizontal mark to have a feedback of the actual etching between SEM images [77], this solution implies repositioning the sample several times and increasing the FIB etching time per analysis.

Most of the requirements mentioned previously can be avoided by positioning the horizontal plane of the substrate parallel to the FIB beam (as shown in Figure 2.4b), from which we can obtain a series of 36° tilted SEM images of the BSi sample. Since the sample is located on a side of the microscope motorized stage, it requires cleaving the wafer to a small size of approx. 1 cm x 1 cm. Further processing of these SEM images are then performed to obtain the top-view representation of the BSi sample at different etching levels. While the image processing methodology of the improved positioning is similar to the conventional one, the different position implies several changes to the steps previously described for the conventional positioning. In order to obtain an accurate three-dimensional representation of the BSi sample we perform a step sequence similar to the one used in the conventional technique:

- SEM micrographs stack registration

Similarly to conventional sample positioning, we register the SEM micrograph stack based on a point location of one feature outside the etching area.

- SEM micrographs stack subtraction

While having the same purpose of removing non-relevant features (background), the image subtraction process is performed between same depth SEM micrographs obtained with different SEM detectors (in-lens and SE2). As previously explained in Chapter 1, each detectors measures secondary electrons emitted at different directions, providing a particular grey-scale mapping with respect to topography. Taking advantage of the differences in the grey-scale mapping, by mixing the in-lens (Figure 2.15a) and the SE2 signals (Figure 2.15b), we remove the non-relevant features, resulting in an image with high brightness on etched areas and low brightness on non-etched areas (Figure 2.15c). Following the image subtraction, we impose a threshold to have a black and white representation of the SEM micrograph (Figure 2.15d), facilitating the boundary detection.

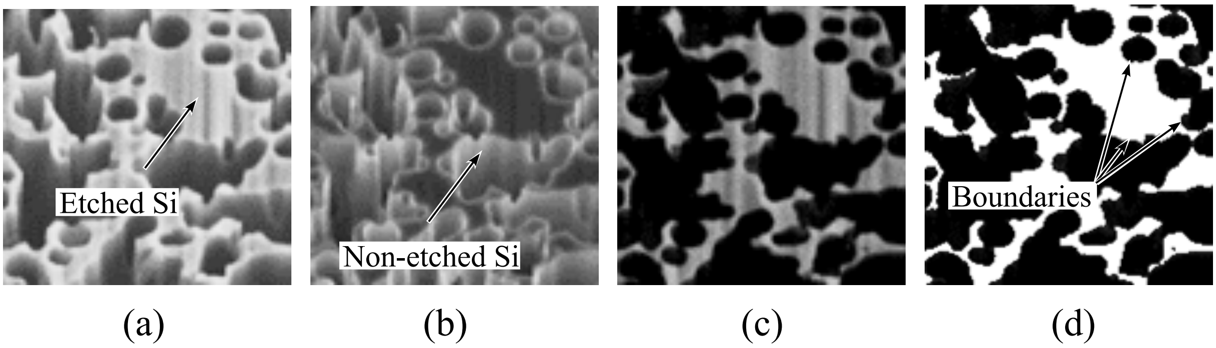

**Figure 2.15.** Image processing of cross-section SEM micrographs using different SEM detectors. (a) In-lens view, (b) SE2 view, (c) Subtraction of in-lens and SE2, and (d) threshold of subtracted image to determine the boundary between etched and non-etched Si.

- SEM micrographs stack translation correction and stretching

In the conventional sample positioning, the FIB etching length between consecutive SEM micrographs is constant and equivalent to the parameter setting in the FIB-SEM machine. In the improved sample positioning, the FIB etching length is measured from the displacement observed in the centre of same holes between consecutive SEM micrographs as illustrated in Figure 2.16. This method corrects the deviations observed between the FIB-SEM setting and the actual etching length between consecutive micrographs, without the requirement of an alignment mark. Following the displacement measurement and correction, every SEM micrograph is stretched to recover the top-view aspect ratio of the structures by a factor equivalent to $1/\cos(36°)$.

- SEM micrographs edge detection and height data triangulation

Similarly to conventional sample positioning, an edge detection is applied in every SEM micrograph to determine the boundary between etched and non-etch silicon, followed by a

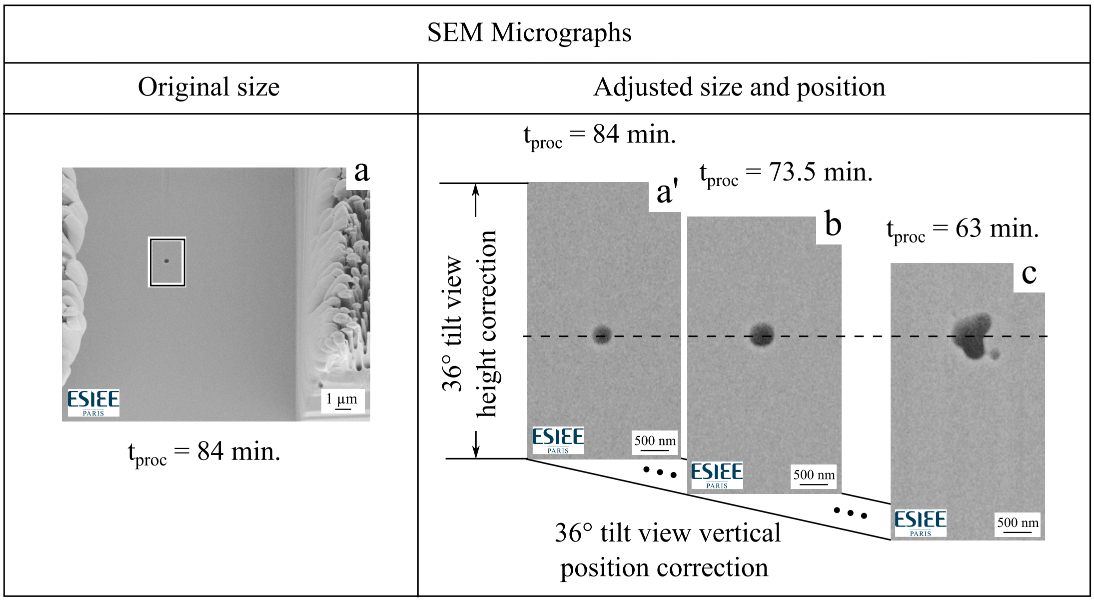

**Figure 2.16.** SEM micrographs 36° tilt-view size and vertical position correction. (a) SEM micrograph at $t_{proc} = 84$ minutes, (a') height adjustment of SEM micrograph at $t_{proc} = 84$ minutes to obtain top-view aspect ratio, (b) and (c) corresponds to SEM micrographs (at $t_{proc} = 73.5$ minutes and $t_{proc} = 63$ minutes respectively) with size and position adjustment due to the tilted view.

Delaunay triangulation to obtain a surface bi-dimensional array that represents the BSi topography in the form of $z = f(x, y)$ [88].

Following the description of the image processing methodology, we proceed to reconstruct the BSi topography of two samples with parallel FIB nanotomography: one sample being a third region of BSi sample S01 (labelled S01c) and another being a region of sample S02. The FIB etching parameters (shown in Table 2.5) are similar between the two samples with the exception of the milling current being lower in sample S02 (since we noticed after processing S01c that 0.5 nA was sufficient to etch the region of interest). In addition, the SEM aperture size was reduced for an improved depth of field that allows maintaining the focus of the SEM images over broader etching depths.

Figure 2.17 shows the 36° tilt view SEM micrographs of BSi sample S01c during FIB nanotomography at different etching levels. The lines in Figure 2.17c describe the boundaries between etched and non-etched areas. In addition, low brightness waterfall artefacts are also observed in the SEM images. When comparing the tilt view SEM micrographs between samples S01c and S02, the same amount of waterfall artefacts are observed even though

**Table 2.5.** Parallel FIB-SEM etching parameters

| FIB-SEM Parameters | BSi samples | |
|---|---|---|
| | S01c | S02 |
| Reconstruction size ($\mu$m) | 18 x 10 | 18 x 7 |
| FIB Tension (kV) | 30 | 30 |
| Milling Current (nA) | 1 | 0.5 |
| SEM Image acquisition interval (nm) | 100 | 100 |
| Total etching time (minutes) | 66 | 100 |
| SEM aperture size ($\mu$m) | 30 | 10 |

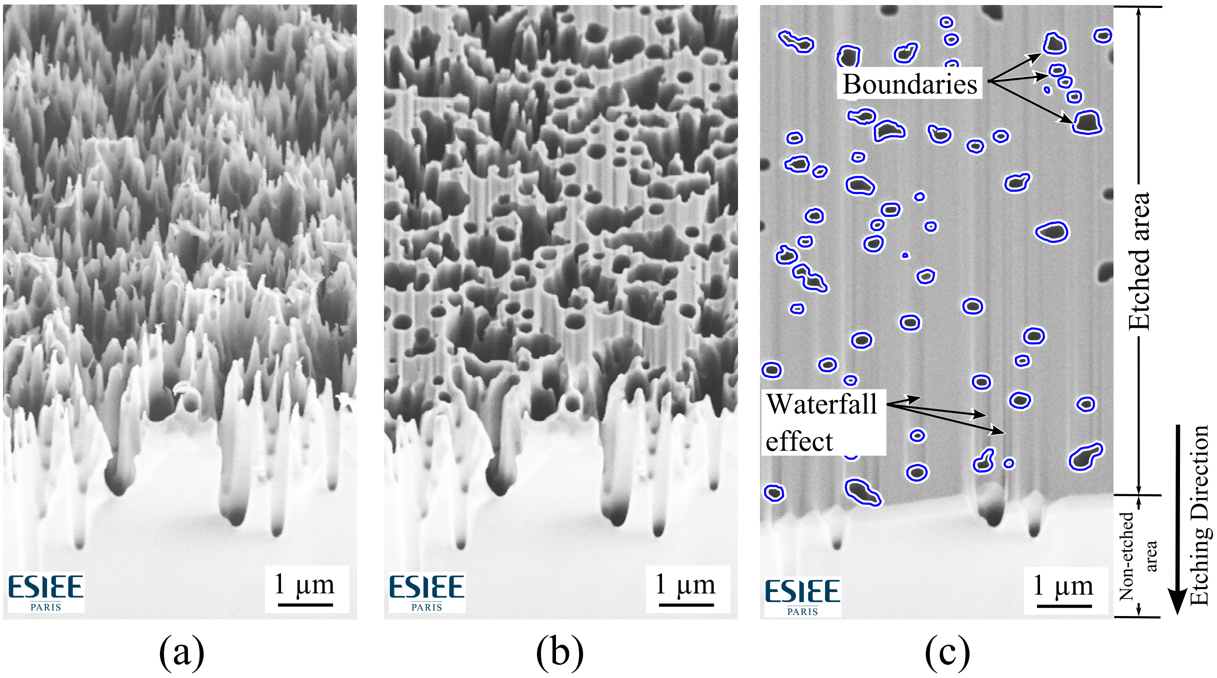

**Figure 2.17.** SEM micrographs of BSi sample S01c during parallel FIB-SEM process (36° tilt view) at different etching levels. (a) depth = 0 $\mu$m (b) depth = 1.8 $\mu$m (c) depth = 5.2 $\mu$m

sample S02 was etched with less milling current. The reduced SEM aperture size greatly improved the depth of field maintaining the sample in focus during the entire etching process; however SEM images with higher noise level were obtained with sample S02, as expected when reducing the aperture size.

Top and 20° tilted views of the three-dimensional models obtained from FIB nanotomography of BSi sample S01c (Figures 2.18b and 2.18d) and S02 (Figures 2.19b and 2.19d) show a remarkable resemblance to the SEM micrographs of the same regions

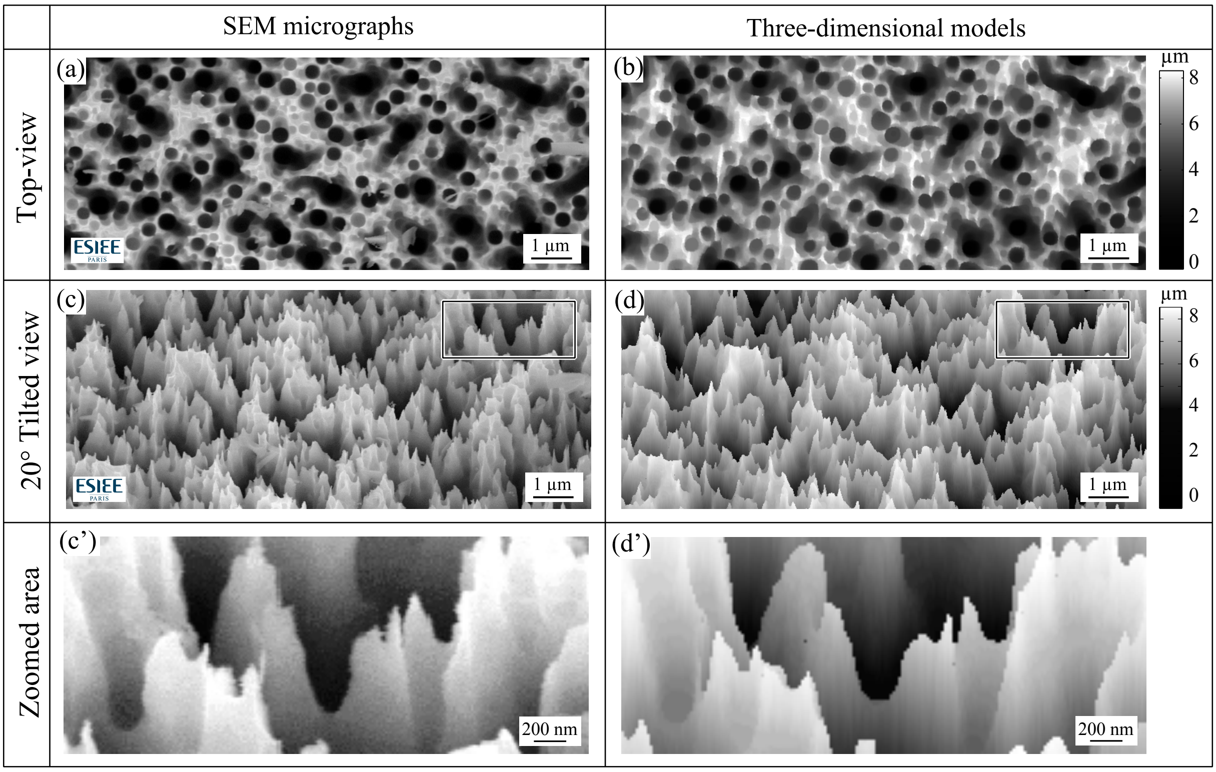

**Figure 2.18.** BSi sample S01c: (a) SEM micrograph top-view, (b) three-dimensional reconstruction top-view, (c and c') SEM micrograph 20° tilt view, and (d and d') three-dimensional reconstruction 20° tilt view.

obtained prior to the FIB-SEM analysis (Figures 2.18a and 2.18c for BSi sample S01c and Figures 2.19a and 2.19c for BSi sample S02). The reconstruction accuracy up to nanometric details can be observed by comparing the zoomed area SEM micrographs (Figures 2.18c' and 2.19c') and three-dimensional models (Figures 2.18d' and 2.19d') of BSi sample S01c and S02 respectively.

In conclusion, we observe that the improved sample positioning resulted in a more accurate reconstruction of the BSi topography to the smallest detail, which is apparent by comparing to the previously acquired SEM micrographs at different viewing angles. Due to the difference in sample positioning, we were able to obtain excellent results using a larger FIB etching increment between SEM acquisitions (100 nm) which makes the FIB-SEM process faster than the conventional positioning (25 nm). Another advantage is that we were able to reconstruct the entire area etched, in contrast to the conventional positioning where due to silicon redeposition the area available for reconstruction is reduced by half. While the improved

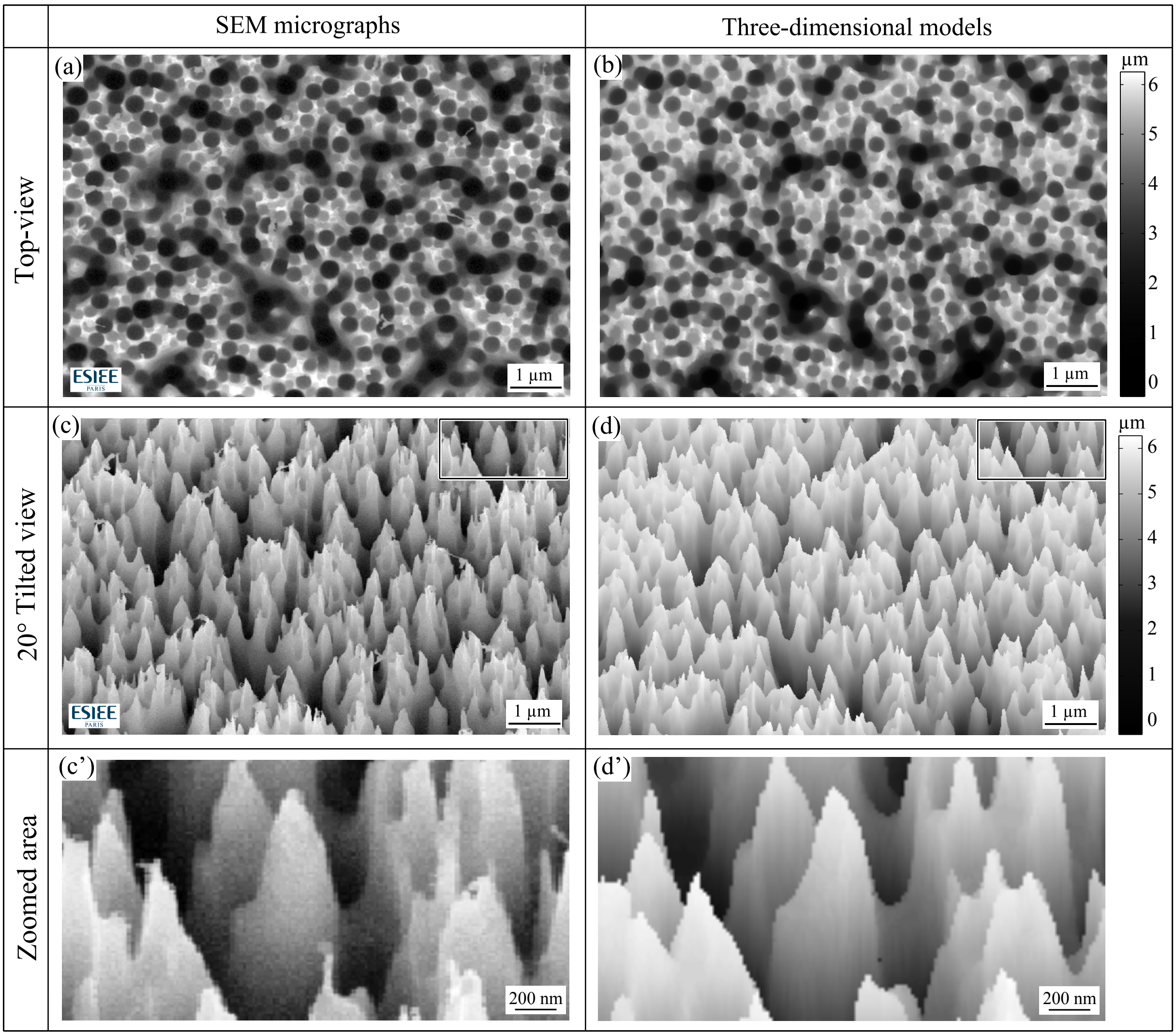

**Figure 2.19.** BSi sample S02: (a) SEM micrograph top-view, (b) three-dimensional reconstruction top-view, (c and c') SEM micrograph 20° tilt view, and (d and d') three-dimensional reconstruction 20° tilt view.

sample positioning does not require platinum coating or alignment marks, its only disadvantage is that it requires the wafer to be cleaved in order to attach it to the side of the microscope motorized stage.

## 2.3 Three-dimensional BSi reconstruction by SEM grey-level analysis

A non-destructive alternative to the FIB-SEM analysis is a three-dimensional reconstruction based on a SEM grey-level conversion to height of a top-view SEM micrograph. This method is non-destructive, easy to implement and has been tested with BSi samples providing good agreement with models based on AFM scanning [14]. However, the accuracy in the deep areas between the peaks is limited by the SEM dynamical range.

The conversion of SEM grey-levels to heights is based on the relation between the secondary electrons detector signal and the surface occlusion or exposure solid angle on irregular surfaces, which makes the highly exposed structures to appear bright in SEM micrographs and occluded regions due to surrounding structures appear dark. This effect allows inferring the structure height as function of the top-view SEM pixel intensity.

In order to analyse the accuracy of the grey-level reconstruction in high aspect ratio (HAR) structures, we proceed to the reconstruction of BSi sample S01 using this method. Taking advantage of the accurate topography obtained from the FIB-SEM analysis, we first plot the relation between pixel intensity and structure depth, by taking random points from both the top-view SEM (before FIB etching) and the three-dimensional model (Figure 2.20).

In Figure 2.20, once we have plotted the depths obtained at different SEM pixel intensity level, we fit a logarithmic function of the form $y = a\ln(x) + b$ used to convert the top-view SEM pixel intensity into a three-dimensional model. After calculating the coefficients of the logarithmic function ($a = 0.97$ and $b = 8.27$), the equation is then applied to the SEM image and the result is compared to the three-dimensional model obtained from FIB-SEM analysis (Figure 2.21).

We observe a great resemblance in the topography obtained from the grey-level (Figure 2.21b) compared to the FIB-SEM three-dimensional model (Figure 2.21a), however, when comparing one cross-section view of the three-dimensional models (Figures 2.21c), we observe that the grey-level method fails to detect deep regions where the height is less than 3 $\mu$m due to the SEM limited dynamic range. The same behaviour is observed in every region of the sample with deep

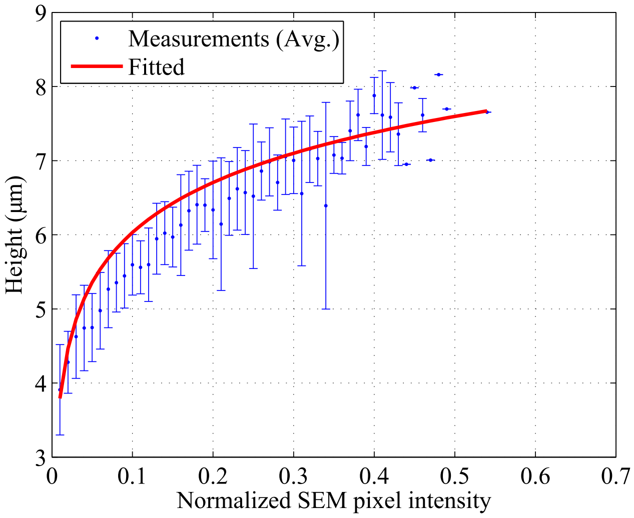

**Figure 2.20.** Relation between the SEM micrograph pixel intensity and avg. height obtained from FIB-SEM analysis. Error bars represent the height standard deviation of multiple points measured with same pixel intensity.

holes, therefore, in this manuscript we limit the use of this method to BSi samples with small to medium aspect ratios, such as BSi samples S03 and S04.

Based on the previous observation, we also proceed to reconstruct the three-dimensional models of BSi samples S03 and S04 (described in Section 2.1) at their initial time-lapse ($t = 2$ min.) by analysing the grey-scale of their top-view SEM micrographs. Figures 2.22b and 2.22d show the three-dimensional reconstruction results of BSi samples S03 and S04 respectively, where we observe that accurate models are obtained by comparing them to their respective BSi sample 20° tilted SEM micrographs (Figures 2.22a and 2.22c).

## 2.4 Topography characterization

To characterize the general roughness parameters of BSi samples, we start by calculating the average values of the structures height and spacing. In a previous report, we have calculated the average height based on manual measurements of several structures taken from cross-section SEM images of the BSi sample [29]. In the same report, the average structure spacing between peaks or holes is obtained from the power spectral density function (PSD) of the top-view SEM image.

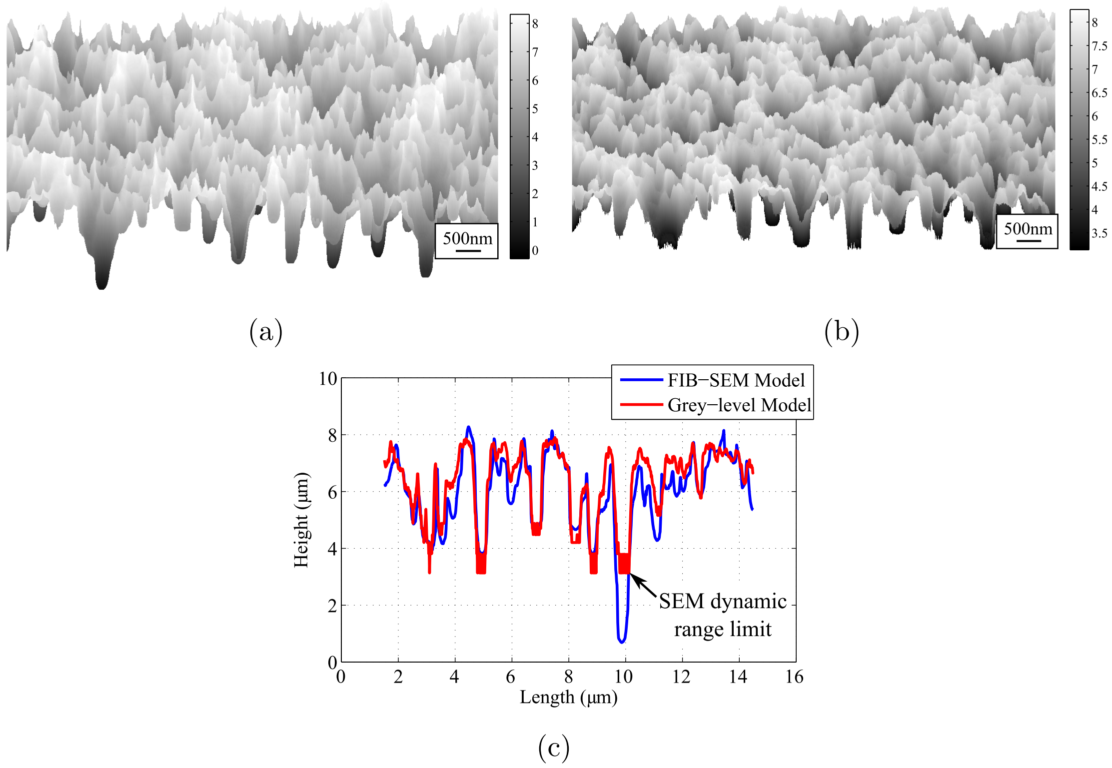

(a)

(b)

(c)

**Figure 2.21.** Comparison between grey-level analysis and FIB-SEM reconstruction for BSi sample S01. 20° tilt views of three-dimensional models obtained by (a) FIB-SEM nanotomography and (b) grey-level analysis. (c) Comparison between the same cross-section view of three-dimensional models obtained by FIB-SEM nanotomography and grey-level analysis.

In this Section, we present a different approach to obtain the topographic parameters using the three-dimensional model representations of BSi samples S01 and S02 presented in Section 2.1, allowing us to determine accurate distribution curves and the statistical moments (e.g. mean and standard deviation) of each parameter.

### 2.4.1 Height distribution

The height distribution is obtained from all the elevation data points of each BSi three-dimensional model. The height is measured using the deepest point as reference. The statistical values such as the mean $h_\mu$ and standard deviation $h_\sigma$ of the surface height are calculated. Figure 2.23a shows the height histograms for BSi samples S01 and S02. Although both samples have similar distributions, the mean structure height of BSi sample S01 is higher than S02. The local variations of structure height can be observed in the cross-section view of BSi sample S02

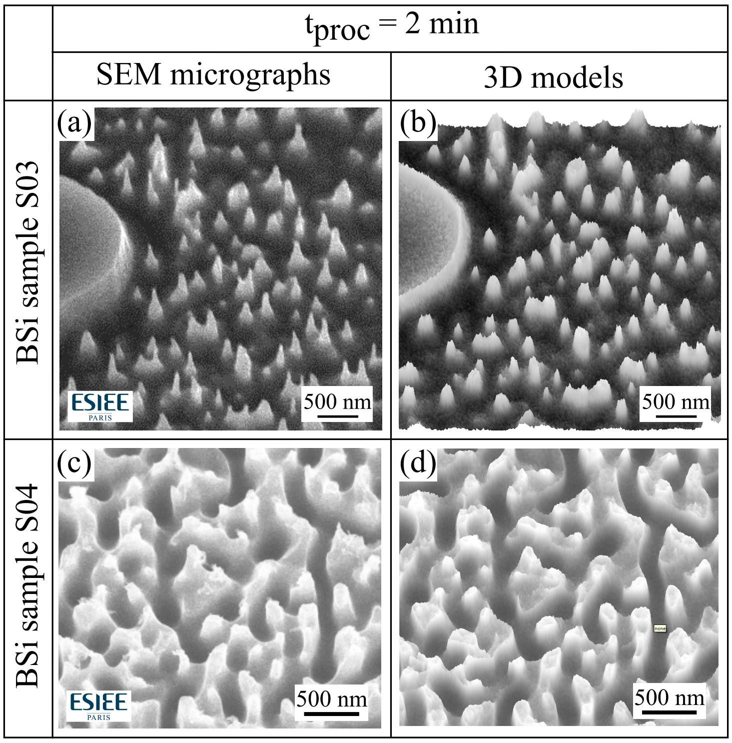

**Figure 2.22.** Three-dimensional reconstruction of initial time-lapse of BSi samples using SEM grey-level analysis. 20° tilted view three-dimensional models (b and d) and SEM micrographs (a and c) of BSi sample S03 and S04 respectively.

(Figure 2.23b) with the difference between global and local height levels and the variation of the distance between the peaks and the holes along the surface.

### 2.4.2 Silicon–air fill factor

With the information obtained from the BSi three-dimensional models we also determine the silicon–air fill factor as function of height, being an interesting parameter that provides the transition shape of the BSi as an interface between the air and the silicon substrate, useful for the optical characterization of the BSi (performed in Chapter 3).

Figure 2.24 shows the silicon content in function of height for BSi samples S01 and S02. We observe that both samples provide similar interface transition between air and Silicon, consisting of a sigmoid curve.

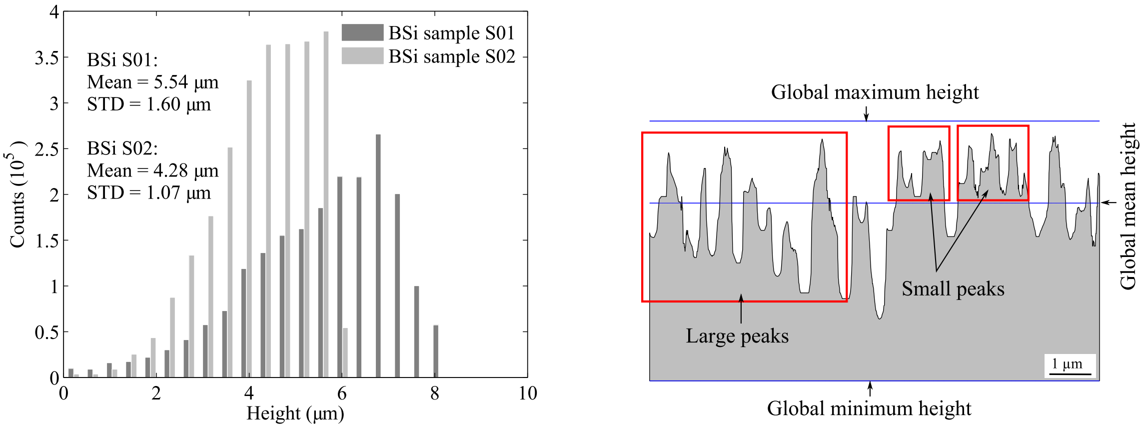

(a) (b)

**Figure 2.23.** Height histograms of BSi samples S01 and S02 (a), indicating their corresponding mean and standard deviation values. (b) BSi sample S02 three-dimensional model cross-section view with lines describing maximum, minimum and mean global heights. The small peaks observed on top of larger scale structures justify the left-skewed height distribution (The distribution mass tends towards the maximum global height).

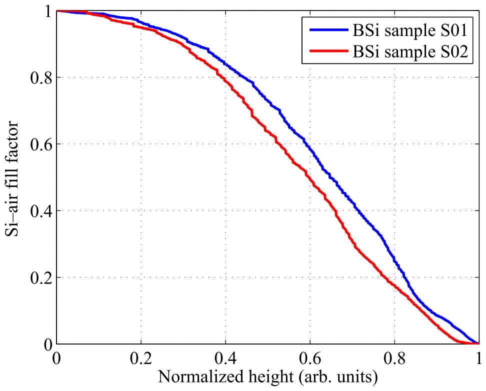

**Figure 2.24.** Silicon–air fill factor *vs.* height of BSi samples S01 and S02

### 2.4.3 Structure spacing distribution

We also determine the structure spacing histograms of BSi samples S01 and S02 (Figure 2.25a) by averaging the distances between the centre of each hole and its closets neighbours. These distances are obtained by means of a Delaunay triangulation applied to all the hole centre points observed on the top-view three-dimensional model of the BSi sample. Since the triangulation mesh provides unrealistic segments at the edges of the model, these are not considered for the structure spacing calculation. An example of the structure spacing measurement in a region of BSi sample S01 is illustrated in Figure 2.25b, where the lengths of the line segments are used to calculate the mean $P_\mu$ and standard deviation $P_\sigma$ of structure spacing.

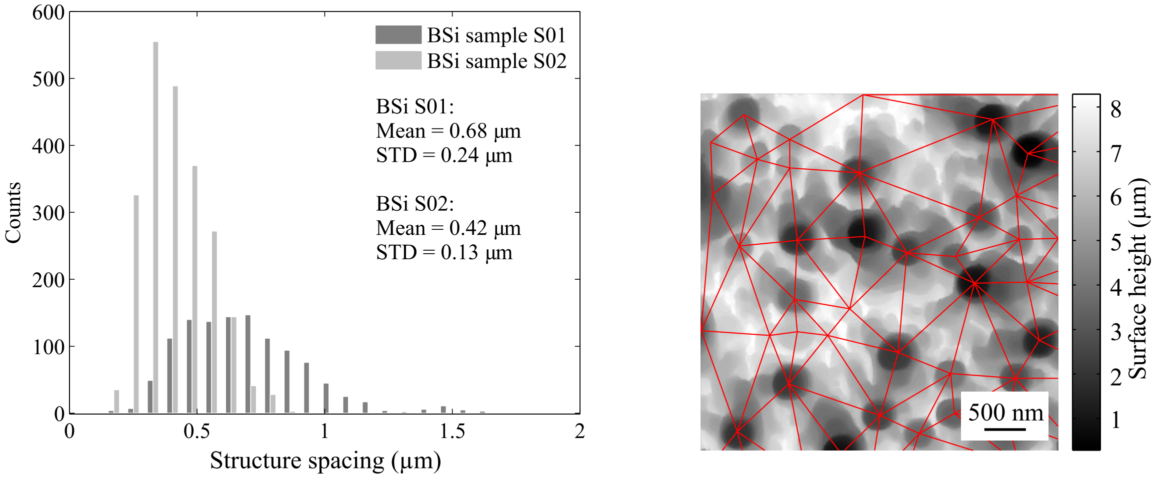

(a) (b)

**Figure 2.25.** Structure spacing histograms of BSi samples S01 and S02 (a) and small section top-view of BSi sample S01 three-dimensional model (b). Red line segments represent the measured distances between neighbour holes and grey-level scale shows the height relative to the global BSi sample height.

By comparing the structure spacing of both samples (Figure 2.25a), we observe that BSi sample S01 has a larger mean and STD of structure spacing than S02. The larger $P_\sigma$ of BSi sample S01 suggests that this sample is more inhomogeneous than sample S02.

### 2.4.4 Surface normal angle and aspect ratio

The normal angle $\alpha_N$ is a local effect that determines how inclined a particular point of the surface is. While there are several methods to calculate the normal angle of a surface, in this manuscript it is defined as the deviation from the vertical axis of a vector that is perpendicular to a small disc locally fitted to the surface. The centre of the disc is placed at the evaluation point of the surface and its radius is fixed to a small value ensuring a local measurement. The fitting process of the disc to the surface is performed by the least mean squares method. Once the deviation angle from the vertical axis is determined, we repeat the process for every point of the surface.

By averaging the normal angles of every point of the surface in BSi samples S01 and S02, we observe that both samples have similar mean surface normal angle (79.44° and 78.49° for BSi samples S01 and S02 respectively). The similarity of the surface normal angle observed in both samples suggests that they have similar mean aspect ratios.

The aspect ratio is often used as referential value to determine the sharpness of the BSi structures. In this manuscript the aspect ratio is calculated by dividing the STD of structure height $h_\sigma$ and the mean spacing between structures $P_\mu$. From calculations of the aspect ratio in BSi samples S01 and S02, we obtain 2.34 and 2.57 respectively.

### 2.4.5 Surface area enhancement

One important parameter of the BSi topography is the surface area enhancement factor, defined as the area of the topography divided by the area of the projection of the surface in the horizontal plane. While estimations of BSi surface area enhancement factor are generally provided based on measurements of catalytic activity [8], we measure the BSi area enhancement factor based on surface topography reconstructions. The BSi total surface area is calculated by adding the area of each simplex obtained from the Delaunay triangulation during the three-dimensional reconstruction by FIB-SEM analysis. The surface area enhancement factor is then obtained by dividing the total area by the product of the samples' length and width. Using this methodology we obtain a surface area enhancement factor of 12.33 and 11.23 for BSi samples S01 and S02 respectively, being the largest value of surface enhancement factor reported up to this date.

### 2.4.6 Surface homogeneity

A study of the large scale variations of the topographic parameters (such as $h_\mu$, $h_\sigma$ and $P_\mu$) are performed to characterize the heterogeneity of the BSi samples. We calculate several parameters derived from the primary topographic ones by dividing the sample in regions of approximately 3 times of the mean structure spacing and calculating the topographic parameter of each small region. Figure 2.26 illustrates the mean and standard deviation of height measures in small regions for sample BSi S02.

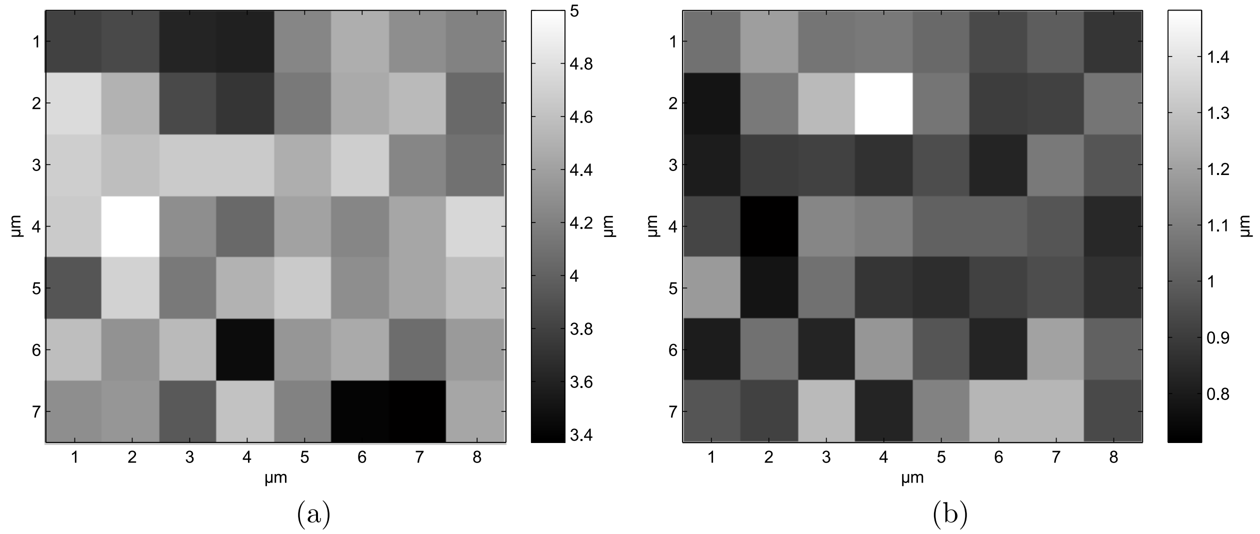

(a) (b)

**Figure 2.26.** Topographic parameters evaluation in small regions of BSi sample S02. (a) Mean height (b) STD of heights.

### 2.4.7 Surface Occlusion level

The occlusion level $\Omega$ (or shadowing) is a long-range effect that determines how occluded is a point of a surface by its surrounding structures [83]. In this manuscript, the occlusion is measured at each point of the surface by using a double integral of a unit sphere where the domain of the polar angle is bounded to the maximum angle of unobstructed view in every azimuthal angle $\theta_\phi$, written as:

$$\Omega_{(x,y)} = \int_0^{2\pi} \int_0^{\theta_\phi} \sin(\theta) d\theta d\phi \tag{2.1}$$

Figure 2.27 illustrates the occlusion level calculation on an arbitrary surface. The maximum polar angle $\theta_\phi$ of unobstructed view is evaluated at every azimuthal angle $\phi$ determining the occlusion level of the point $z$. This procedure is then repeated for every point of the surface. The range of the occlusion level is between 0 and $4\pi$ for maximum and minimum occlusions respectively, and the occlusion level of a planar surface is represented by the mid-range ($2\pi$).

By averaging the occlusion level in every point of the surface of BSi samples S01 and S02,

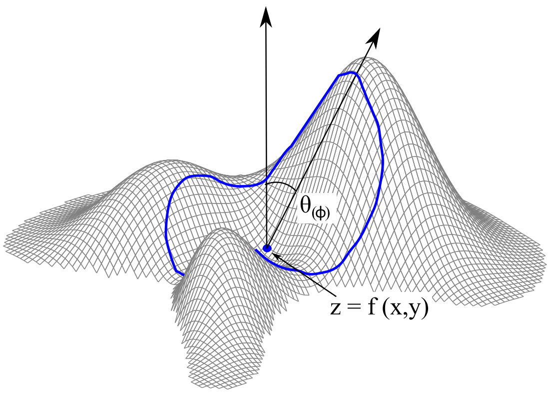

**Figure 2.27.** Diagram of occlusion calculation on an arbitrary surface, the solid curved line describes the contact point of the maximum polar angle with the surface for every azimuthal angle.

we observe that they have similar mean occlusion (0.54 $\pi$ and 0.52 $\pi$ for BSi samples S01 and S02 respectively). In subsequent chapters we refer to the normalized occlusion level $\Omega'$, being equivalent to $\Omega/4\pi$.

In Table 2.6 we summarize most of the topographic parameters measured in the present Section, based on three-dimensional reconstructions of BSi samples S01 and S02.

**Table 2.6.** Topographic parameters of BSi samples S01 and S02

| **FIB-SEM Parameters** | **BSi samples** | |
|---|---|---|
| | **S01** | **S02** |
| Min. structure height $h_{min}$ ($\mu$m) | 0.00 | 0.00 |
| Max. structure height $h_{max}$ ($\mu$m) | 8.28 | 6.24 |
| Mean structure height $h_\mu$ ($\mu$m) | 2.75 | 1.97 |
| Mean structure depth $d_\mu$ ($\mu$m) | 2.75 | 1.97 |
| Mean structure spacing $P_\mu$ ($\mu$m) | 0.68 | 0.42 |
| Mean surface normal angle $\alpha_N$ (°) | 79.44 | 78.49 |
| Mean surface aspect ratio | 2.34 | 2.57 |
| Mean occlusion level $\Omega$ | $0.54\pi$ | $0.52\pi$ |
| Surface area enhancement factor | 12.33 | 11.24 |

### 2.4.8 Topographic characterization of time-lapse BSi samples

In Section 2.1, SEM images at different viewing angles are obtained for every time-lapse of BSi sample S03 and S04. In this section, we measured the geometric parameters of the structures such as the average structure spacing and height. The mean structure spacing is measured using the SEM image top-view with the same technique described in Section 2.4.3. Approximate mean height is calculated from tilted SEM micrographs with the aid of the fiducial markers, where the cross-section aspect ratio of the structures is deduced after a tilt correction rescaling.

Measurements of average structure spacing and height of the BSi samples (Table 2.7) show an increase (between $t = 2$ min and $t = 4$ min) of the structure mean height in sample S03 with an almost unchanged spacing, whereas in BSi sample S04 we observe an increase of both mean height and structure spacing between $t = 2$ min and $t = 3$ min.

**Table 2.7.** Time-lapsed BSi samples topographic parameters

| **Parameters** | **BSi sample S03** | | **BSi sample S04** | |
|---|---|---|---|---|
| | **t = 2 min.** | **t = 4 min.** | **t = 2 min.** | **t = 3 min.** |
| Mean structure spacing (nm) | 462 | 467 | 435 | 483 |
| Mean Height (nm) | 953 | 1990 | 698 | 781 |

# Chapter 3

# BSi optical characterization

**Contents**

As mentioned in the introductory chapter, one of the most interesting properties of BSi is the capability to trap the light which have many applications such as in photovoltaics. A great amount of research has been conducted into creating models of BSi samples that are able to predict their surface reflectance and the material absorbance enhancement. Accurate predictions of the optical parameters based on the BSi topography are important because it allows to adjust the structures dimensions to obtain the desired optical parameters according to the application, reducing the quantity of experimental trials. In addition, it allows to make theoretical predictions from structures that cannot be fabricated yet.

Previous studies have demonstrated accurate predictions of the optical parameters of BSi by comparing with reflectance measurements using different modelling techniques such as the rigorous coupled wave analysis (RCWA) [18], the finite-difference time-domain (FDTD) [16] and the finite element method (FEM) [81]. The model used in the simulation usually consists of a unitary cell composed of a regular shape that resembles the predominant structure observed in the sample (e.g. cone, cylinder). Periodic boundaries are imposed to this unitary cell in order to simulate an infinite array of this cell as illustrated in Figure 3.1. Another model used in the simulation consists of a small portion of the real surface topography with periodic boundaries [16].

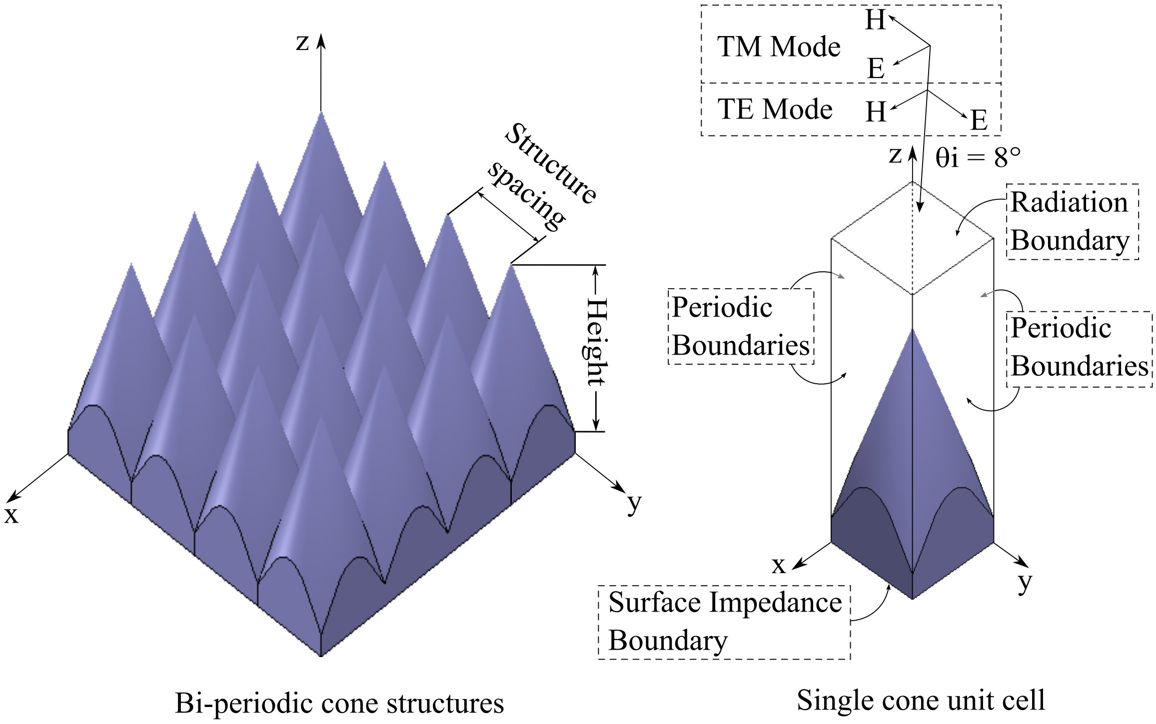

**Figure 3.1.** View of a large bi-periodic micro-structured surface from which a unit cell is defined with periodic boundaries for numerical simulation of reflectance.

In order to have accurate predictions of the BSi samples optical parameters, we require accurate representation models of the BSi topography. In previous numerical simulations using the FEM, parametric studies of BSi structures with dimensions based on cross-section view SEM micrographs have shown similar tendencies as the ones obtained experimentally [81]. However, accuracy of such approach is strongly affected due to the difficulty of modelling real BSi surfaces with their wide range of roughness dimensions and their disordered distribution. In this case the definition of the equivalent unit cell is not obvious, the key point lying in the choice of the appropriate bi-periodic unit cell that includes the influence of the heterogeneity of BSi structuring.

In Chapter 2, we performed an exhaustive characterization of the BSi topographical parameters based on accurate three-dimensional representations obtained from FIB-SEM analysis. In the present chapter we perform simulations of several models that represent BSi samples to predict their optical parameters such as reflectance, transmittance and absorbance. We start by measuring the reflectance of the BSi samples presented in Chapter 2 with an integrating sphere and a photo-spectrometer, followed by describing the numerical simulation methods used to obtain predictions of the BSi reflectance. We then perform simulations of reflectance using different BSi unit cell models including a new model proposed that incorporates the strong variations of BSi structures dimensions and their disordered distribution. All the simulation results are compared with measurements obtained experimentally. In this chapter we also study the influence of the BSi disordered structure in the reflectance reduction at different angles of incidence (AOI) and the BSi capabilities to enhance the Si substrate absorbance.

## 3.1 Reflectance measurements

The general definition of reflectance $\rho(\lambda)$ at a specified wavelength is the ratio of the reflected radiant flux $\Phi_{\lambda r}$ to the incident radiant flux $\Phi_{\lambda i}$ [90], as described in equation 3.1.

$$\rho(\lambda) = \frac{\Phi_{\lambda r}}{\Phi_{\lambda i}} \tag{3.1}$$

The hemispherical reflectance measurements of Si wafers and BSi samples are performed with a spectrometer and an integrating sphere (Ocean optics Maya-2000 Pro), allowing us to measure the total reflectance (both specular and diffused components).

The reflectance measurement setup is shown in Fig. 3.2. More information regarding the specifications of the measuring equipment can be found in [91].

The reflectance $R$ being determined as the ratio of the total reflected radiant flux to that of a reference diffuser [90], a certified 2% diffuse reference is used. The light beam enters the integrating sphere with an incident angle of 8° from normal and the reflected flux is collected

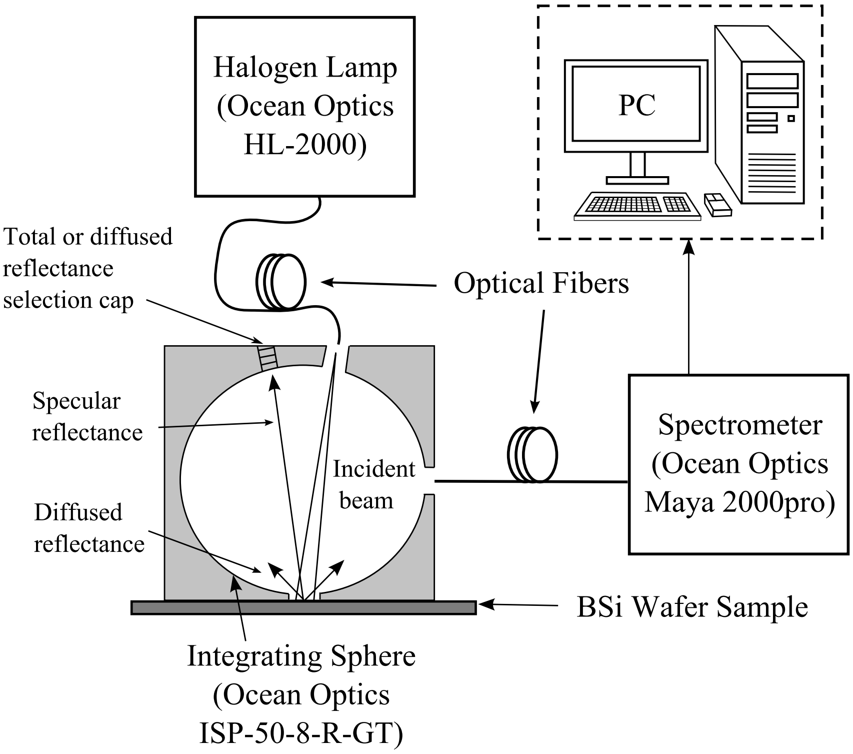

**Figure 3.2.** BSi sample reflectance measurement setup

hemispherically.

The wavelength range of the reflectance measurements are between 450 nm and 950 nm, the area of the sample being measured is approx. 28 $mm^2$. Reflectance measurements have both specular and diffuse components.

Three spectra measurements are necessary to calculate the sample reflectance $R_{BSi}$: the dark spectrum $I_d$ where the light source is blocked, the reference spectrum $I_{ref}$ and the sample spectrum $I_{BSi}$. Considering the null dark reflectance $R_d$ and the known reference reflectance $R_{ref}$, the sample reflectance is obtained by a linear interpolation, as shown in Equation 3.2:

$$R_{BSi} = R_d + \frac{[I_{BSi} - I_d] * [R_{ref} - R_d]}{[I_{ref} - I_d]} \tag{3.2}$$

We measure the total and the diffused reflectance on BSi samples S01 and S02, by changing the integrating sphere configuration. In order to obtain the diffused reflectance the portion of the integrating sphere in the specular reflectance path is removed (Figure 3.2). Once the total and the diffused reflectance are obtained, the specular component $R^s_{BSi}$ is deduced by subtracting the diffused intensity $I^d_{BSi}$ from total intensity $I^T_{BSi}$

$$R^s_{BSi} = R_d + \frac{[(I^T_{BSi} - I^d_{BSi}) - I_d] * [R_{ref} - R_d]}{[I_{ref} - I_d]} \tag{3.3}$$

Figure 3.3 shows the total, specular and diffused reflectances of BSi samples S01 and S02.

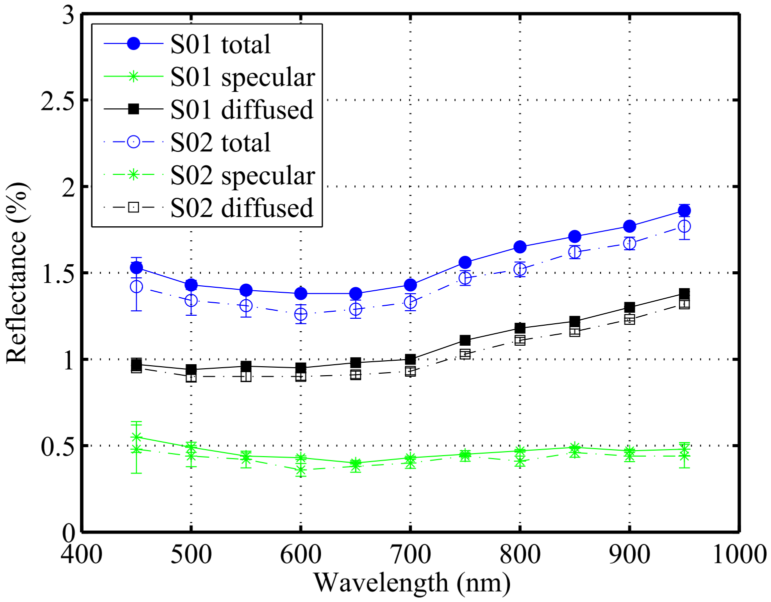

**Figure 3.3.** Reflectance measurements of BSi samples S01 and S02. Error bars represent the standard error calculated from 4 measurements on different regions of the sample.

We first of all notice that the diffused component, due to the surface roughness, is preponderant. Therefore, reflectance simulation methods based on effective medium approximations (EMA) [86, 92], which only provide the specular component, would represent only a small portion of the total reflected power thus are not suited to the modelling of BSi. The specular component is mostly constant with the wavelength whereas the diffused one increases with the wavelength. Based on the topography characterization performed in Chapter 2, both samples present similar mean aspect ratios (of 2.34 and 2.57 for BSi samples S01 and S02 respectively), which is in accordance to their close reflectance behaviours, the total reflectance of S02 being slightly lower (mean reflectance of 1.45% against 1.55% for S01). As previously reported [13], we observe with BSi samples a decrease of the reflectance when the structure's aspect ratio increases.

The specular component of the BSi reflectance can also be measured using spectroscopic ellipsometry. In collaboration with the Paris Institute of Nanoscience (INSP), we performed measurements on BSi samples S01 and S02 by ellipsometry using the setup illustrated in Figure 3.4a. The obtained results are shown in Figure 3.4b.

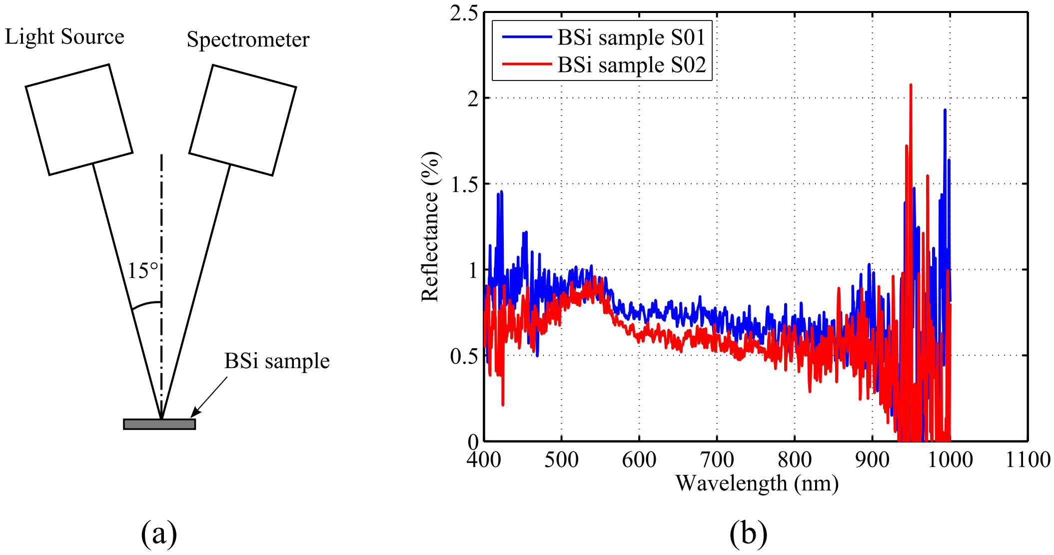

**Figure 3.4.** Specular reflectance measurements of BSi samples S01 and S02 by ellipsometry with angle on incidence of 15°.

The specular reflectances shown in Figure 3.4 were measured without any further treatment such as averaging (unlike in Figure 3.3). The strong variations observed between 800 nm and 1000 nm of wavelength is due to a lower power of the light source in this wavelength range. We notice that the specular reflectances of both BSi samples obtained by ellipsometry have similar orders of magnitude than the specular reflectances calculated from the measurements using the integrating sphere. Despite the different experimental conditions such as the angle of incidence, both measurements methods show that BSi sample S01 has slightly higher reflectance than sample S02.

## 3.2 Numerical reflectance simulation methods for periodic structures

### 3.2.1 Finite element method

Reflectance simulations in the visible light wavelength range are performed using ANSYS HFSS software. The bulk silicon material permittivity and loss tangent as a function of wavelength are based on information obtained from the literature [93] (Figure 3.5).

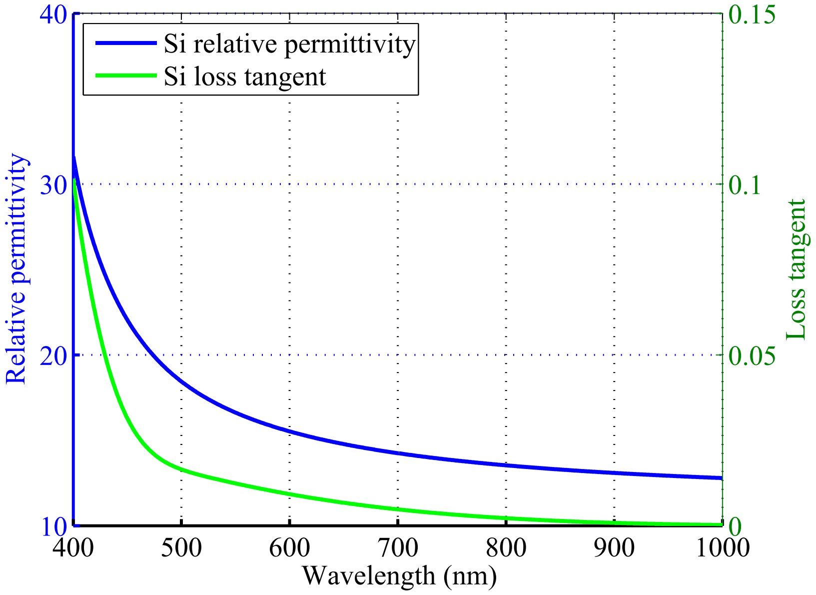

**Figure 3.5.** Relative permittivity and tangent loss of crystalline silicon obtained by ellipsometry [93].

Periodic boundaries are imposed in the side faces of the unit cell. The source consists in a plane wave with an incidence angle of 8° with respect to the wafer back surface normal vector (Figure 3.1). At the bottom of the simulated volume, an impedance condition is used to simulate the thickness of the silicon substrate of 500 $\mu$m and a perfect conductor is placed under the silicon layer to further match the conditions of the reflectance measurement setup.

The reflectance spectrum is evaluated at the top face of the cuboid denoted in Figure 3.1 as the radiation boundary. As non-polarized light is used in the measurements, the reflection coefficient $S_{11}$ as function of wavelength is evaluated for both TE and TM polarizations according to Equation 3.4. The total reflectance $R$ is obtained from the average of both polarizations (Equation 3.5). The reflectance simulations include both specular and diffused components, since the $S_{11}$ parameter is calculated using the total scattered electromagnetic fields.

$$R_{TE|TM} = |S_{11}|^2_{TE|TM} \tag{3.4}$$

$$R = \frac{R_{TE} + R_{TM}}{2} \tag{3.5}$$

### 3.2.2 Multilayered medium approximation

#### 3.2.2.1 Synthesized capacitance model

The synthesised capacitance model [86] is a method developed to calculate the reflectance of pyramidal array structures used in anechoic chambers at microwave frequency range. The unit cell structure consisting of a pyramid is transformed into layers with different refractive indexes (illustrated in Figure 3.6). In each layer the equivalent permittivity is calculated based on the amount of silicon and air, the silicon bulk permittivity and the air permittivity. Once the equivalent permittivity is obtained for all layers, the reflectance is calculated using an analytical method for the equivalent dielectric multilayered structure [94].

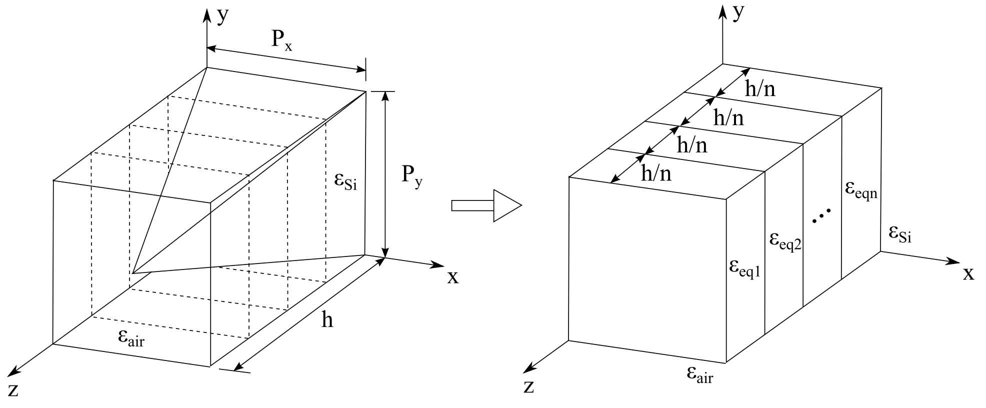

**Figure 3.6.** Pyramid approximation to an arrangement of variable dielectric constant layers

For a TE incident plane wave having an E field polarized along y-axis, the equivalent refractive index per layer is deduced by rearranging the silicon content in each layer as illustrated in Figure 3.7; the layer is considered equivalent to three capacitors ($C_{air1}$,$C_{air2}$ and $C_{Si}$) where $C_{air1}$ and $C_{Si}$ are in series and $C_{air2}$ is in parallel. The equivalent capacitance of this arrangement is expressed in Equation 3.6:

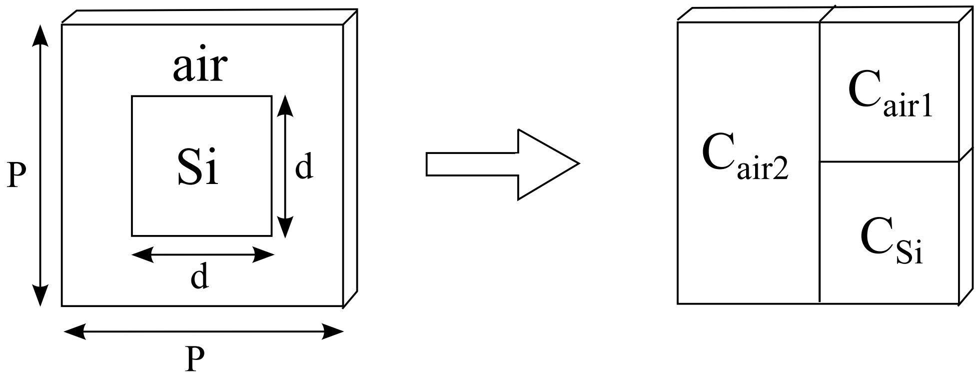

**Figure 3.7.** Effective permittivity calculation of a pyramid layer based on the synthesized capacitance model

$$C_{eq} = \left( \frac{C_{Si} \cdot C_{air1}}{C_{Si} + C_{air1}} \right) + C_{air2} \tag{3.6}$$

Based on the parallel plate expression of the capacitance we can deduce the equivalent dielectric constant $\varepsilon_{eq}$ of the layer:

$$\varepsilon_{eq} = \left( \frac{\varepsilon_{Si} \cdot \varepsilon_{air} \cdot d/(P-d)}{\varepsilon_{Si} + \varepsilon_{air} \cdot d/(P-d)} \right) + \varepsilon_{air} \cdot (P-d)/P \tag{3.7}$$

Where $\varepsilon_{Si}$ and $\varepsilon_{air}$ are the relative permittivity of Silicon and air respectively; $d$ is the pyramid cross-section size at the current layer and $P$ is the cell structure spacing (equivalent to the base size of the pyramid). Assuming permeability equal to unity, we can evaluate the equivalent refractive index $n_{eq}$ of the layer:

$$n_{eq} = \sqrt{\left( \frac{\varepsilon_{Si} \cdot \varepsilon_{air} \cdot d}{\varepsilon_{Si} \cdot (P-d) + \varepsilon_{air} \cdot d} \right) + \varepsilon_{air} \cdot (P-d)/P} \tag{3.8}$$

The same process being repeated with every layer, we finally calculate the structure reflectance by using a recursion model for multiple dielectric slabs [95].

#### 3.2.2.2 Si-air volume ratio

In this model, the refractive index of each layer is obtained with the Si–air volume ratio from a pyramidal unit cell. The specular reflectance of the unit cell is then calculated using an analytical method for the equivalent dielectric multilayered structure. The equivalent refractive index is deduced by homogenizing each layer based on its Si–air ratio using the following relation [96]:

$$\Gamma^{\mathrm{eq}}_{\mathrm{TE,TM}} = p\Gamma^{\mathrm{Si}}_{\mathrm{TE,TM}} + (1-p)\Gamma^{\mathrm{air}}_{\mathrm{TE,TM}} \tag{3.9}$$

where $\Gamma$ is the Fresnel reflection coefficient of each material and $p$ is the BSi Si–air ratio. Considering a null value of $\Gamma^{air}$ and a normal angle of incidence, the equivalent refractive index in each layer is deduced:

$$n_{eq} = \frac{1 + n_{\mathrm{Si}} - p + n_{\mathrm{Si}}p}{1 + n_{\mathrm{Si}} + p - n_{\mathrm{Si}}p}. \tag{3.10}$$

Once the equivalent refractive index is obtained for all layers, the BSi reflectance is calculated using an analytical method for the equivalent dielectric multilayered structure [94].

## 3.3 BSi modelling approaches

In this section, three methods of modelling the bi-periodic unit cell are presented. Their reflectances obtained by FEM numerical simulations are compared with measurements carried out by means of an integrating sphere.

The first approach consists of modelling small regions of the actual BSi surface topographies obtained from the three-dimensional reconstruction [16]. Periodic boundary conditions are imposed on the side faces of the small region in order to obtain an infinite surface avoiding finite surface edge effects. The simulation based on actual BSi topography is however restricted to very small regions due to the required computational effort, consequently this approach cannot handle the variations of structure height and spacing which are typical in BSi samples.

The second approach incorporates a single equivalent protuberance as unit cell that has a similar height distribution as the one obtained from a large BSi surface [81]; the better choice of the equivalent shape is also discussed. We also use single structure unit cells to perform simulations with the synthesized capacitance method [86].

In the third approach, we propose an equivalent structure made of several elementary shapes having different dimensions to include the effect of the disordered distribution of the BSi structures.

### 3.3.1 Simulation of real surface topography

The surface data obtained from BSi reconstructions with FIB-SEM tomography (Chapter 2) can be exported in various three-dimensional digital formats for further analysis. In this method, small regions of the BSi surface topography are imported in HFSS to perform reflectance simulations. The regions are chosen with different mean and STD values of height to observe the influence of different topographic parameters in the reflectance response.

The three-dimensional model top-view of BSi samples S01 and S02 are shown in Figures 3.8a and 3.8b respectively. The rectangles represent the regions of these samples which are introduced in HFSS for simulation. Each region has lateral dimensions equivalent to the mean structure spacing (estimated in Chapter 2) in the $y$-axis and half of the mean structure spacing in the $x$-axis. The final model introduced in HFSS has a duplicated structure according to symmetric boundaries conditions that allows us to perform simulations with off-normal angles of incidence. Symmetry conditions are applied on boundary surfaces parallel to the incident plane ($zx$) and periodic conditions applied on the $zy$ plane boundaries. Figure 3.8c shows the three-dimensional view of region No. 1 unit cell extracted from BSi sample S01. We note that the extracted region consists of a half structure hole; once the symmetry boundary condition is taken in account, the unit cell comprises an entire hole.

Table 3.1 shows the statistical parameters of each region and the global BSi sample parameters. The minimum, maximum, mean and STD heights ($h_{min}$, $h_{max}$, $h_{\mu}$ and $h_{\sigma}$ respectively) of each region are relative to their corresponding global BSi sample topographical parameters. The mean depth $d_{\mu}$ is deduced from $h_{max}$ minus $h_{\mu}$. The mean structure spacing

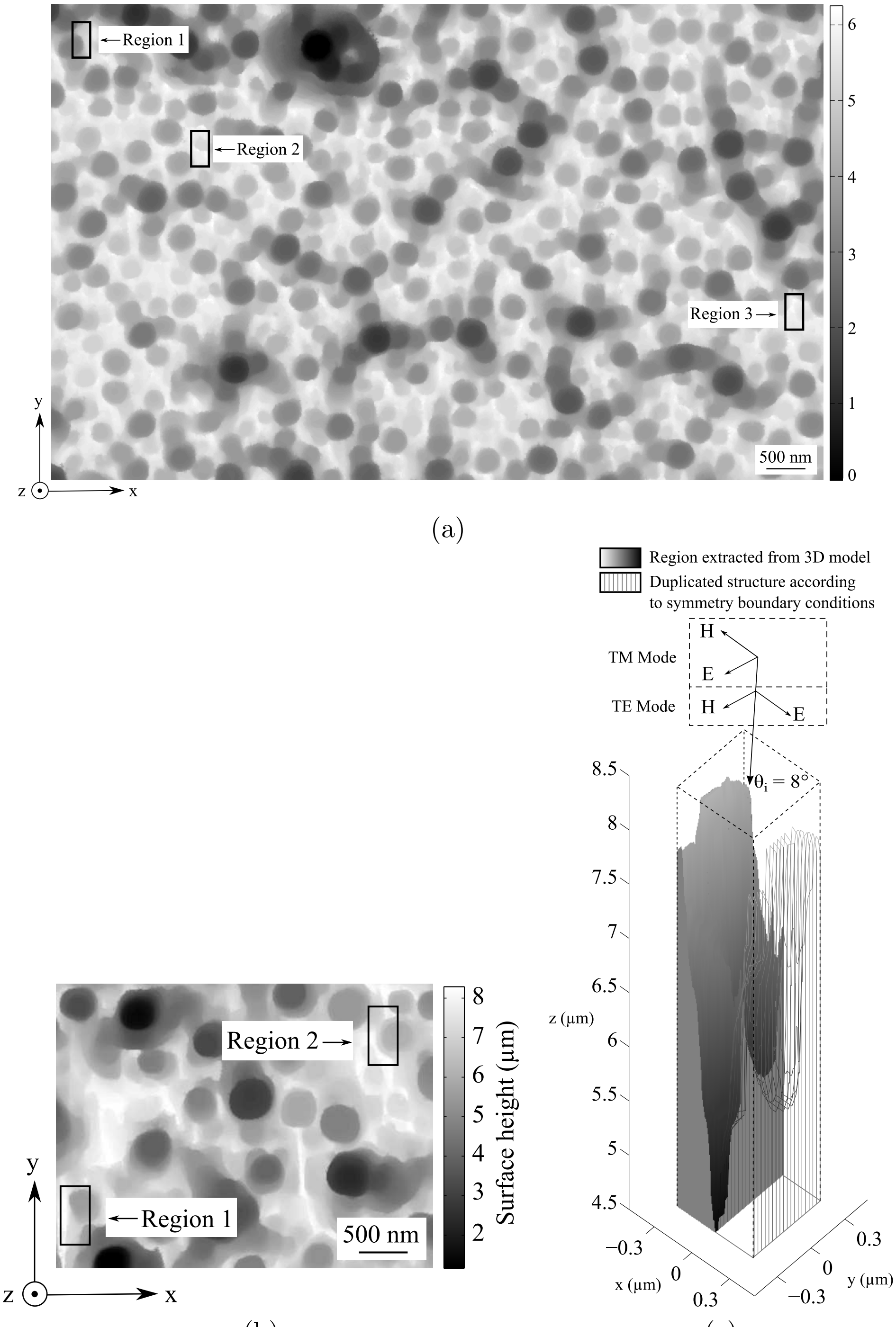

(a)

(b)

(c)

**Figure 3.8.** Top-view of a small part of BSi sample S02 (a) and sample S01 (b) models with rectangles delimiting the extracted regions used as periodic unit cell, the grey-level scale represents the global BSi sample height. (c) Three-dimensional view of region No. 1 unit cell extracted from BSi sample S01, comprising the simulated half unit cell and the duplicated half due to symmetry boundary conditions.

$P_\mu$ of each region corresponds to the unit cell size being the same as $P_\mu$ for the global BSi sample S02 but slightly smaller for BSi sample S01, due to the maximum cell volume imposed by the limited computational resources. We also calculate the mean surface normal angle $\alpha_N$ for each region and the height based on the mean surface normal angle ($h_N = \tan(\alpha_N) * P_\mu/2$).

**Table 3.1.** Comparison between the topographic parameters of each region with their corresponding global sample parameters.

| **Parameters** | **BSi sample S01** | | | |
|---|---|---|---|---|
| | Total | Region 1 | Region 2 | |
| $h_{min}$ ($\mu$m) | 0.00 | 4.71 | 6.01 | |
| $h_{max}$ ($\mu$m) | 8.28 | 8.28 | 8.28 | |
| $h_\mu$ ($\mu$m) | 5.54 | 6.67 | 7.07 | |
| $d_\mu$ ($\mu$m) | 2.74 | 1.61 | 1.22 | |
| $h_\sigma$ ($\mu$m) | 1.60 | 0.98 | 0.70 | |
| $\alpha_N$ (°) | 79.44 | 77.82 | 75.38 | |
| $h_N$ ($\mu$m) | 1.83 | 1.58 | 1.31 | |
| $P_\mu$ ($\mu$m) | 0.683 | 0.600 | 0.600 | |
| | **BSi sample S02** | | | |
| | Total | Region 1 | Region 2 | Region 3 |
| $h_{min}$ ($\mu$m) | 0.00 | 2.68 | 4.31 | 4.41 |
| $h_{max}$ ($\mu$m) | 6.24 | 5.64 | 6.21 | 6.21 |
| $h_\mu$ ($\mu$m) | 4.28 | 4.18 | 5.60 | 5.64 |
| $d_\mu$ ($\mu$m) | 1.96 | 1.45 | 0.61 | 0.57 |
| $h_\sigma$ ($\mu$m) | 1.07 | 0.84 | 0.31 | 0.30 |
| $\alpha_N$ (°) | 78.49 | 76.82 | 69.63 | 63.67 |
| $h_N$ ($\mu$m) | 1.02 | 0.89 | 0.56 | 0.42 |
| $P_\mu$ ($\mu$m) | 0.416 | 0.416 | 0.416 | 0.416 |

The numerical calculations of the reflectance are evaluated for a wavelength range between 450 nm and 950 nm using Equations 3.4 and 3.5. Figures 3.9a and 3.9b show the reflectance simulation of each region of BSi samples S01 and S02 respectively, compared with measurements obtained experimentally.

First, we notice the differences between the simulated reflectance of the regions in the same BSi sample that reflect the influence of the structure heterogeneity in the overall response of a larger surface composed by structures with different dimensions and shapes. In addition, we observe for both samples, the decrease of the average reflectance response with the increase of each region STD height $h_\sigma$. In agreement with previous published results [81], the average reflectance is decreased, when the region's heights present a large dispersion.

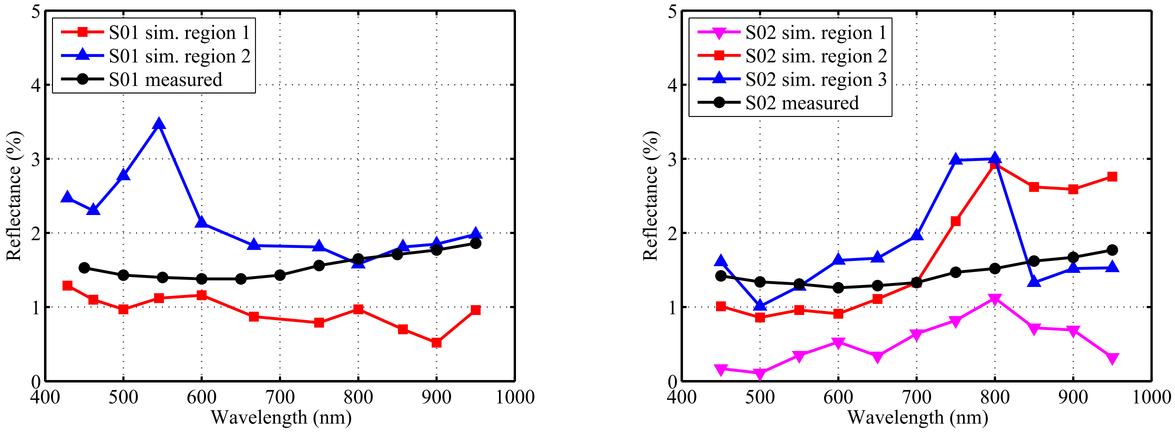

(a) (b)

**Figure 3.9.** Reflectance simulation of small regions based on real topographic data of BSi sample S01 (a) and BSi sample S02 (b) compared with their respective reflectance measurements

Additional differences between simulations and measurements such as the presence of peaks in the simulated reflectance curves, the tendency of the curves and the agreement of the reflectances observed only for small wavelength ranges again suggest that the size of the regions (equal to the mean structure spacing) is not large enough to represent the behaviour of the entire BSi sample. If the size of the evaluated region were incremented then the local geometrical properties would approach the global ones and therefore the reflectance matching improves. However, since larger samples cannot be evaluated with FEM due to large memory requirements, an alternative solution is to model an equivalent unit cell structure based on the statistical parameters of the entire BSi sample.

### 3.3.2 Simulation of a single-structure cell model

In earlier studies, cone shapes have been used as a unit cell to represent the BSi sample [81], with dimensions based on measurements of cross-section SEM micrographs of the BSi sample. However, qualitative observations and the topographic characterization performed in Chapter 2 demonstrate that the characteristic shapes observed in the BSi samples consist of a network of holes “drilled” in the sample.

In this section we determine a more suitable shape for the equivalent bi-periodic unit cell, based on the similarity of height distribution between the equivalent shape and the entire BSi sample. Once the shape is selected, we calculate their dimensions based on the topographic parameters (height and structure spacing) obtained in Section 2.4 of each BSi sample.

We proceed to compare the height distribution of different geometrical shapes with the ones obtained from BSi samples. The normalized height distributions of BSi samples S01 (Figure 3.10a) and S02 (Figure 3.10b) are compared with a cone and an inverted cone.

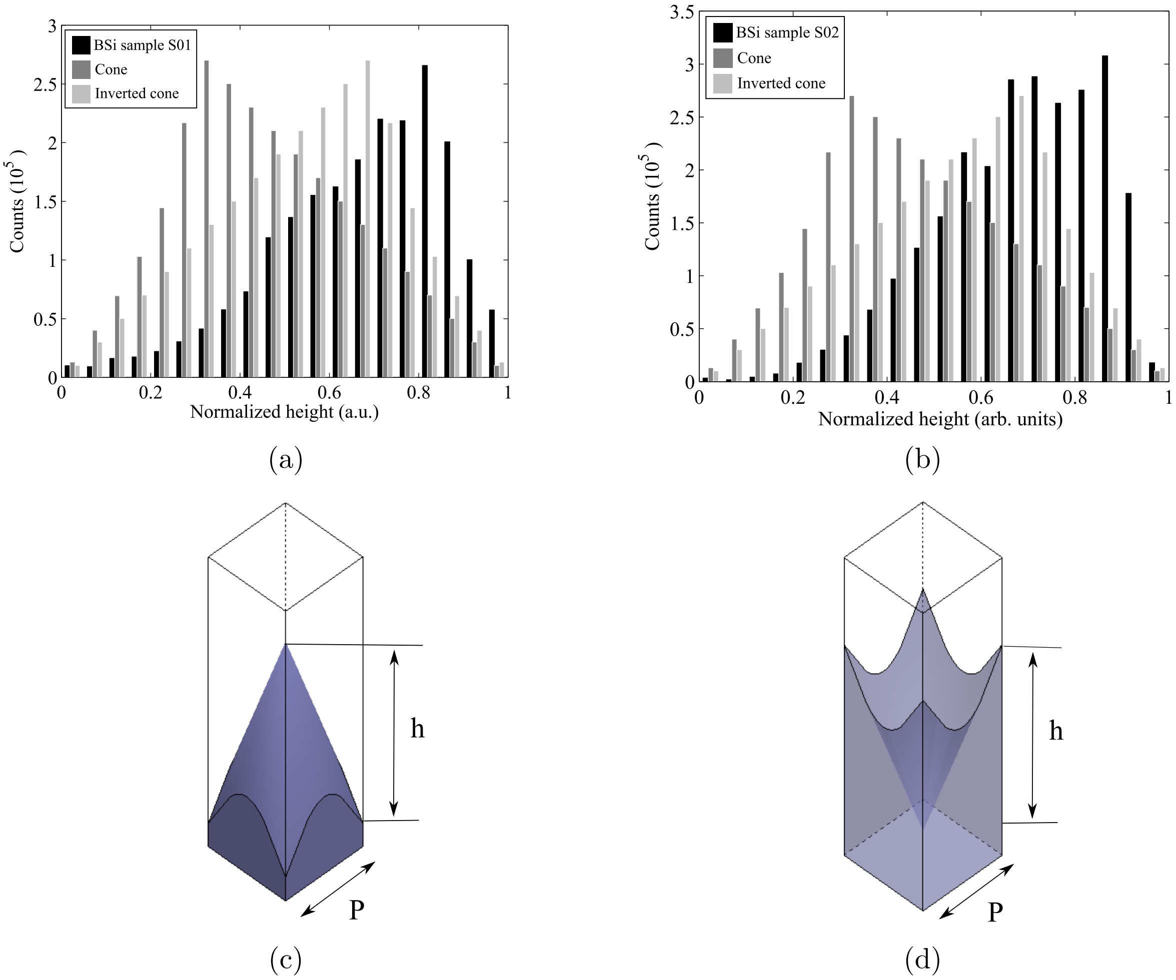

(a) (b)

(c) (d)

**Figure 3.10.** Normalized height distributions comparison of BSi sample S01 (a) and S02 (b) with a cone and an inverted cone; three-dimensional view of the cone structure (c) and the inverted cone structure (d)

Since the unit cell is inserted in a bi-periodic squared structure, the cone and inverted cone structures are truncated in a cuboid, to allow the assignment of periodic boundaries on vertical surfaces as shown in Figures 3.10c and 3.10d. Since no planar surfaces are observed in

BSi samples, the cone diameter $d$ is fixed to the structure spacing $P$ to avoid planar surfaces between conic structures.

In Figures 3.10a and 3.10b, we find a greater similarity between the normalized distributions of the inverted conic structure and both BSi samples than the conic structure.

Using the inverted cone as the equivalent structure shape, we proceed to determine its dimensions based on the global BSi topography data. Three different heights are defined for the equivalent structure: the first one is based on the global mean depth of the structure $d_\mu$, the second height $h_N$ is based on the mean surface normal angle $\alpha_N$ and the third height corresponds to the standard deviation (STD) of the total BSi height distribution $h_\sigma$. The reasoning behind the use of the STD lies in the strong variation of the local mean height along the surface discussed in Section 2.4.1 of Chapter 2. By using only the global mean depth, the effects caused by the small height variations above and below the mean value are not taken in account in the simulation. The width of the unit cell structure is defined based on the mean structure spacing of the total BSi sample (Table 3.1).

Having determined the structure dimensions, the simulated reflectance of the equivalent structures of BSi samples S01 (Figure 3.11a) and S02 (Figure 3.11b) are compared with their respective BSi reflectance measurement. As referential information we also include the simulation of a conic structure with height equivalent to $h_\sigma$.

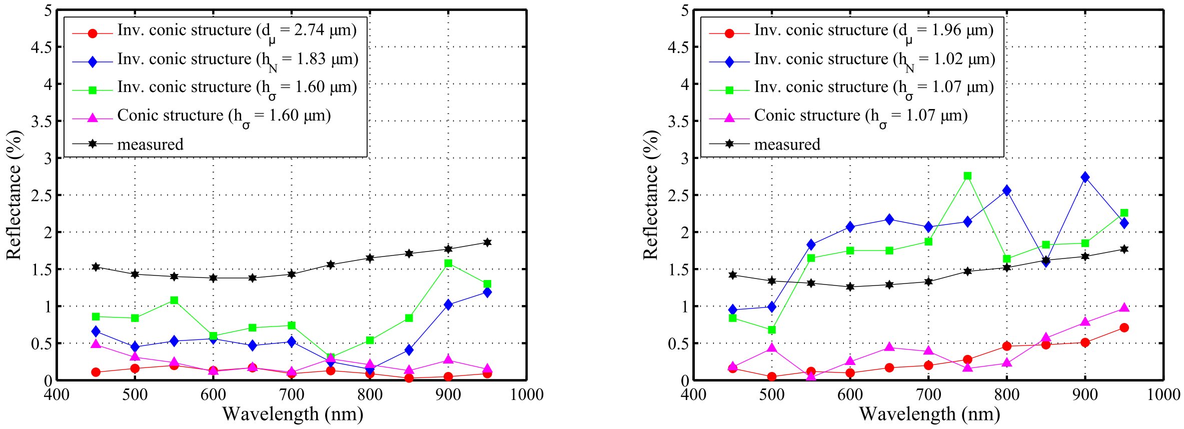

**Figure 3.11.** Reflectance simulations of equivalent structure cells based on statistical data from BSi samples S01 (a) and S02 (b) compared with measurements.

**Table 3.2.** Mean reflectance calculations of simulations and measurements for single structure cells based on BSi samples S01 and S02, evaluated between wavelength 450 nm and 950 nm.

| Inverted cone structure | **BSi sample S01** | **BSi sample S02** |
|---|---|---|
| Mean R% Simulation ($d_\mu$) | 0.11 | 0.29 |
| Mean R% Simulation ($h_N$) | 0.56 | 1.93 |
| Mean R% Simulation ($h_\sigma$) | 0.85 | 1.72 |
| Mean R% Measurement | 1.55 | 1.45 |

In Figure 3.11 we observe a poor agreement between the reflectance of the single inverted cone structure with height based on the global mean depth $d_\mu$ and the reflectance measurements; however, the structures with heights based on the mean surface normal angle $h_N$ and global STD of height $h_\sigma$, both provide better agreement with the reflectance measurements in both BSi samples. Among these results, the BSi equivalent structure with the height based on the global height STD is the one that gives best match over the studied wavelength range (Table 3.2). We also observe that between the cone and inverted cone structures with same dimensions (equivalent to $h_\sigma$), the inverted cone provides an improved agreement with the measured reflectance than the conic structure. This is expected due to the improved matching of the height distributions between the inverted cone and the BSi sample observed in Figures 3.10a and 3.10b.

Although the tendency of the simulated curves obtained with inverted cones agrees with their corresponding measurements, some discrepancies or fluctuations are still observed at certain wavelengths. These discrepancies reflect the remaining difference of the height distribution between the equivalent shape and the BSi sample which is limited to the single structure degrees of freedom (structure height and average spacing). In addition, the interferences caused by the perfectly periodic single structure cells result in a reflectance that is more sensitive to frequency variation, whereas interferences in non-periodic BSi samples are expected to be less strong.

In order to overcome these discrepancies, in Section 3.3.3 an equivalent unit cell consisting of multiple structures is presented, where variations of the inverted cone height and diameter are introduced in order to better match the BSi non-periodic nature.

### 3.3.3 Simulation of a multiple-structures cell model

To include the disordered distribution characteristic of BSi samples in simulations, an equivalent multi-structure unit cell is modelled consisting of 4 inverted cones with variable dimensions based on large scale standard deviations of the structure spacing distribution calculated from the total BSi sample. Figure 3.12 illustrates the arrangement of four individual inverted cones in one multi-structure unit cell.

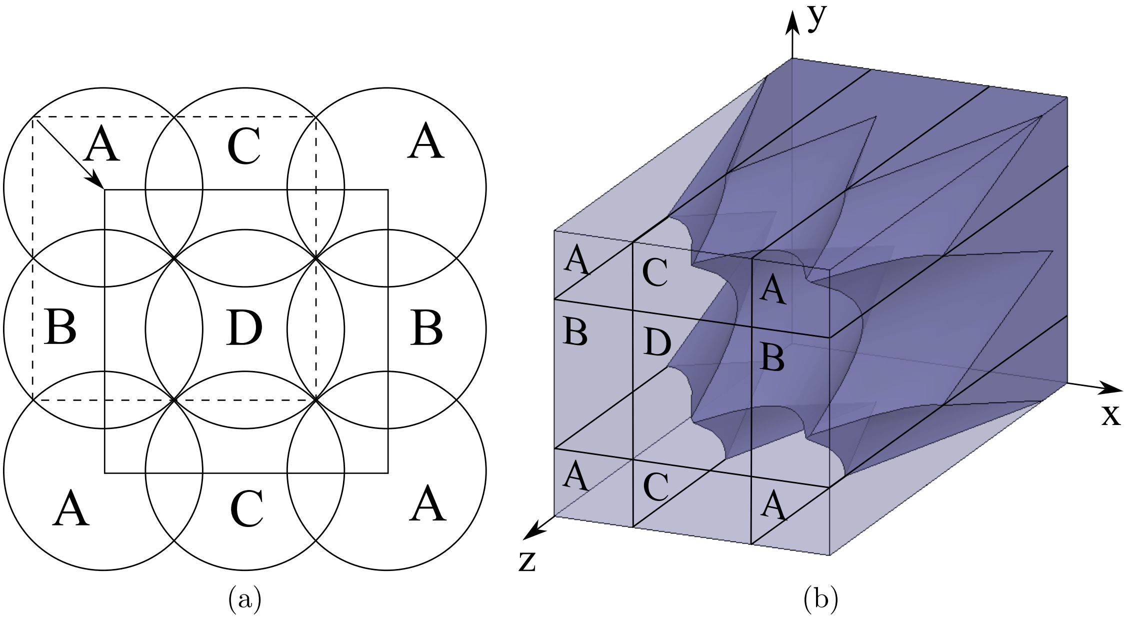

**Figure 3.12.** Representation of multi-structure cell consisting of 4 inverted cones with different dimensions: (a) Top view of the 4 cones structures where the unit cell (represented by the dashed square) is displaced by a half of the structure spacing in order to have a symmetrical structure independently of the cone dimensions. (b) three-dimensional view of the unit cell structure modelled in HFSS

Variations are introduced in each structure's height and diameter that forms the multi-structure cell while maintaining (on the entire simulated cell) the same height mean and height STD as in the single structure unit cell defined in Section 3.3.2. Based on the analytical definitions of the statistical mean and STD, we proceed to calculate the height and diameter of each structure for two different multi-structure unit cell configurations. The results of these calculations are presented in Table 3.3. Only BSi sample S02, presenting the lower reflectance, is considered in this section.

The amount of disorder introduced in the multi-structure unit cell is based on surface homogeneity study made on the BSi samples, presented in Section 2.4.6 of Chapter 2. As previously explained, in this study we calculate the variations of the statistical parameters of BSi in different regions with dimensions of three times the value of the global mean structure spacing. Followed by the calculation of the mean structure spacing and the STD between each region, we set the structure spacing standard deviation $P_\sigma$ (being 38.22 nm for BSi sample S02) as the STD of structure spacing in the multi-structure cell calculations presented in Table 3.3.

**Table 3.3.** Multi-structure cell dimensions based on BSi local variation of surface topography

| $1^{\text{st.}}$ **case** | $2^{\text{nd.}}$ **case** |
|---|---|
| $AR = h_\sigma / P_\mu$ | $AR = h_\sigma / P_\mu$ |
| $d_A = P_\mu$ | $d_A = P_\mu$ |
| $d_B = P_\mu + \sqrt{2} * P_\sigma$ | $d_B = P_\mu - 6/\sqrt{14} * P_\sigma$ |
| $d_C = P_\mu - \sqrt{2} * P_\sigma$ | $d_C = P_\mu + 2/\sqrt{14} * P_\sigma$ |
| $d_D = P_\mu$ | $d_D = P_\mu + 4/\sqrt{14} * P_\sigma$ |
| $h_A = AR * d_A$ | $h_A = AR * d_A$ |
| $h_B = AR * d_B$ | $h_B = AR * d_B$ |
| $h_C = AR * d_C$ | $h_C = AR * d_C$ |
| $h_D = AR * d_D$ | $h_D = AR * d_D$ |
| Where:<br>$h_\sigma$ = 1.07 $\mu$m (Standard deviation of height)<br>$P_\mu$ = 0.42 $\mu$m (Mean structure spacing)<br>$P_\sigma$ = 38.22 nm (STD structure spacing) | |

The diameter $d$ of each inverted cone is calculated according to the relation defined by the multi-structure configuration; since the cone aspect ratio $AR$ is maintained fixed, the height of each structure can be deduced from its aspect ratio and its base diameter. The calculations based on the analytical definition of mean and STD do not take into account the overlapping between structures in a squared multi-structure unit cell, therefore the dimensions are manually adjusted to ensure a perfect match of the mean and standard deviation of heights with respect to the single structure cell. Table 3.4 shows the dimensions of the multi-structure cells before and after the adjustment for matching the mean and STD of height.

Figure 3.13 shows the heights distributions of the two multi-structure cells configurations

**Table 3.4.** Multi-structure cell dimensions before and after the adjustment for mean and STD of height

| | **$1^{\text{st.}}$ case** | | **$2^{\text{nd.}}$ case** | |
|---|---|---|---|---|
| | Calculated | Adjusted | Calculated | Adjusted |
| $d_A$ | 0.416 | 0.4426 | 0.416 | 0.4258 |
| $d_B$ | 0.4701 | 0.4701 | 0.3547 | 0.3547 |
| $d_C$ | 0.3619 | 0.3619 | 0.4364 | 0.4364 |
| $d_D$ | 0.416 | 0.416 | 0.4569 | 0.4569 |
| $h_A$ | 1.07 | 1.0791 | 1.07 | 1.0575 |
| $h_B$ | 1.209 | 1.146 | 0.9124 | 0.8810 |
| $h_C$ | 0.931 | 0.8825 | 1.1225 | 1.0839 |
| $h_D$ | 1.07 | 1.0143 | 1.1751 | 1.1347 |

compared to the single structure and the BSi sample S02. We observe that due to the calculations based on the definition of mean and STD, we are able to produce several multi-structured cell configurations with almost the same distribution as the single structure. Following the cells design, we introduce them in HFSS to simulate their reflectance.

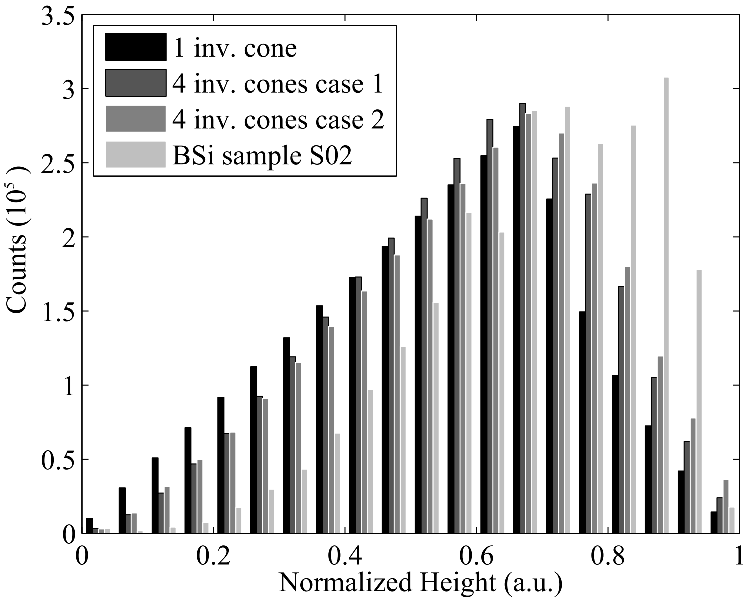

**Figure 3.13.** Comparison of normalized heights distributions of the single and multi-structure inverted cone unit cells with the height distribution of the BSi sample S02.

Figure 3.14 and numerical results in Table 3.5, compare the simulated reflectance of the

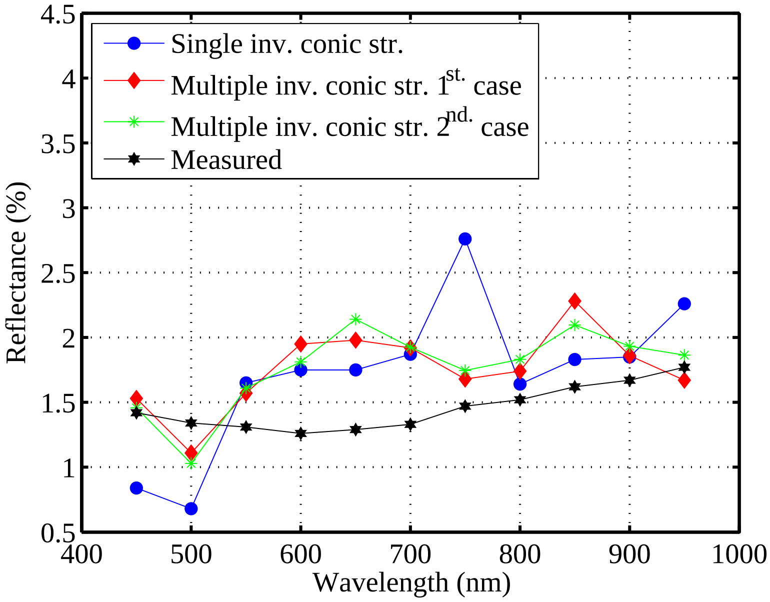

**Figure 3.14.** Comparison of reflectance simulation with single and multiple equivalent structures with their respective measured reflectance based on dimensions obtained from BSi sample S02

multi-structure unit cells with the one obtained from the single structure along with the BSi sample reflectance measurement. We observe that by introducing some height disorder while maintaining the same topographic parameters of the single structure unit cell, the mean reflectance of the multi-structure cells are almost the same as the single structure cell. However, smoother reflectance responses are observed in the multi-structure cells that approach the tendency of the BSi measurement.

This improvement is quantified in Table 3.5 with the normalized root-mean-square error (NRMSE) and STD values. Despite the tendency improvement with respect to measurements, small fluctuations are still observed which could be removed by incrementing the amount of disorder or using a more complex model. Moreover, using the 8 degrees of freedom provided by this model, multi-structure unit cells can be designed with a goal on their height distributions outcome to be similar to the real BSi samples; a better agreement with measurements results is expected in this case.

**Table 3.5.** Mean and STD calculations for: single-structure and multi-structure simulations and BSi sample S02 measurements. NRMS deviation of each simulated structures from measurements for a wavelength range between 450 and 950 nm.

| | **Mean R%** | **STD R%** | **NRMSE (%)** |
|---|---|---|---|
| Single inv. cone str. | 1.72 | 0.57 | 0.33 |
| Multiple inv. cone str. $1^{\mathrm{st.}}$ case | 1.75 | 0.30 | 0.24 |
| Multiple inv. cone str. $2^{\mathrm{nd.}}$ case | 1.77 | 0.31 | 0.24 |
| Measured | 1.45 | 0.17 | — |

### 3.3.4 Multilayered medium approximation

#### 3.3.4.1 Inverted Pyramid

Since the height distribution of a cone and a pyramid structures are similar, we perform simulations (at normal angle of incidence) with the effective medium approximation based on the synthesized capacitance model and the Si–air volume ratio using inverted pyramid structures. The dimensions of these structures are based on topographic parameters of BSi samples S01 and S02 obtained in Section 2.4 of Chapter 2. The results are compared with specular measurements obtained by ellipsometry (Figure 3.15).

The disagreement observed between the simulations of inverted pyramids using the multilayered media approximations and the measurements is due to the unit cell structure spacing being in the same order of magnitude to the wavelength ($P/\lambda \sim 1.7$ and 1 for BSi samples S01 and S02 respectively) whereas the equivalent media approaches are only suited in cases when the structure spacing is less than the wavelength of the source ($P/\lambda < 0.3$) [86].

#### 3.3.4.2 Real surface topography

In this Section, the same analytical procedure to calculate the specular reflectance is used, but instead of using the pyramid unit cell, we use the real surface topography presented in Section 2.4.2 of Chapter 2. Figure 3.16 shows the specular reflectance simulations of BSi samples S01 and S02 (at normal angle of incidence) obtained with both equivalent multilayered material approaches and compared with specular reflectances measured by ellipsometry (presented in Section 3.1).

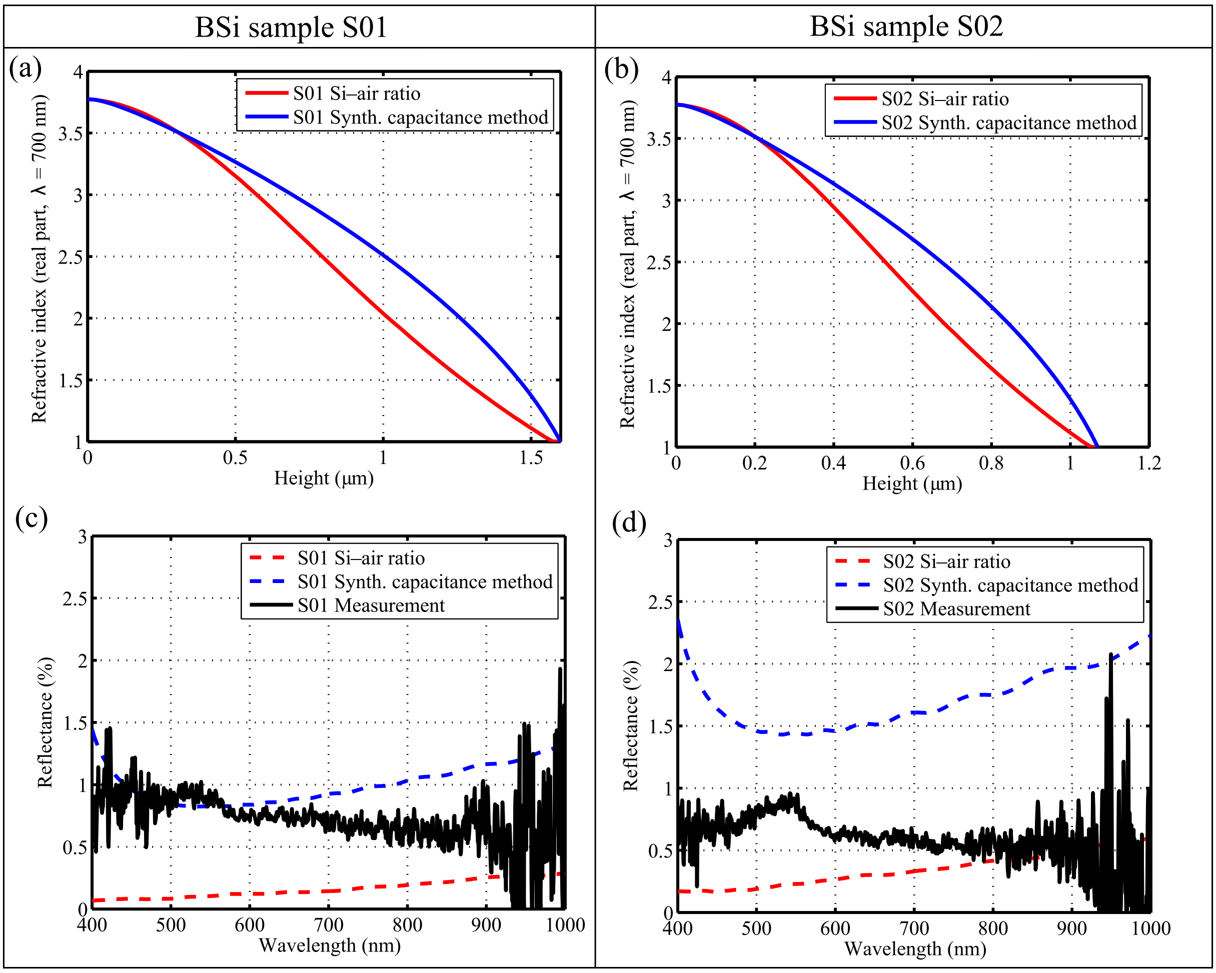

**Figure 3.15.** Specular reflectance simulations and measurements of inverted pyramid structures based on BSi samples $h_\sigma$: Real part of refractive index as function of structure height for (a) BSi sample S01 and (b) BSi sample S02. Simulations, being performed with the multilayered medium approximation method with both synthesized capacitance and Si–air ratio models, are compared with measurements for (c) BSi sample S01 and (d) BSi sample S02

From Figure 3.16, we observe that the effective medium approximation with both Si–air fill factor and synthesized capacitance models, based on real surface topography, provide specular reflectances with similar tendencies when compared to measurements performed by ellipsometry. These results suggest that by embedding the influence of the BSi structure spacing variations in the refractive index profile as a function of height, it is possible to obtain improved reflectance simulations in structures with average spacing similar to the wavelength of the source. We also observe, in both BSi samples, that the Si–air fill factor model provides better agreement to the measurements than the synthesized capacitance model.

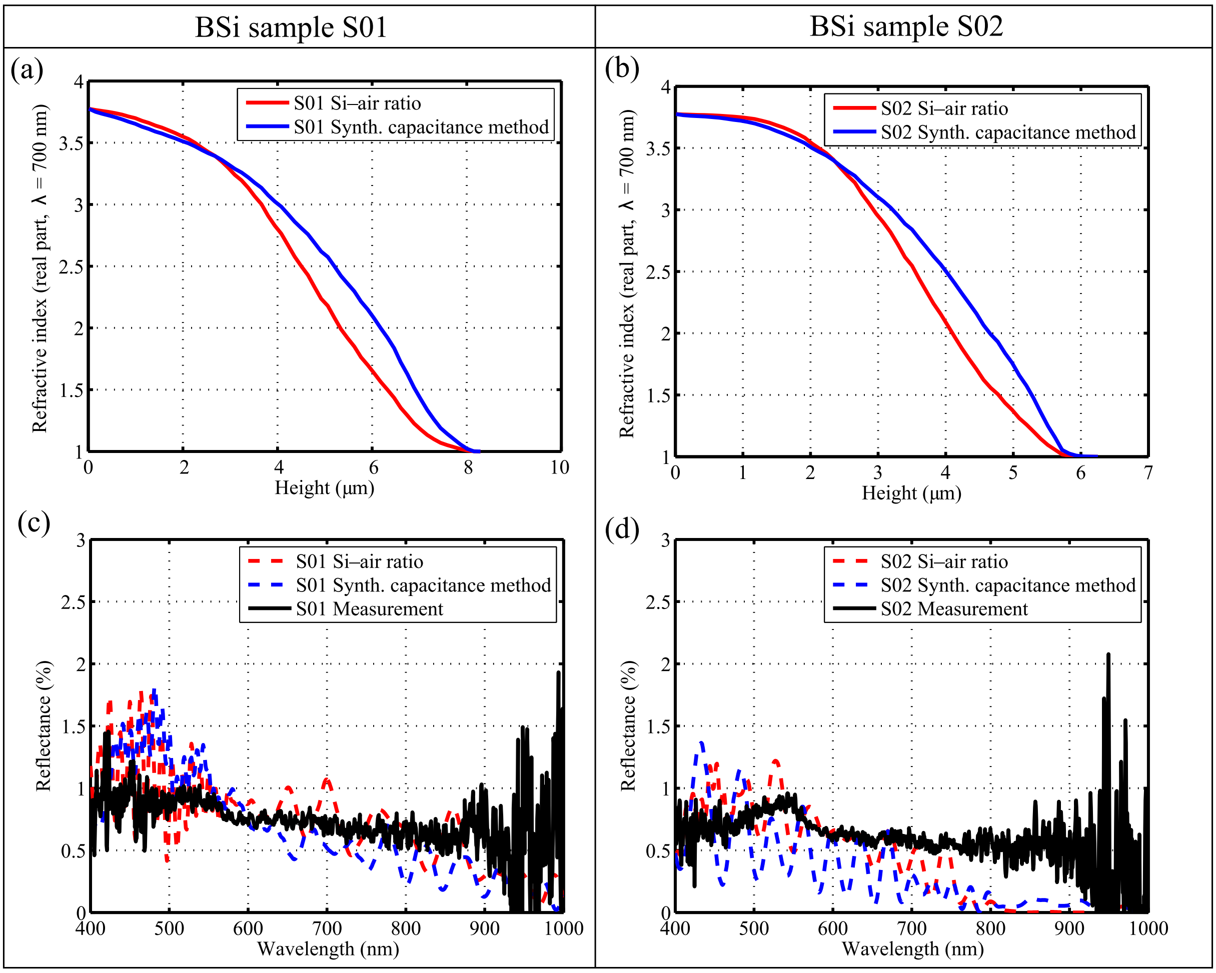

**Figure 3.16.** Specular reflectance simulations and measurements of BSi samples real surface topography: Real part of refractive index as function of structure height for (a) BSi sample S01 and (b) BSi sample S02. Simulations, being performed with the multilayered medium approximation method with both synthesized capacitance and Si–air fill factor models, are compared with measurements for (c) BSi sample S01 and (d) BSi sample S02

## 3.4 Influence of the source angle of incidence

An additional interesting aspect of BSi surfaces is their ability to reduce the reflectance independently to the incidence angle of the source light. This property is useful in solar cells applications where maximum amount of light is required independently of the position of the panel with respect to the sun. Previous publications have demonstrated the increase in power conversion efficiencies on devices by using arrays of organized periodic structures [47] and BSi surfaces [48] due to the reflectance reduction on broad angles of incidence.

Simulations at different angles of incidence (AOI) are performed in the two different configurations of the multi-structure cells presented in Section 3.3.3 using a planar wave excitation at 700 nm of wavelength, and they are compared to the single inverted conic structure cell. We demonstrate in Figure 3.17 that very low reflectance response is maintained at different angles of incidence up to 40°, followed by a slightly reflectance increase at greater AOI values for both single and multi-structure cells. In addition by introducing the disorder in the two configurations of the multi-structure cells, a lower reflectance is obtained for intermediate angles of incidence (between 30° and 60°). These results suggest that for surfaces irradiated in different AOI the total hemispherical reflectance of disordered structure distribution (typical in BSi) is reduced compared to strictly periodic structured surfaces of similar dimensions.

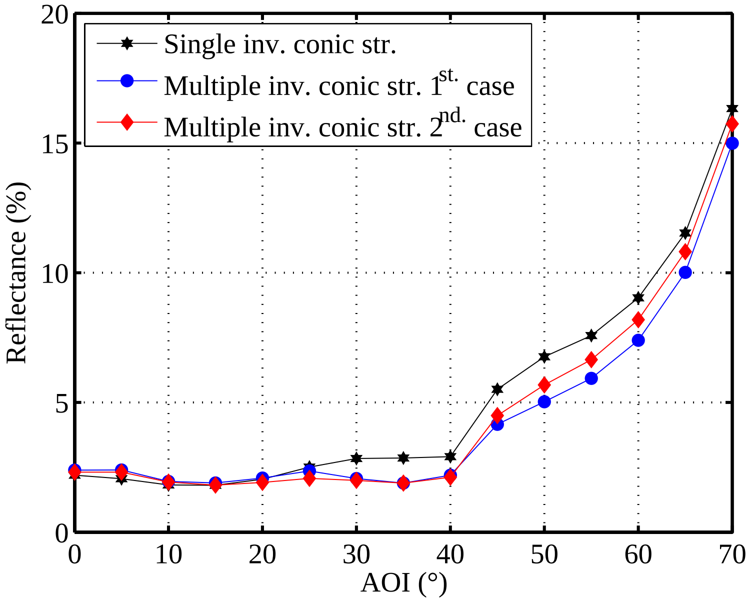

**Figure 3.17.** Comparison of reflectance simulations with single and multi-structure unit cells in function of angle of incidence ($\lambda = 700$ nm)

## 3.5 BSi transmittance and absorbance

With the support from the Paris Institute of NanoScience (INSP), we performed both total reflectance and transmittance measurements using an Agilent Cary 5000 spectrophotometer. In this case, by performing transmittance and reflectance measurements with the same samples and the same equipment, we can deduce the absorbance and observe its increase caused by the BSi structures with respect to planar Si substrates with the same material specifications. In this setup, a certified 100 % diffuse reflectance surface is used as a standard reference for both planar Silicon and Black Silicon samples. Both the reflectance $R$ and transmittance $T$ include the specular and diffuse components and they are measured in a wavelength range between 400 nm and 1000 nm. The area of the sample being measured is $\sim$3 cm$^2$. Using the measurement results, we calculate the absorbance $A$ with the relation: $A = 1 - T - R$.

We start by measuring the reflectance $R$ and transmittance $T$ of a single side polished <100> Si wafer with 500 $\mu$m of thickness (Figure 3.18a and Figure 3.18e respectively) followed by the absorbance calculation (Figure 3.18c), then we compare the measurements to analytical calculations based on refractive coefficients of intrinsic <100> Silicon obtained from the literature [93]. We also compare the reflectance $R$, transmittance $T$ and absorbance $A$ (based on measurements) of BSi sample S01 (Figure 3.18b, Figure 3.18f and Figure 3.18d respectively) with simulations made on HFSS using the single structure inverted conic cell presented in Section 3.3.2. Due to the large diameter of the spectrometer beam, it was not possible to measure BSi sample S02.

We observe from Figure 3.18 that the transmittance of both samples are negligible on the visible light wavelength range due to its large thickness (500 $\mu$m), becoming significant when $\lambda > 950$ nm; this behaviour is in agreement with previous reports [16]. We also observe that despite the amount of silicon etched during the BSi formation ($\sim$20 $\mu$m), the transmittance is lower in the BSi with respect to the planar Si surface by a factor of 2 at $\lambda = 1000$ nm. This is due to the multiple reflections caused by the microstructures which diffuses the light increasing its path length required to reach the back surface combined with the bulk silicon absorption coefficient. Finally, the absorbance increment observed in the BSi confirms that the additional

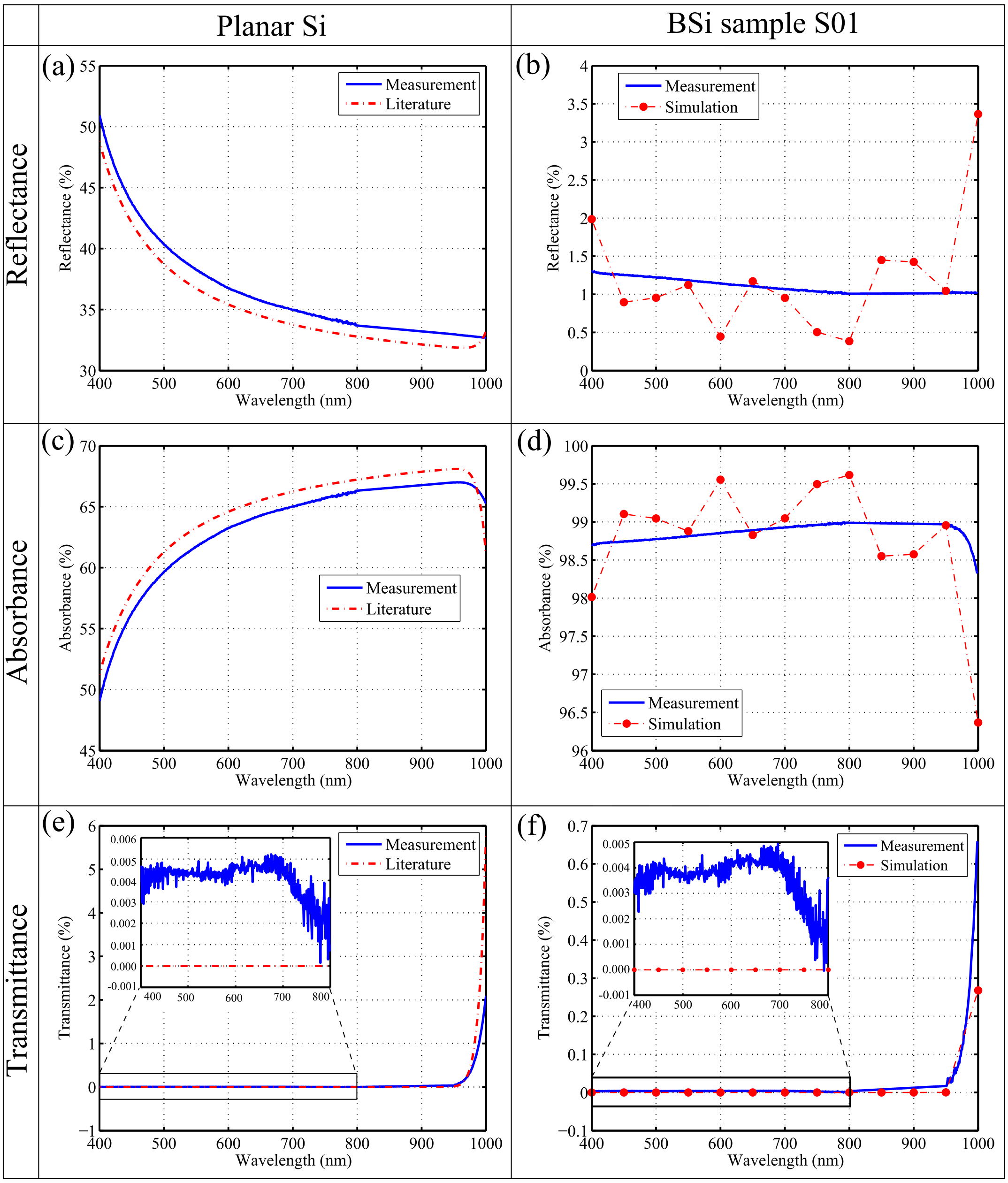

**Figure 3.18.** Optical measurements (experimental and literature) of a single side polished <100> Si wafer with 525 $\mu$m of thickness: (a) Reflectance, (c) Absorbance and (e) Transmittance. Optical simulations and measurements of BSi sample S01: (b) Reflectance, (d) Absorbance and (f) Transmittance

.

light captured by the BSi structures is not further transmitted to the back surface interface but absorbed within the material in the studied wavelength range (400-1000 nm).

The small disagreement between measurement and theory, observed on the polished silicon wafer, is probably due to differences between the silicon wafer specifications used in the literature (unknown doping level and crystalline orientation, double side polished and thickness 600 $\mu$m) and the silicon wafer used in our measurements (p-doped, <100> oriented, bulk resistivity 1 - 20 $\Omega$.cm, single side polished and thickness 500 $\mu$m). Small discrepancies observed when comparing the measurement and simulation of the BSi transmittance, can be attributed to the roughness of the unpolished Si substrate back side surface which is not taken in account in the simulation. In addition, the observed variations of the simulated reflectance with respect to measurements, being already explained in Section 3.3.2, is due to the perfectly periodic nature of the single structure cell used in the simulation.

# Chapter 4

# Static and dynamic aspects of black silicon formation

**Contents**

As mentioned in the introductory Chapter, the mechanism by which a complex topography such a BSi can be generated from a flat surface by a uniform reactive ion etching process is not currently well understood. Multiple hypotheses have been proposed regarding the formation mechanisms for BSi topography, such as micro-masks originated from native oxide or dust [16, 19, 20], or due to re-deposition of reaction products in certain areas that reinforces the passivation layer [21]. In this Chapter we present a model that is capable of simulating the entire evolution of a surface from a planar substrate to fully-developed BSi topography. We show that the observed evolution of BSi from a planar substrate can be accurately modelled by including the long-range effects of geometric occlusion (or self-shadowing), and no role for defects or micromasking.

By means of the proposed model, we study the static and dynamic aspects of BSi formation starting with initial roughness of typical polished Si surfaces, up to the later-time formation of high aspect ratio (HAR) structures. By comparing the BSi surfaces obtained from the model with experimental data, great similarity is found in several phenomena observed during the BSi formation. Consequently, this model explains in great detail the mechanism in which the instabilities of several processes occurring in cryo-DRIE can lead to the BSi formation, in contrast to previous assumptions of the influence of micro-masking effects due to substrate impurity precipitates or chamber contamination.

In the initial Section of this Chapter, we start by describing the model which simulates the three processes that occur simultaneously in cryo-DRIE, such as the passivation layer formation, the passivation layer etching and the silicon etching. The subsequent Sections comprise several static and dynamic aspects of BSi formation. In the static aspects Section, we study the influence in the variation of the simulation process parameters in the resulting BSi structures for a given etching time, and provide calculations of the silicon–air fill factor *vs.* structure height. In the dynamic aspects Section, we study the evolution of the BSi aspect ratio with process time and the structure shape transformations at different time-lapses. All the BSi structures simulations are compared with experimental data to validate the model, obtained from previous studies of the BSi formation at different cryo-DRIE parameters [97] along with BSi samples reconstructions by FIB-SEM nanotomography and time-lapsed BSi samples presented in Chapter 2. An example of the BSi formation model program written in Matlab is described in Appendix A.

## 4.1 BSi formation model

Although many parameters in cryo-DRIE (described in Chapter 2) have a direct or indirect effect on BSi formation [13, 21, 98], the model focuses on the three main processes that occur in cryogenic RIE: passivation layer formation, passivation layer etching and silicon etching. These processes, occurring simultaneously in cryo-DRIE, are discretized in the model by infinitesimal time increments, until the pre-established process time is reached.

A schematic of the BSi formation model is shown in Figure 4.1. The model data are stored in two bi-dimensional arrays ($Z_{\mathrm{SI}}$ and $Z_{\mathrm{PL}}$) corresponding to the silicon substrate height (with initial values imposed by the chosen substrate geometry), and, respectively, the passivation layer thickness as measured normal to the substrate (generally with null initial value). Because the height function $Z_{\mathrm{SI}}$ is single-valued, overhanging features (which we never observe experimentally) cannot be modelled using the current approach.

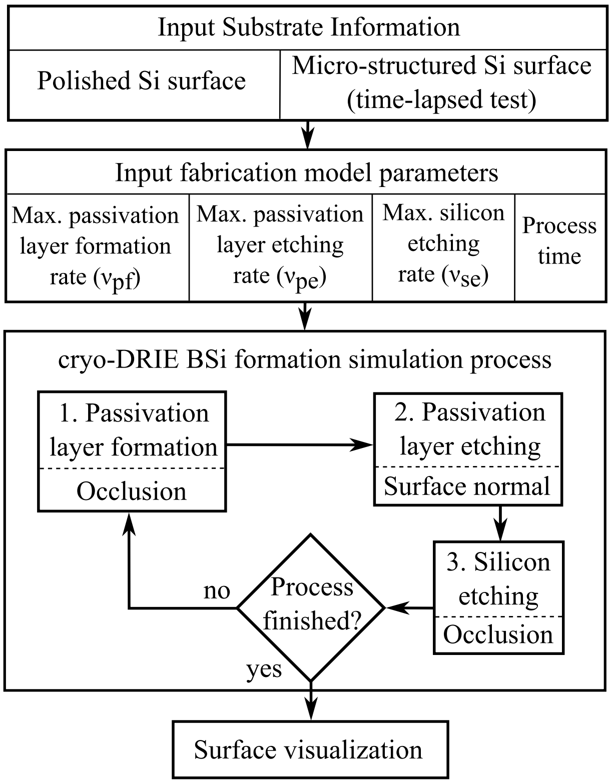

**Figure 4.1.** Flowchart diagram of BSi formation algorithm.

The main parameters to control the simulation model are: maximum passivation formation rate $v_{\mathrm{pf}}$ (related to the $O_2$ concentration and temperature), maximum passivation etching rate $v_{\mathrm{pe}}$ (related to bias voltage), maximum silicon etching rate $v_{\mathrm{se}}$ (related to $SF_6$ concentration) and total process time $t_{\mathrm{proc}}$.

Different initial substrate geometries have been used: that of a polished silicon wafer with residual roughness based on characterizations with atomic force microscopy (AFM), and that of BSi obtained at early stages of time-lapse etching/SEM grey-scale imaging experiments. Based on AFM analysis of polished Silicon wafers an average height variation of ~0.5 nm has been reported [22], which corresponds to the typical value used in our model.

### 4.1.1 Passivation layer formation

Because the passivation layer formation depend on free diffusion of $O_2$ radicals to the substrate [21], it is more efficient in areas readily exposed to the plasma (e.g. top of features) than in areas occluded by surrounding structures (e.g. bottom of trenches and holes) as illustrated in Figure 4.2. It is important to note that at the low pressures (less than 10 Pa) that are typical in cryogenic RIE processes, the mean free path of radicals is significantly longer than the scale of BSi structures.

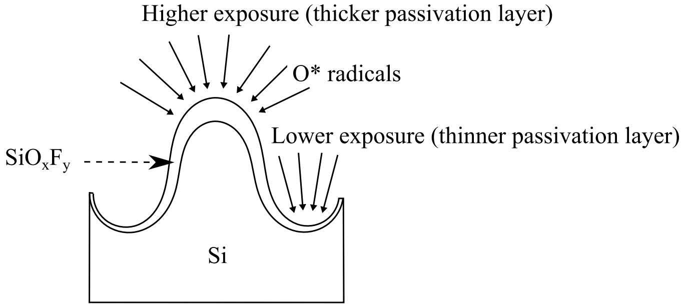

**Figure 4.2.** Diagram of passivation layer formation during cryo-DRIE.

Passivation layer formation therefore depends on the geometric occlusion level and can be considered proportional to the local solid angle $\Omega$ of unobstructed exposure to the plasma. In the model, the normalized occlusion ($\Omega' = \Omega/4\pi$) is calculated at every position of the Si surface array $Z_{\mathrm{SI}}$, using the equations presented in Section 2.4.7 of Chapter 2.

The occlusion determines the effective passivation formation rate at every point of the surface, being null for fully occluded areas and equal to the maximum passivation formation rate $v_{\mathrm{pf}}$ for fully exposed areas. While experimental measurements of passivation formation rate were not found in the literature, values of $v_{\mathrm{pf}} = 0.28$ nm/s were reported on planar surfaces without voltage bias using $SF_4/O_2$ plasmas [99], suggesting that the range of 0 - 3 nm/s is a reasonable choice.

However this effective passivation formation rate assumes a linear growth which does not correspond to general oxidation processes which are self-limiting, such as the ones observed in thermal oxidation of silicon [100]. As the passivation layer grows, it becomes progressively more difficult for the oxygen and fluoride radicals to react with the silicon lattice. This suggests that passivation layer growth slows down with time, asymptotically reaching a maximum thickness. We consider for the oxidation thickness model a sigmoid function $f$ as the self-limiting mechanism of the passivation layer growth

$$Z_{\mathrm{PL}} = f(Z_{\mathrm{PL}}^{\mathrm{lin}}) = Z_{\mathrm{PL}}^{\mathrm{max}} \left[ \frac{2}{1 + \exp\left( \frac{-2Z_{\mathrm{PL}}^{\mathrm{lin}}}{Z_{\mathrm{PL}}^{\mathrm{max}}} \right)} - 1 \right], \tag{4.1}$$

where $Z_{\mathrm{PL}}^{\mathrm{max}}$ is the maximum passivation layer thickness, $Z_{\mathrm{PL}}^{\mathrm{lin}}$ is the thickness calculated assuming a linear growth, and $Z_{\mathrm{PL}}$ is the actual thickness based on a self-limiting passivation layer formation. Figure. 4.3 shows the actual passivation layer thickness as a function of calculated thickness assuming linear growth.

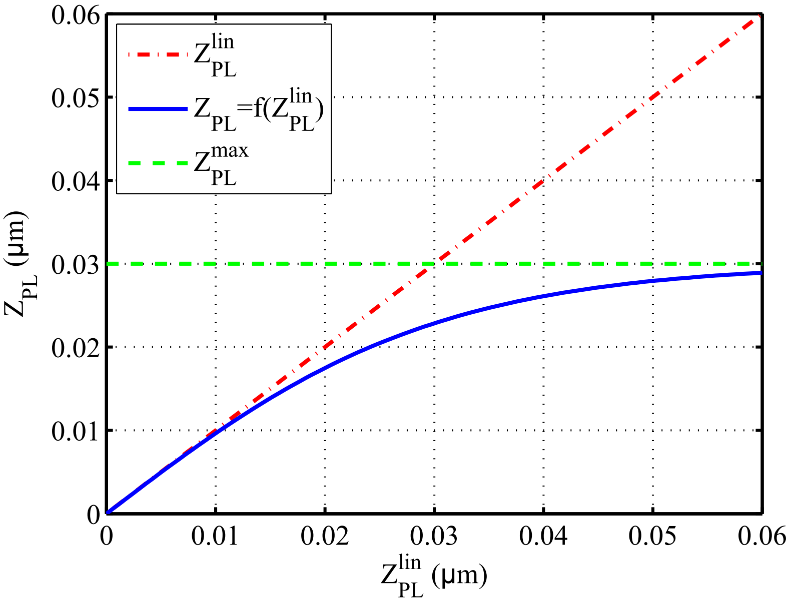

**Figure 4.3.** Actual passivation layer thickness $Z_{\mathrm{PL}}$ *vs.* calculated passivation layer thickness $Z_{\mathrm{PL}}^{\mathrm{lin}}$ assuming linear growth. The red line represents the linear growth without self-limiting process. The blue line represents the actual growth taking into account a self-limiting process to a predefined maximum passivation thickness $Z_{\mathrm{PL}}^{\mathrm{max}}$ (green line).

The passivation layer consisting of a $\mathrm{SiO}_x\mathrm{F}_y$ film that protects the Silicon from being etched, its thickness and strength are significant at temperatures less than -80 °C. Values of the maximum passivation layer thickness $Z_{\mathrm{PL}}^{\mathrm{max}}$ of 30 nm were used, based on independent measurements made by spectroscopic ellipsometry on planar surface with similar cryo-DRIE parameters [99].

### 4.1.2 Passivation layer etching

In contrast to passivation layer formation, passivation layer etching relies primarily on $\mathrm{SF}_{\mathrm{x}}^{+}$ ions being accelerated towards the sample by the plasma DC voltage bias, which physically removes the passivation layer. Such ions impact the wafer with high energies on close-to-vertical trajectories, leading to etching speeds that depend on the plasma DC bias setting but not on geometric occlusion. Since passivation layer formation is a conformal process whereas its etching is highly directional, the effective passivation thickness that is presented to the etching ions depends on local surface normal angle $\alpha_{\mathrm{n}}$, the passivation layer etching speed on horizontal surfaces being higher than on close-to-vertical walls. In our model, secondary collisions are ignored; ion-substrate interactions are assumed to have a sticking coefficient of 1.

Using the same procedure described in Section 2.4.4 in Chapter 2, the normal angle at every point of the surface is calculated by fitting a circle to the surface by the least squares method. The centre of the circle is placed at the evaluation point and its radius determines the local degree of the surface normal, being set by default to 150 nm. Following the circle fitting, the angle between its normal and the vertical axis is determined. The surface normal determines the effective passivation etching rate at every point of the surface, being nearly zero when the surface normal angle approaches 90° (vertical) and equal to the maximum passivation etching rate $v_{\mathrm{pe}}$ when the surface normal angle is 0° (horizontal).

### 4.1.3 Silicon etching

Because the silicon etching depends on free diffusion of $\mathrm{F}^{*}$ radicals to the substrate [21], it is more efficient in areas readily exposed to the plasma (e.g. top of features) than in areas occluded by surrounding structures (e.g. bottom of trenches and holes). Therefore, similarly to the passivation layer formation, the silicon etching rate also depends on the geometric occlusion level $\Omega$.

In the model, the occlusion determines the effective silicon etching rate at every point of the surface where the passivation layer is completely removed, being null in areas highly occluded and equal to the maximum silicon etching rate $\upsilon_{\mathrm{se}}$ for fully exposed areas. Typical $\upsilon_{\mathrm{se}}$ values of 30 nm/s are used, based on measurements on trenches made by cryo-DRIE without the presence of voltage bias and $O_2$ flow [99].

### 4.1.4 Model description

At each time step the algorithm computes the angle $\alpha_{\mathrm{n}}$ between surface normal and the vertical direction, as well as the plasma exposure solid angle $\Omega$ everywhere on the surface, using a computational approach similar to [83]; both calculations were previously described in Chapter 2. Simulation continues by modelling passivation layer growth where we start by calculating the preexisting passivation layer assuming a linear growth $Z_{\mathrm{PL}}^{\mathrm{lin}}(t)$. Considering that the passivation growth follows a sigmoid function $f$, we obtain $Z_{\mathrm{PL}}^{\mathrm{lin}}(t)$ by means of the inverted sigmoid function $f^{-1}$

$$Z_{\mathrm{PL}}^{\mathrm{lin}} = -\frac{Z_{\mathrm{PL}}^{\max}}{2} \log \left[ \frac{2}{(\frac{Z_{\mathrm{PL}}(t)}{Z_{\mathrm{PL}}^{\max}} + 1)} - 1 \right], \tag{4.2}$$

where $Z_{\mathrm{PL}}(t)$ is the actual preexisting thickness. The passivation layer formed during the time step $dt$ is then added to the preexisting passivation layer

$$Z_{\mathrm{PL}}^{\mathrm{lin}}(t + dt) = Z_{\mathrm{PL}}^{\mathrm{lin}}(t) + \upsilon_{pf} \Omega' dt, \tag{4.3}$$

where $\upsilon_{pf}$ is the maximum passivation formation rate and $\Omega'$ is the normalized exposure solid angle. The actual passivation layer $Z_{\mathrm{PL}}(t + dt)$ is then calculated using the sigmoid function $f$

$$Z_{\mathrm{PL}}(t + dt) = f(Z_{\mathrm{PL}}^{\mathrm{lin}}(t + dt)) = Z_{\mathrm{PL}}^{\max} \left[ \frac{2}{1 + \exp\left( \frac{-2 Z_{\mathrm{PL}}^{\mathrm{lin}}(t+dt)}{Z_{\mathrm{PL}}^{\max}} \right)} - 1 \right]. \tag{4.4}$$

The additional passivation thickness is then subtracted from the silicon height to take into account the silicon consumed in the reaction.

$$Z_{\mathrm{SI}}(t)' = Z_{\mathrm{SI}}(t) - \alpha \frac{(Z_{\mathrm{PL}}(t+dt) - Z_{\mathrm{PL}}(t))}{\cos(\alpha_{\mathrm{n}})}, \tag{4.5}$$

where $1/\cos(\alpha_{\mathrm{n}})$ accounts for the isotropic silicon consumption and $\alpha$ accounts for the difference in spatial density of silicon atoms between the silicon substrate and the newly-formed passivation layer. Since the exact composition of the passivation layer is unknown, for simplification $\alpha$ was assumed to be equal to 1. This step has only minor effect on the observed dynamics and is fully equivalent to a slight modification to the maximum passivation formation rate $\upsilon_{\mathrm{pf}}$, maximum passivation etching rate $\upsilon_{\mathrm{pe}}$ and maximum silicon etching rate $\upsilon_{\mathrm{se}}$ parameters. The amount of passivation due to the ions bombardment is then subtracted to the actual passivation layer $Z_{\mathrm{PL}}(t+dt)$.

$$Z_{\mathrm{PL}}(t+dt)' = Z_{\mathrm{PL}}(t+dt) - \cos(\alpha_{\mathrm{n}})\upsilon_{\mathrm{pe}}dt, \tag{4.6}$$

where $\cos(\alpha_{\mathrm{n}})$ accounts for the directional etching and $\upsilon_{\mathrm{pe}}$ is the maximum passivation etching rate. Since the passivation layer etching cannot be larger than the thickness of the passivation layer itself, $Z_{\mathrm{PL}}(t+dt)'$ is truncated at 0 wherever it reaches negative values, which corresponds to bare silicon being reached after a time interval $\delta t < dt$, with

$$\delta t = \frac{f(f^{-1}(Z_{\mathrm{PL}}(t)) + \upsilon_{\mathrm{pf}}\Omega' dt)}{\cos{(\alpha_{\mathrm{n}})}\upsilon_{\mathrm{pe}}}. \tag{4.7}$$

Silicon etching will only be performed in areas where no passivation layer is present, during the time interval $dt - \delta t$ that is remaining in the current simulation step. The silicon height at the end of the silicon etching step is, therefore:

$$Z_{\mathrm{SI}}(t+dt) = \begin{cases} Z_{\mathrm{SI}}(t) - \frac{\upsilon_{\mathrm{se}}\Omega'(dt-\delta t)}{\cos{(\alpha_{\mathrm{n}})}} & \text{if } Z_{\mathrm{PL}}(t+dt) = 0 \\ Z_{\mathrm{SI}}(t) & \text{otherwise.} \end{cases} \tag{4.8}$$

We note that in Eq. 4.8 the amount of silicon etched is affected by occlusion through the local plasma exposure angle $\Omega'$, whereas the isotropic nature of the etching is accounted for by the inverse dependence on $\cos{(\alpha_{\mathrm{n}})}$.

## 4.2 Static aspects of BSi formation

### 4.2.1 Influence of the simulation model parameters in the BSi structures

By varying $v_{\mathrm{pe}}$ and $v_{\mathrm{pf}}$ at fixed $v_{\mathrm{se}}$ and $t_{\mathrm{proc}}$, we simulate the growth of BSi structures from planar surfaces in different plasma conditions. The variation of $v_{\mathrm{pf}}$ being analogous to a change in the $SF_6/O_2$ gas ratio in the plasma and variations of $v_{\mathrm{pe}}$ is analogous to a change in the voltage bias.

A diagram with calculations of the mean height of the simulated sample (with 3 x 3 $\mu$m of size) is shown in Figure 4.4. We observe that the combination of high $v_{\mathrm{pf}}$ and low $v_{\mathrm{pe}}$ results in a low amount of Silicon etching (the surface is over-passivated) whereas the combination of high $v_{\mathrm{pe}}$ and low $v_{\mathrm{pf}}$ results in a high amount of uniform Silicon etching (no passivation). This behaviour is consistent with experimental observations of cryo-DRIE etching amounts at different values of $SF_6/O_2$ gas ratio and voltage bias.

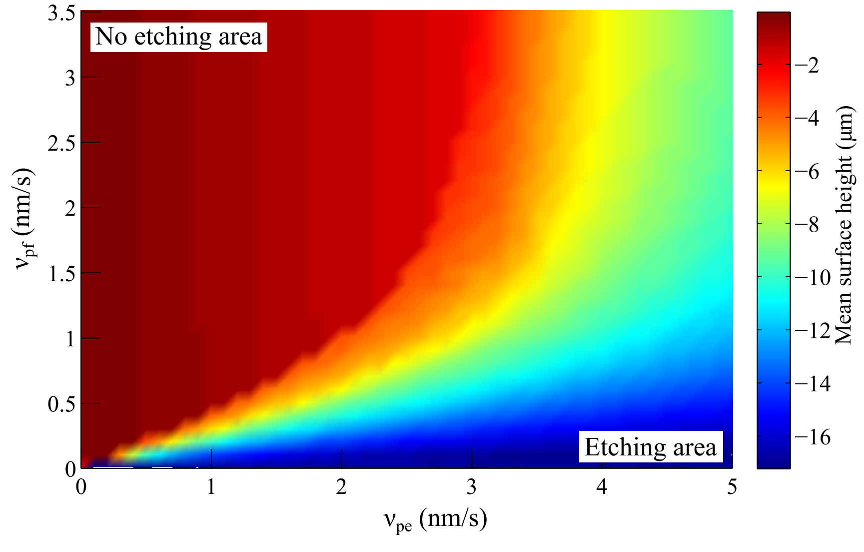

**Figure 4.4.** Diagram of Silicon etch depth dependence on $v_{\mathrm{pe}}$ and $v_{\mathrm{pf}}$, the other parameters being fixed ($v_{\mathrm{se}} = 30$ nm/s and $t_{\mathrm{proc}} = 10$ minutes).

In order to retrieve the combinations of $v_{\mathrm{pe}}$ and $v_{\mathrm{pf}}$ that produce BSi, we show the phase diagram with calculations of the aspect ratio of the surface (Figure 4.5). The area with high aspect ratio shows a delimited phase-space area where BSi is formed. From this phase diagram we select several BSi formation conditions (points *a*, *b*, *c* and *d*) to observe the structure formation at different $v_{\mathrm{pf}}$ values. The model predicts that the BSi phase disappears for combinations of large $v_{\mathrm{pe}}$ and $v_{\mathrm{pf}}$, suggesting that a gradual transition from no-etch to uniform etch behaviour is possible without the intermediate BSi phase.

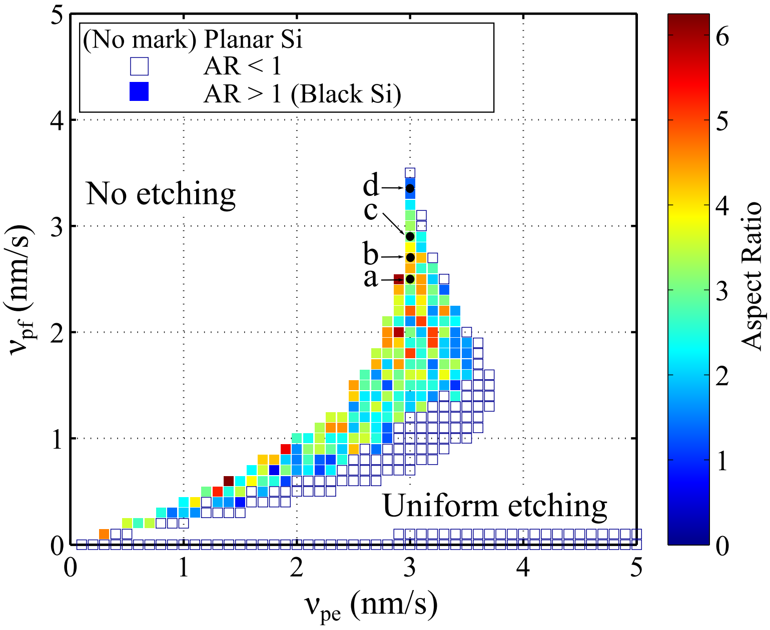

**Figure 4.5.** Phase diagram of BSi aspect ratio (AR) dependence on $v_{\mathrm{pe}}$ and $v_{\mathrm{pf}}$, the other parameters being fixed ($v_{\mathrm{se}}$ = 30 nm/s and $t_{\mathrm{proc}}$ = 10 minutes).

In Figure 4.6 we compare the cross-section views of the simulation results at various $v_{\mathrm{pf}}$ values with SEM images from a previous parametric study, where the effect of $SF_6/O_2$ on the geometry of the resulting BSi structures was measured [13]. We notice that the BSi obtained in a low oxygen content process (low $v_{\mathrm{pf}}$) consists of sharp HAR features (the surface in this case appears black, with visible light reflectivity below 1% [13]), which become progressively shallower and rounder as the oxygen content (or, analogously, $v_{\mathrm{pf}}$) is increased (in which case the surface appears greyer). This behaviour is the basis for the empirical “black silicon method”, which has been developed to determine the ideal plasma conditions for vertical etch profiles [19].

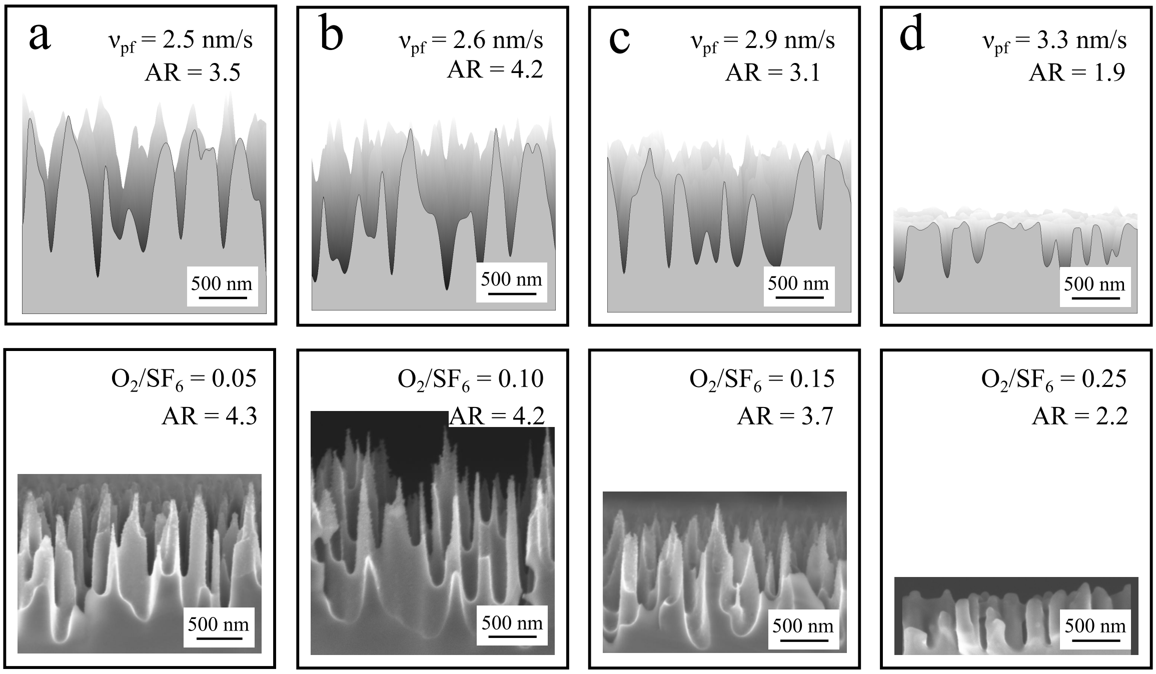

**Figure 4.6.** Top images: Cross-sectional views of simulated resulting geometries for the BSi formation at different $v_{\mathrm{pf}}$ values (2.5, 2.6, 2.9 and 3.3 nm/s respectively), being compared with SEM cross-sectional views of BSi samples (bottom images) obtained at different $O_2/SF_6$ ratios (0.05, 0.10, 0.15 and 0.25 respectively) [13].

### 4.2.2 Analysis of BSi interface transition

BSi is an example of meta-material: its low reflectivity at wavelengths larger than feature size can be explained by the smooth refractive index change between silicon and air in our effective medium approach, which inhibits reflection of incident light. The more gradual this transition, the lower the reflectance, hence the interest of HAR structures. In Chapter 2, we have measured the silicon content *vs.* depth for actual BSi samples, using an original destructive FIB nanotomography technique consisting of successive FIB slicing starting from the top of the structures, and subsequent SEM imaging of each slice. The silicon content corresponding to each slice was also determined, and a complete three-dimensional model of the BSi sample was built. In Figure 4.7 we compare the interface Si–air fill factor in function of normalized height, between simulated BSi samples with measurements obtained experimentally on BSi sample S02, showing a good agreement and proving that the simulated BSi geometry provides, indeed, a very smooth transition from silicon to air. The smoothness is a direct consequence of the characteristic features of BSi, which consist of a combination of sharp “needles” at the top and rounded “holes”

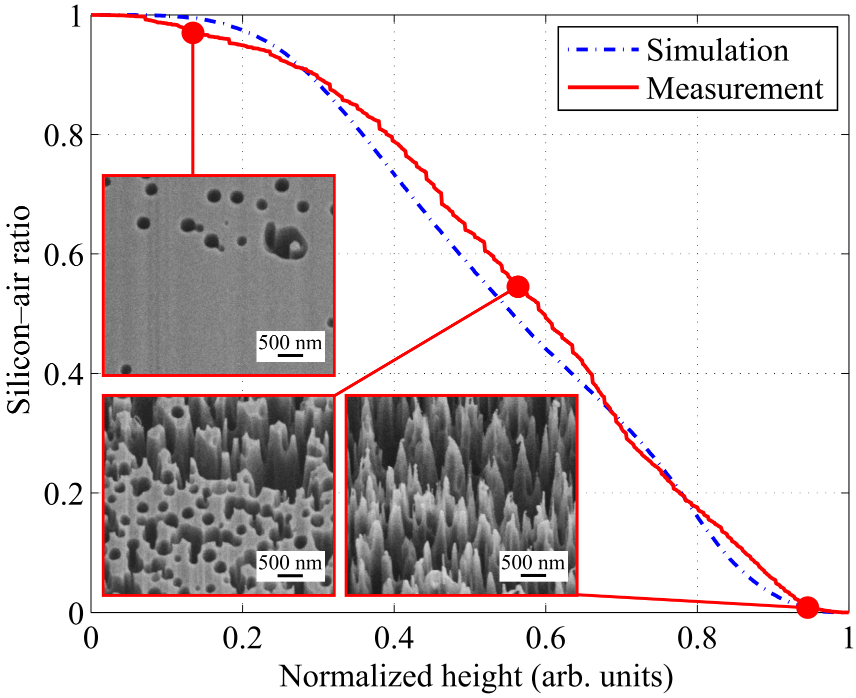

**Figure 4.7.** Silicon content *vs.* depth comparison between simulation ($v_{\mathrm{pf}} = 2.5$ nm/s, $v_{\mathrm{pe}} = 3$ nm/s, $v_{\mathrm{se}} = 30$ nm/s and $t_{\mathrm{proc}} = 10$ minutes) and BSi sample S02. The insets show three of the FIB slices used in the analysis.

at the bottom, extending to various heights and depths (as seen in the insets to Figure 4.7). It is interesting to note that such a smooth transition cannot be obtained with standard lithographic texturing especially at sub-wavelength scales. Simulations of the mean specular reflectance based on effective medium approximations (shown in Section 3.3.4 of Chapter 3), using the silicon–air fill factor obtained by FIB nanotomography, provide results consistent with actual reflectance measurements of the same sample (0.41% and 0.58% for simulated and measured mean specular reflectance respectively, with wavelength range between 400 nm and 1000 nm).

## 4.3 Dynamic aspects of BSi formation

To gain insight into the formation mechanisms of BSi, we performed two dynamic studies. We first simulated the evolution of the BSi geometry over time, followed by a series of time-lapse experiments where we introduced, as an initial substrate in the model, three-dimensional models based on short-period cryo-DRIE processed Si substrates where initial protuberances have already formed.

### 4.3.1 Time evolution of BSi Aspect Ratio

In this section, we simulate the evolution of the BSi geometry over time, starting from a flat initial substrate. The simulation data were found to be in good agreement with actual measurements performed on distinct samples subjected to cryogenic RIE at different durations, and imaged with top-view, tilt-view and cross-sectional SEM [13]. In particular, what is observed in both experiment and simulation is that BSi appears after a few minutes of process time, its aspect ratio increasing rapidly over the next few minutes before finally levelling off (Figure 4.8). It is interesting to notice that the simulations reveal the detailed structure of BSi at different stages of its evolution: at $t_{proc} = 7$ minutes, the initial roughness length scale is amplified by a factor of approximately 20, generating a network of holes at the planar surface, which then grow and densify as they are etched progressively deeper into the substrate (insets to Figure 4.8). As the etching progresses, all the flat portions of the substrate are etched away, leaving behind the network of needles characteristic of BSi, consistent with experimental observations [13, 16]. At the same time, the initial holes continue to be etched deeper into the substrate, causing the geometry observed at the bottom of the BSi structures (and illustrated in the insets to Figure 4.7). The aspect ratio then tends to stabilize as the geometry evolves towards a configuration that balances the etch rates of needles and holes. As Figure 4.5 confirms, the ultimate aspect ratio that can be obtained is process-dependent.

### 4.3.2 Time-lapse BSi formation analysis

Using the SEM micrographs and three-dimensional models reconstructions of the time-lapse BSi samples S03 and S04 (Described in Sections 2.1 and 2.3 of Chapter 2), we perform simulations where the initial topography introduced in the BSi formation model, instead of polished surfaces, consists of intermediate time-lapse three-dimensional reconstructions of BSi samples with some structures already formed. This procedure allows us to observe, dynamically, how the etching proceeds on a sample that has already developed incipient BSi. After introducing the BSi sample, we then simulate the cryogenic etching for the necessary time to reach the following time-lapse. The topography of the resulting simulated models is then compared with SEM micrographs

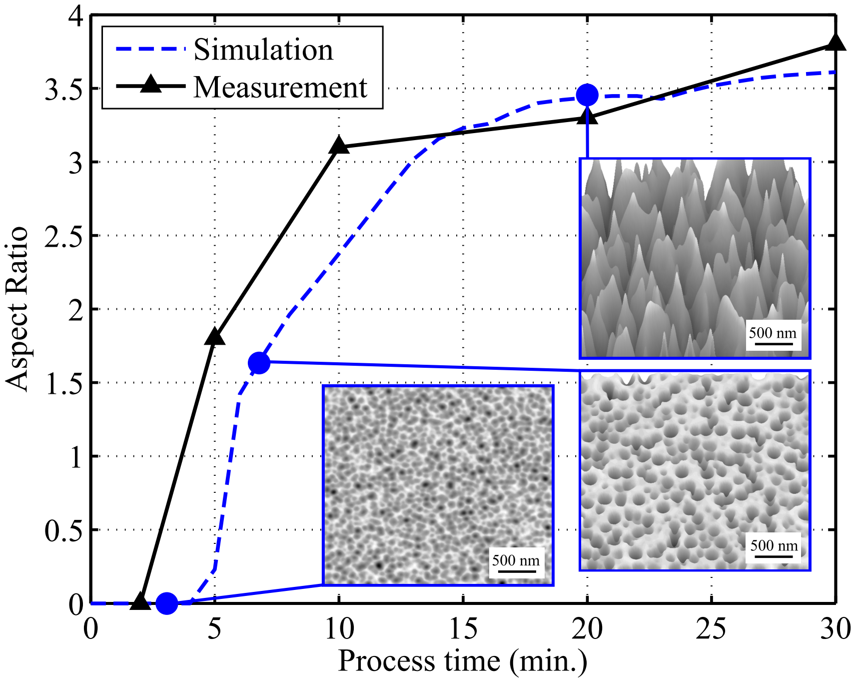

**Figure 4.8.** Dynamic study of BSi aspect ratio evolution with time, comparing simulation ($v_{\mathrm{pf}} = 3.1$ nm/s, $v_{\mathrm{pe}} = 3$ nm/s and $v_{\mathrm{se}} = 30$ nm/s) and experimental data from [13] (temperature = -120°C, inductively coupled plasma (ICP) power = 1000 W, bias voltage = -10 V, $O_2$ flow = 10 sccm, $SF_6$ flow = 200 sccm and pressure = 1.5 Pa). The insets show the simulated BSi structure at different times through the etch process.

obtained experimentally.

The three-dimensional model of the initial time-lapse ($t = 2$ min) of BSi sample S03 (Figure 4.9b) is introduced in the BSi formation program as the initial substrate, we then perform the simulation using the parameters shown in Table 4.1. The resulting simulated model (Figure 4.9d) is then compared to the final time-lapse SEM micrograph (Figure 4.9c), showing a great resemblance. We also note that the model is able to reproduce the preferential formation of new holes, which has been observed in certain regions of the SEM micrographs and have been highlighted with circles to facilitate their location.

We then proceed to repeat the simulation of the initial time-lapse three-dimensional model using BSi sample S04 ($t = 2$ min). The simulations parameters used in this simulation (Table 4.1) are slightly different from sample S03 to compensate for the difference in their cryo-DRIE fabrication parameters. The resulting geometry (Figure 4.10d) shows a remarkable resemblance to the experimental data (Figure 4.10c), including the observed development of new etch fronts at topographical saddle points.

**Table 4.1.** BSi Simulation Parameters

| **Parameters** | **BSi samples** | |
|---|---|---|
| | **S03** | **S04** |
| $v_{\text{pf}}$ (nm/s) | 2.5 | 1.8 |
| $v_{\text{pe}}$ (nm/s) | 3 | 1.2 |
| $v_{\text{se}}$ (nm/s) | 30 | 30 |
| $t_{proc}$ (Minutes) | 2 | 1 |

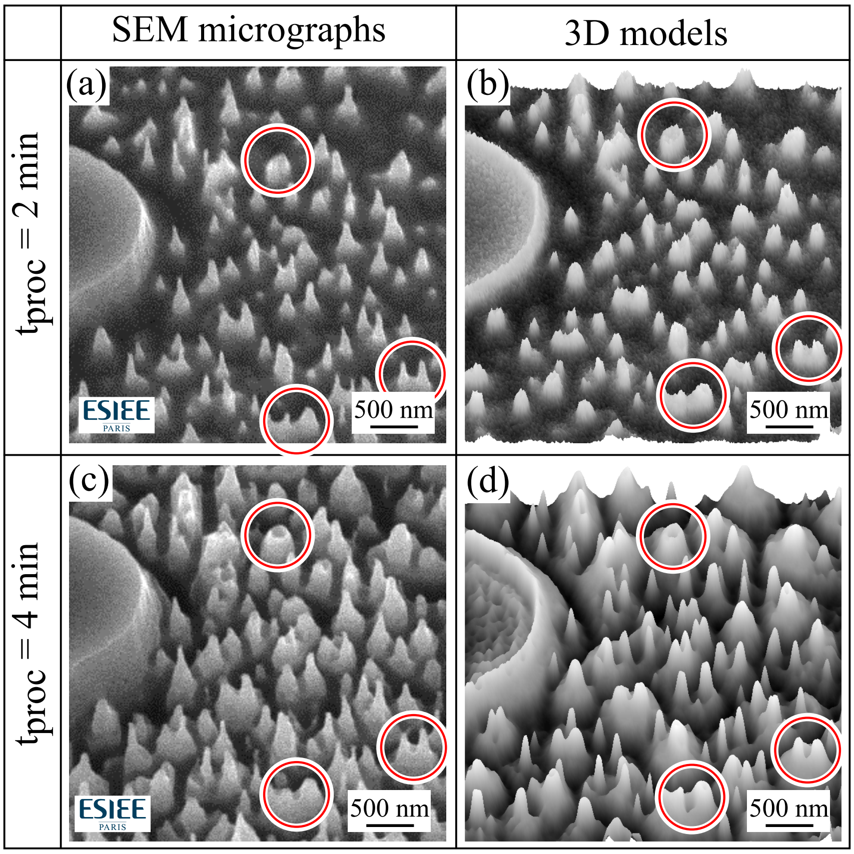

**Figure 4.9.** Time-lapse data showing the evolution of sample S03 between $t = 2$ min and $t = 4$ min of process time, for both simulation and experiment. 20° tilted view of: (a) initial time-lapse SEM and (b) three-dimensional reconstruction; (c) final time-lapse SEM (Temperature = -120°C, ICP power = 1000 W, bias voltage = -10 V, $O_2$ flow = 40 sccm, $SF_6$ flow = 200 sccm and pressure = 1.5 Pa) and (d) final time-lapse simulation ($v_{\text{pf}} = 2.5$ nm/s, $v_{\text{pe}} = 3$ nm/s and $v_{\text{se}} = 30$ nm/s). Preferentially etched holes at topographical saddle points are highlighted with circles.

## 4.4 Formation of new etch fronts

After explaining the calculation methods of the three different processes that occur simultaneously in cryo-DRIE we describe how the instability provided by the combination of

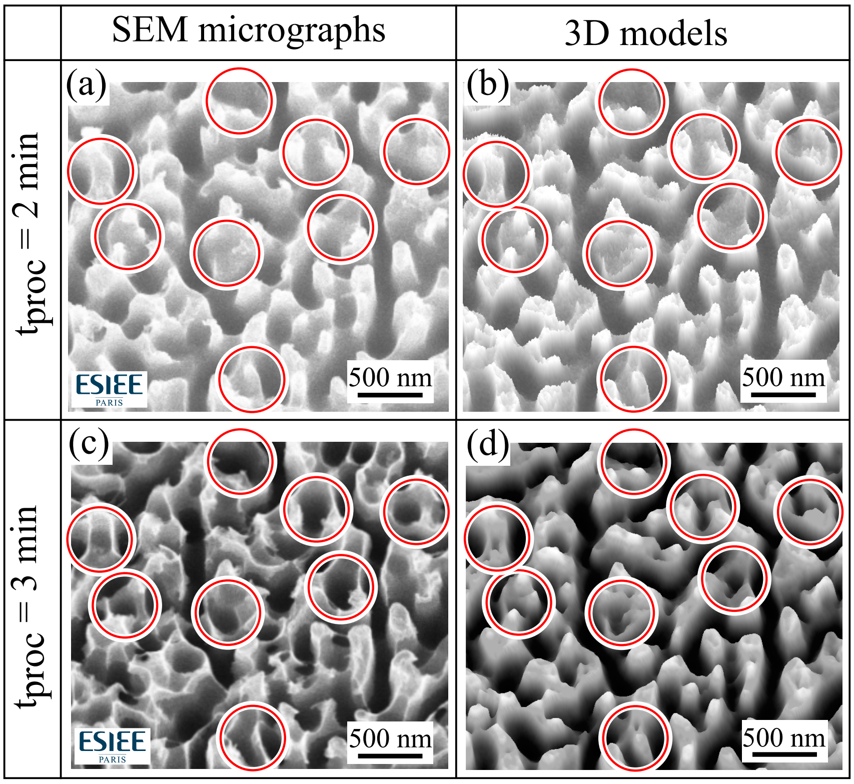

**Figure 4.10.** Time-lapse data showing the evolution of sample S04 between $t = 2$ min. and $t = 3$ min. of process time, for both simulation and experiment. 20° tilted view of: (a) initial time-lapse SEM and (b) three-dimensional reconstruction; (c) final time-lapse SEM (Temperature = -120°C, ICP power = 1000 W, bias voltage = -10 V, $O_2$ flow = 20 sccm, $SF_6$ flow = 200 sccm and pressure = 1.5 Pa) and (d) final time-lapse simulation ($v_{\mathrm{pf}} = 1.8$ nm/s, $v_{\mathrm{pe}} = 1.2$ nm/s and $v_{\mathrm{se}} = 30$ nm/s). Newly etched holes are highlighted with circles, showing good agreement between model and experiment.

these different processes can lead to the formation of BSi and the new etch fronts on top of previously formed mound structures. Figure 4.11 illustrates the different effects of the simulation model that lead to the BSi formation from planar structures. The observed phenomenology can be explained by the fact that the initial flat surface of the Si sample is unstable to hole formation under RIE since the etching of the passivation layer is anisotropic (ion bombardment), and thus unaffected by hole formation, whereas the passivation layer formation is hindered by diffusion at the bottoms of the holes. The bottoms of the holes therefore undergo reduced passivation, and hence the etching conditions there are effectively shifted downwards on the phase diagram of Figure 4.5, towards the uniform etching regime. Likewise, the tops of needles are over-passivated due to increased exposure to the diffusing passivating species, whereas the exposure to passivation etching species remains essentially unchanged. This pushes the effective etching condition for needle tops upwards on the phase diagram, resulting in slower (or no) etching. However, on a sample that has already developed the characteristic BSi topography, saddle points are the only areas where the effective passivation growth and etch rates are balanced, which allows the formation of new holes and explains the observed densification of the hole pattern with time.

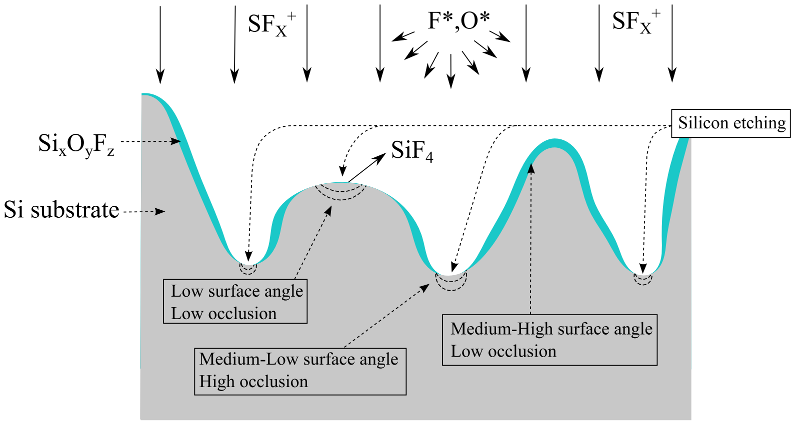

**Figure 4.11.** BSi formation mechanism

We also have tested the formation of new etch fronts in mathematically generated surfaces, where we clearly observe the preferential etching of the saddle areas due to the combination of high exposure and low surface angle (Figure 4.12).

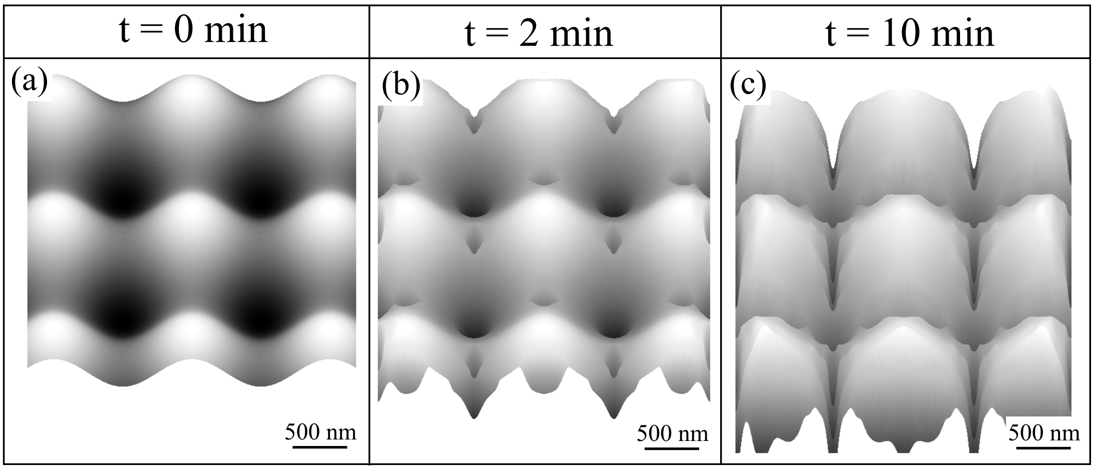

**Figure 4.12.** Formation of new etch fronts on saddle points on mathematically generated surface. (a) $t = 0$ min, (b) $t = 2$ min and (c) $t = 10$ min

This page intentionally left blank

# Chapter 5

# Design and development of a BSi solar cell

## Contents

In this Chapter we present the fabrication process workflow of a black silicon solar cell. The design is based on the analysis of previous works in the literature, the experience in Silicon microfabrication of ESYCOM's Lab CMM team and the "Laboratoire de Physique des Interfaces et Couches Minces" (LPICM) hosted by the Ecole Polytechnique.

The objective is to fabricate a BSi solar cell with enhanced power conversion efficiency (PCE) as a partial step to demonstrate the proof of concept of a self-cleaning solar cell. Such cell is achieved by integrating the BSi cell to a microfluidic system and taking advantage of BSi hydrophilic/hydrophobic properties.

## 5.1 Substrate characterization

Silicon substrates are acquired with the specifications described in Table 5.1.

**Table 5.1.** Si substrate specifications

| **Parameter** | **Value** | **Parameter** | **Value** |
|---|---|---|---|
| Material | PV-FZ* | Orientation | (1-0-0) +/- 1 |
| Type/Dopant | P/Bo | Resistivity (Ω cm) | 1-5 |
| Lifetime ($\mu$ sec) | $\geq$ 500 | Carbon (Atoms/cm$^3$) | $<$ 2.0 x $10^{16}$ |
| Oxygen (Atoms/cm$^3$) | $<$ 2.0 x $10^{16}$ | Diameter (mm) | 100 +/- 0.3 |
| Flat, Primary (mm) | SEMI standard | Flat, Secondary (mm) | SEMI standard |
| Thickness ($\mu$m) | 280 +/- 25 | Finish front side | Polished |
| Finish back side | Polished | Edge rounding | Yes, standard |
| TTV** ($\mu$m) | $\leq$ 12 | Bow*** ($\mu$m) | $\leq$ 30 |

*Float-Zone silicon

**Total thickness variation

***Deviation of the centre points between a wafer and its best fit referential plane

To verify the quality of the Si substrate for photovoltaic applications we measure its minority carrier (MC) lifetime after a passivation and annealing process. The method used to evaluate the MC lifetime consists of RF quasi-steady-state photoconductance (RS-QSSPC) measurements [101], which are performed at LPICM.

Two Si wafers (labelled A and B) are processed. We proceed to the Si surface passivation by the consecutive grow of a hydrogenated amorphous silicon carbide (a-SiC:H) layer and a hydrogenated amorphous silicon (a-Si:H) layer on both wafers by Plasma-enhanced chemical vapour deposition (PECVD). The process parameters are described in Table 5.2.

**Table 5.2.** Fabrication parameters for minority carrier lifetime measurement

| **Parameters** | **1$^{st.}$ layer (a-SiC:H)** | **2$^{nd.}$ layer (a-Si:H)** |
|---|---|---|
| SiH$_4$ flow (sccm) | 25 | 50 |
| CH$_4$ flow (sccm) | 50 | 0 |
| Power (W) | 1 | 1 |
| Pressure (mT) | 40 | 50 |
| Time (s) | 30 | 330 |
| Approx. layer thickness (nm) | 2.5 | 25 |
| Temperature (°C) | 200 | 200 |

After the wafer passivation step, we measure the minority carrier lifetime by the Radio Frequency Quasi-Steady-State Photoconductance RF-QSSPC method. Figure 5.1 shows the results of (MC) lifetime *vs.* minority carrier density of both samples.

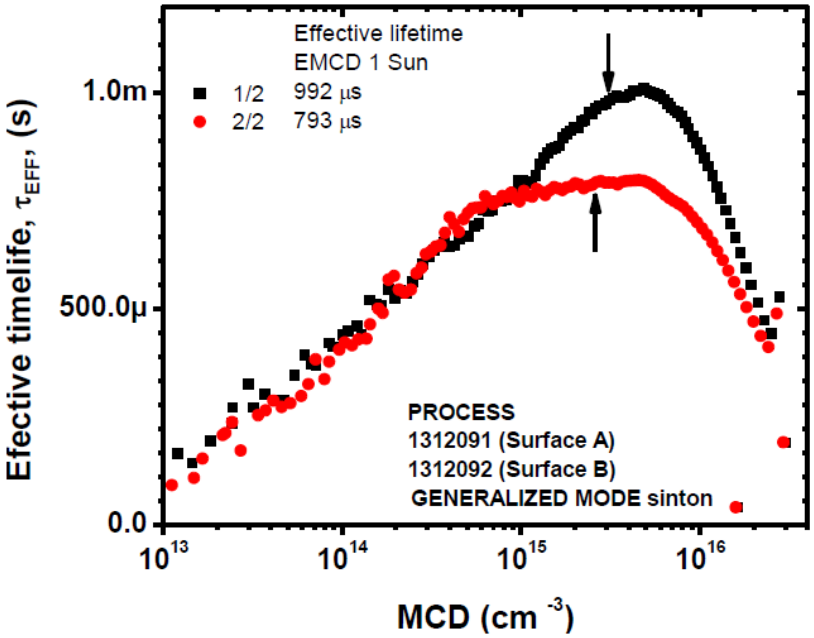

**Figure 5.1.** Minority carrier lifetime *vs.* minority carrier density for Si wafers samples A and B after passivation process. (Measurement performed at LPICM)

To further increase the MC lifetime, the Si wafers are annealed for 30 minutes in $N_2$ at 200°C, followed by a second MC lifetime measurement shown in Figure 5.2.

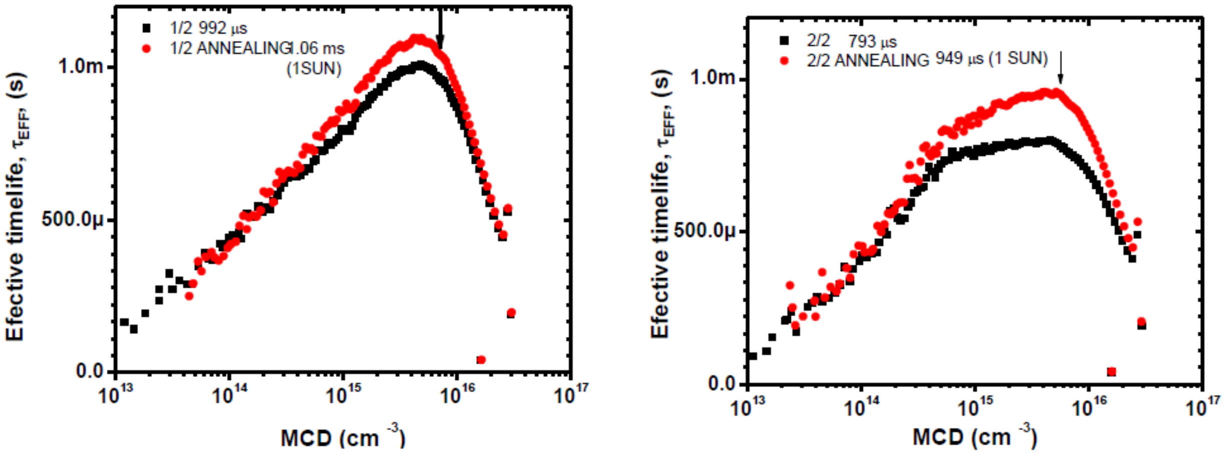

(a) (b)

**Figure 5.2.** Minority carrier lifetime *vs.* minority carrier density for Si wafers samples A (a) and B (b) after passivation and annealing process. (Measurement performed at LPICM)

From Figure 5.2 we observe that for a current density equivalent to 1 sun the effective MC lifetimes are 1.06 ms and 0.95 ms for samples A and B respectively, therefore the substrates are suitable for solar cell fabrication ($\geq 1$ ms).

## 5.2 Fabrication process description

The BSi solar cell fabrication process starts with the back surface doping followed by the front surface BSi patterning. Solar cells with different design parameters configurations, such as the average BSi structure height and the junction depth, are fabricated to determine their influence in the cell's performance. Three sets of solar cells are fabricated, from which two are patterned with BSi of different heights (500 nm and 1000 nm) and the third one is without BSi patterning. Each set consists of two cells with different junction depths (100 nm and 500 nm), as illustrated in Figure 5.3.

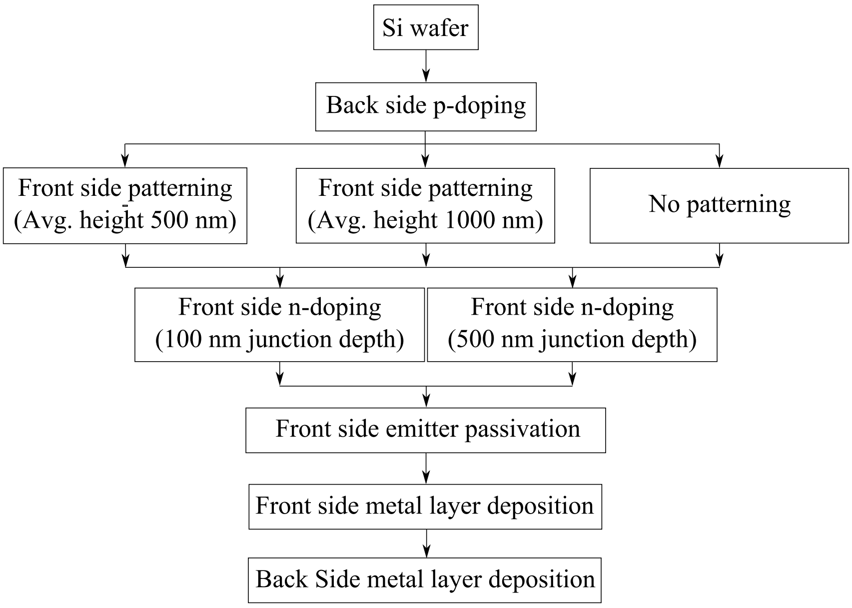

**Figure 5.3.** BSi solar cell fabrication process

Two wafers per configuration are used, each wafer consisting of four cells from which three are structured with BSi and one cell is planar (without the patterning step), for a total of eight wafers.

## 5.3 Masks description

Based on the previously described fabrication process, a mask is required to define the active areas of the patterned cells with BSi structures. Since each wafer will contain four cells from which three are patterned, the layout of the mask consists of three squares of size 2 x 2 cm as illustrated in Figure 5.4a.

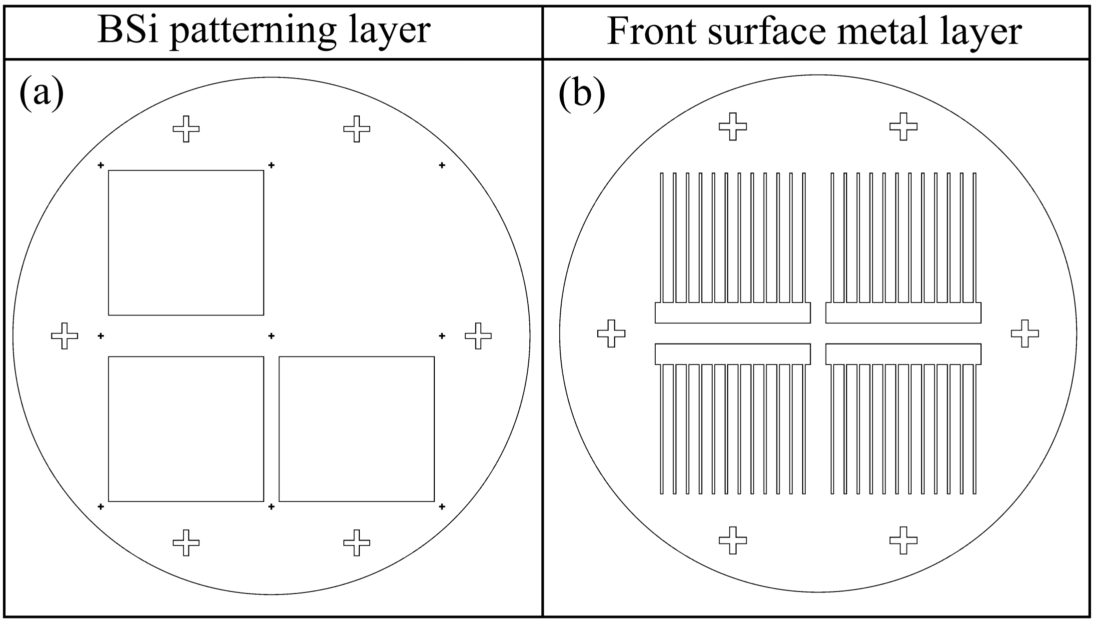

**Figure 5.4.** Layout of masks used in the BSi fabrication process: (a) BSi patterning area mask (b) Front surface metal layer mask

The second mask is used for the patterning of the front surface metal deposition step, consisting of 12 fingers with length 2 cm, width 0.5 mm and finger separation 2.5 mm, as illustrated in Figure 5.4b. These dimensions were obtain analytically by minimizing the power losses due to sheet and fingers resistance.

## 5.4 Steps performed

### 5.4.1 Back surface p-doping implantation and annealing

After the substrate characterisation, we proceed to the implantation of a p-doped layer on the back side of the wafers followed by a rapid thermal annealing (RTA) process. This layer allows creating a back surface field that reduces the effective rear surface recombination velocity [102].

Typical specifications of the p-doped layer used in solar cell (obtained from the literature [102]) comprise a sheet resistance of 90 $\Omega \cdot \Box$ and a thickness of 0.5 $\mu$m. In order to fabricate a p-doped layer with these specifications, calculations are made using a solar cell modelling software (PC1D), to determine the doping profile parameters such as peak doping and a depth factor by providing the substrate dopant and bulk resistivity. The calculations using PC1D show that, for a complementary error function (Erfc) profile shape, a peak doping of 1.6 x $10^{20}$ $\mathrm{cm}^{-3}$ and depth factor of 0.15 $\mu$m are required. Complementary ion implantation simulations (using SILVACO) are performed to determine the appropriate implantation parameters (such as ion energy and dose level) to achieve the required p-doped layer profile. (Simulations performed in LAAS-CNRS)

In order to verify the SILVACO simulations, a parametric study of the profile is performed by analysing the substrates with different dose levels using secondary ion mass spectroscopy (SIMS). Prior to the ion implantation, a sacrificial oxide layer is grown on the wafer to obtain a smoothly decreasing dopant concentration profile. The oxygen layer is obtained by dry thermal oxidation process at 1000°C.

Three silicon wafers (labelled 1, 4, and 8) with a 100 nm oxide layer are processed by boron implantation at three different doses: 3 x $10^{15}$, 5 x $10^{15}$ and 7 x $10^{15}$ atoms/cm$^2$ respectively. These wafers are then analysed by SIMS to have a feedback on their doping profile, the results, being shown in Figure 5.5, allow us to determine the dose level that provides the most appropriate profile (3 x $10^{15}$ atoms/cm$^2$).

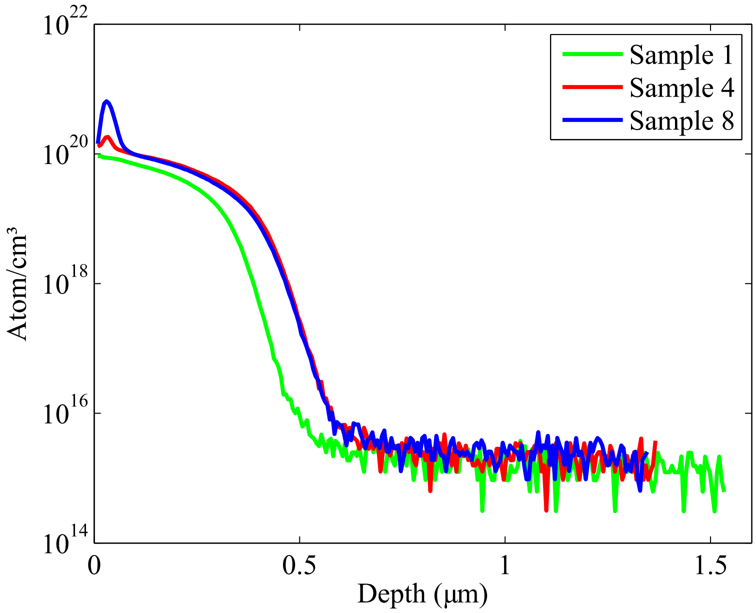

**Figure 5.5.** Si wafer doping level profiles obtained by SIMS of Silicon samples 1,4, and 8. (Measurement performed at LAAS-CNRS)

## 5.5 Unachieved steps

### 5.5.1 Front surface BSi etching

Followed by the back surface p-doping, a series of steps are applied to prepare the wafer for the front surface BSi etching such as: an increase of the oxide layer to a thickness of approx. 250 nm, used as a mask during the front surface n-doping step (Figure 5.6b); a 1 $\mu$m thick back side photoresist layer coating (Figure 5.6c); the top side oxide removal by HF wet etching (Figure 5.6d); and finally, a top side photolithography to create a 1.7 $\mu$m patterned mask that exposes the active area of the cells where BSi is going to be etched (Figure 5.6e).

After the preliminary steps, a Black Silicon etch is applied to the front surface of the samples (Figure 5.6f) using the cryo-DRIE parameters shown in Table 5.3.

### 5.5.2 Front surface PN junction fabrication

The PN junction fabrication on the BSi surface requires several preliminary steps such as: the removal of the previous coated photoresist by $O_2$ plasma etching (Figure 5.7b), the front surface

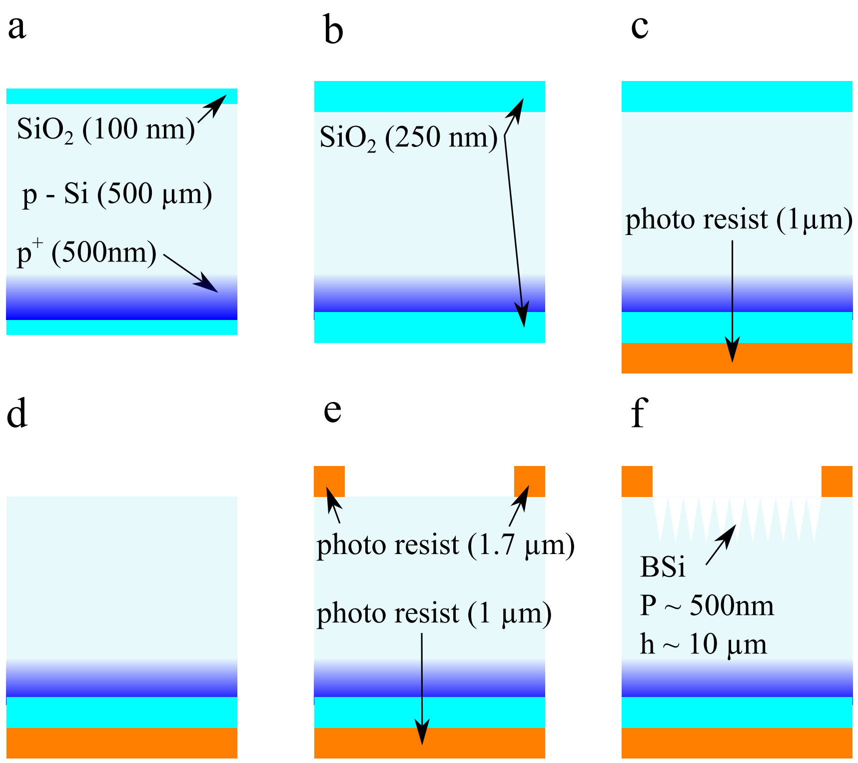

**Figure 5.6.** Si wafer process workflow for front surface BSi etching: (a) Si wafer with 100 nm oxide layer and back surface p-doping of approx. 500 nm, (b) oxide layer thickness increase by dry oxidation process to a desired thickness of approx. 250 nm, (c) back surface 1 $\mu$m thick photoresist coating, (d) front surface oxide layer removal by HF wet etching, (e) front surface patterned 1.7 $\mu$m thick photoresist coating and (f) front surface BSi etching by cryo-DRIE, to produce microstructures of approx. 10 $\mu$m of height and 500 nm of average spacing.

**Table 5.3.** BSi cryo-DRIE fabrication parameters

| **cryo-DRIE parameters** | **Values** |
|---|---|
| Temperature (°C) | -120 |
| ICP Power (W) | 1000 |
| Bias Voltage (V) | -10 |
| $O_2$ flow (sccm) | 10 |
| $SF_6$ flow (sccm) | 200 |
| Pressure (Pa) | 1.5 |
| Processing time (minutes) | 10 |

n-doping by $POCl_3$ diffusion (Figure 5.7c), the glass removal with HF wet etching (Figure 5.7d), and finally, the front surface passivation and annealing (Figure 5.7e). Two different values are considered for the n-doping thickness: 100 nm to dope only the BSi structure surfaces and 500 nm to dope through the entire BSi structures.

The exact procedure to perform a conformal passivation layer on the textured front surface is not yet defined. A possible method could consist of growing a conformal $Al_2O_3$ layer by atomic layer deposition (ALD).

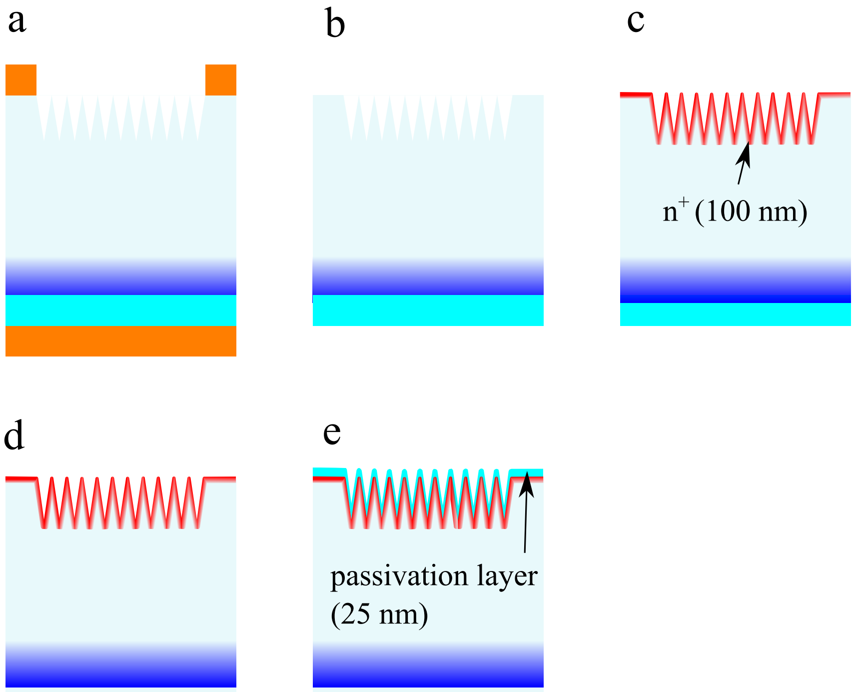

**Figure 5.7.** Si wafer process workflow for front surface n-doping and surface passivation and annealing: (a) Si wafer after BSi etching in front surface, (b) photoresist removal by $O_2$ plasma, (c) front surface n-doping by $POCl_3$ diffusion (d) glass removal by HF wet etching, (e) front surface passivation and annealing.

### 5.5.3 Front and back surface metallization

An Aluminium layer of approx. 1 $\mu$m is deposited on the front and back surfaces of the cell by evaporation or sputtering (Figure 5.8). A patterning on the front surface is performed using a shadow mask, being previously fabricated using the mask described in Figure 5.4b.

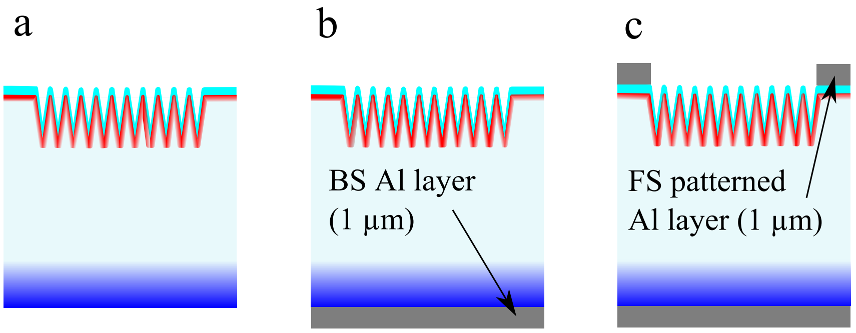

**Figure 5.8.** Si wafer process workflow for back and front surface metallization: (a) PV cell after front surface passivation and annealing, (b) Back surface metal deposition by evaporation or sputtering (∼1 $\mu$m) and (c) front surface patterned metal deposition by evaporation or sputtering with shadow mask (∼1 $\mu$m).

# Conclusions

In Chapter 2, by comparing the obtained 3D model reconstructions of BSi samples with their corresponding SEM micrographs at different viewing angles, we demonstrate that dual beam FIB-SEM nano-tomography can be used to reconstruct accurate topographies of complex samples with dense high aspect ratio features. This method removes the limitation on maximum aspect ratio that is inherent to all 3D reconstruction methods based on SEM image pixel conversion due to the limited dynamic range of the detectors. FIB-SEM nano-tomography provides extremely accurate information on the depth of deep narrow holes that are specific to BSi, at the cost of destroying the sample in the FIB etching process.

The error margin of the measurement of hole depth is equivalent to the SEM image acquisition interval, being $\sim$100 nm for our setup. Having accurate topographic parameters of BSi samples allowed us to better understand the relation between such structures and their optical properties as demonstrated in Chapter 3. Another advantage of this reconstruction method is that it provides an accurate measurement of the total surface area enhancement, showing that in the case of BSi it can reach values higher than 10. Such surfaces therefore may have important implications in manufacturing catalytic micro-reactors, where improved contact area can provide an important efficiency boost.

As an interesting observation, the analysis of the images obtained with the FIB-SEM tomography suggests that the BSi samples are formed through the bottom-up generation of a pattern of tapered cylindrical holes carved in the Si substrate at different depths as by a "nano-drill", corresponding to observations previously reported [21]. The actual silicon "needles" that are characteristic of BSi therefore represent the difference between the initial silicon wafer volume and the union of all the drilled holes volumes, and not the result of micro-masking, as was previously speculated [19].

In Chapter 3, we have presented modelling techniques of BSi samples to improve the simulated reflectance with respect to the one obtained by measurements. All techniques are based on statistical information of BSi 3D model reconstructions obtained by FIB-SEM tomography due to the dense agglomeration of high aspect ratio structures typical in BSi samples. The first technique, consisting of numerical simulations of unit cell structures based on regions of actual BSi topography, provides partial concordance with measurements at certain wavelength range but with different curve tendencies. Differences in the reflectance response between regions are attributed to the limited size of the simulated structure and the BSi heterogeneity.

The second modelling technique, based on a biperiodic equivalent structure consisting of a single shape, shows improved agreement of the simulated reflectances compared to measurements when the height distribution is similar to the global BSi height distribution (single inverted cone *vs.* cone shapes). In addition, improved concordance was obtained when the equivalent structure height is based on the global BSi height STD, compared with the height based on the global mean depth and the mean normal surface angle. This result suggests that by using the STD as structure height, it compensates the strong local variations of the mean height observed in the BSi topography.

In the third modelling technique, unit cells with 4 inverted cones are used in order to introduce variations of the structure height and diameter to break the periodicity of the single structure unit cell and therefore with greater resemblance to BSi topography. The results obtained consist in smoother reflectance responses with improved tendencies with respect to the ones observed in measurements, while the mean reflectance did not change due to the cells being designed with the same topographic parameters as the single structure unit cell. The multi-structure unit cell provides 8 degrees of freedom allowing to model unit cells having height distributions with greater similarity to the ones measured from BSi samples, which would imply further improvement in the reflectance matching.

The different multi-structured unit cell configurations ($1^{st.}$ and $2^{nd.}$ cases) provide about the same reflectance response with NRMSE with experimental measurements below 0.25% for wavelength range between 450 and 950 nm. The remaining fluctuations observed in the reflectance of the multi-structured unit cell denote the trade-off between cell simplicity and reflectance accuracy.

The specular reflectance results obtained from the multilayered media approximations, using both the Si–air ratio and the synthesized capacitance models, demonstrates that an improved agreement between simulations and measurements can be achieved when the silicon–air interface as a function of height is based on measurements of real BSi surfaces obtained by FIB nanotomography. By using the measured interface transition from silicon to air, the effect caused by the disordered distribution of the structures can be incorporated into this method providing improved agreement compared to the ones based on basic shapes such as an inverted pyramid.

The reduced average reflectance observed in simulations of multi-structure unit cells with respect to the single-structure cell at different AOI, suggests that surfaces having a disordered structure distribution with different dimensions such as BSi are preferable in cases where lower reflectance is required at different irradiation AOI than surfaces having perfectly organized structures with similar dimensions.

In Chapter 4, a combination of experimental data and modelling has allowed us to explain some of the properties of BSi, and to gain insight into the mechanisms underlying its formation by cryo-DRIE. We have shown that the observed evolution of BSi from a planar substrate can be accurately modelled by including the long-range effects of geometric occlusion (or self-shadowing). The resulting simulation model, corroborated with experimental observations, allowed us to create a phase diagram that indicates the combinations of control parameters giving rise to BSi formation, and their effect on the final BSi aspect ratio. The complex geometry of BSi, consisting of needles and holes of various heights and depths, is captured by the model and explains the exceptionally low reflectivity of BSi. The dynamics of BSi formation, including the early-stage development of new etch fronts at topographical saddle points, as well as the late-stage evolution of aspect ratio with process time, are correctly predicted by the model.

In the future, we plan to further automatise the 3D reconstruction method using parallel sample orientation, by making it more robust against errors in the edge detection such as the ones caused by the waterfall effect. In addition, this reconstruction technique can be further generalized to other structures surfaces different than BSi such as nanowires, porous materials, nanotubes, etc.

The unit cell modelling techniques presented in this manuscript used to obtain improved reflectances predictions, can be further extended to study the BSi behaviour in the infrared wavelengths suitable for applications such as thermal conversion and infrared sensors. Since we demonstrate that with BSi surfaces the interface reflectance is reduced in both directions, a possible application of BSi could be the improvement of light extraction from infrared LEDs.

We also plan to further develop the BSi formation model in order to integrate the cryo-DRIE parameters influence in the simulation model parameters. In addition, we plan to include several mechanisms present in cryo-DRIE that are not currently taken in account in the model such as the ion re-emissions and variations of the strength of the passivation layer based on cryogenic temperature. Another interesting objective is to integrate both BSi formation model and the reflectance prediction model into a single algorithm capable to provide the time evolution of both topography and reflectance based on the cryo-DRIE parameters.

In the scope of the thesis we originally planned to fabricate a BSi solar cell which would be subsequently integrated into a microfluidic system to demonstrate a new concept of a self-cleaning solar cell, taking advantage of BSi hydrophobic/hydrophilic properties. While due to time constraints the solar cell is not yet fabricated, several preliminary tests and a carefully studied fabrication process are presented in Chapter 5. In the future, we plan to fabricate the BSi cells, and measure the expected power conversion efficiency contribution caused by the presence of BSi, which also includes tests of PCE performance at different angles of incidence.

# Bibliography

[1] C. Wilkinson and M. Rahman, “Dry etching and sputtering,” *Philosophical Transactions of the Royal Society of London. Series A: Mathematical, Physical and Engineering Sciences*, vol. 362, no. 1814, pp. 125–138, 2004.

[2] T.-H. Her, R. J. Finlay, C. Wu, S. Deliwala, and E. Mazur, “Microstructuring of silicon with femtosecond laser pulses,” *Applied Physics Letters*, vol. 73, no. 12, pp. 1673–1675, 1998.

[3] J. Gittleman, E. Sichel, H. Lehmann, and R. Widmer, “Textured silicon: A selective absorber for solar thermal conversion,” *Applied Physics Letters*, vol. 35, no. 10, pp. 742–744, 1979.

[4] Y. Inomata, K. Fukui, and K. Shirasawa, “Surface texturing of large area multicrystalline silicon solar cells using reactive ion etching method,” *Solar energy materials and solar cells*, vol. 48, no. 1, pp. 237–242, 1997.

[5] C. Wu, C. Crouch, L. Zhao, J. Carey, R. Younkin, J. Levinson, E. Mazur, R. Farrell, P. Gothoskar, and A. Karger, “Near-unity below-band-gap absorption by microstructured silicon,” *Applied Physics Letters*, vol. 78, no. 13, pp. 1850–1852, 2001.

[6] S. Koynov, M. S. Brandt, and M. Stutzmann, “Black nonreflecting silicon surfaces for solar cells,” *Applied Physics Letters*, vol. 88, no. 20, p. 203107, 2006.

[7] J. E. Carey, C. H. Crouch, M. Shen, and E. Mazur, “Visible and near-infrared responsivity of femtosecond-laser microstructured silicon photodiodes,” *Optics Letters*, vol. 30, no. 14, pp. 1773–1775, 2005.

[8] M. Roumanie, C. Delattre, F. Mittler, G. Marchand, V. Meille, C. de Bellefon, C. Pijolat, G. Tournier, and P. Pouteau, “Enhancing surface activity in silicon microreactors: Use of black silicon and alumina as catalyst supports for chemical and biological applications,” *Chemical Engineering Journal*, vol. 135, pp. S317–S326, 2008.

[9] S. Y. Heo, J. K. Koh, G. Kang, S. H. Ahn, W. S. Chi, K. Kim, and J. H. Kim, “Bifunctional moth-eye nanopatterned dye-sensitized solar cells: Light-harvesting and self-cleaning effects,” *Advanced Energy Materials*, vol. 4, no. 3, 2014.

[10] S. Wahl, F. Marty, N. Pavy, B. Mercier, and D. E. Angelescu, “Sub-0.05° precision optofluidic dual-axis inclinometer,” in *Micro Electro Mechanical Systems (MEMS), 2014 IEEE 27th International Conference on*, pp. 797–800, IEEE, 2014.

[11] A. Torkkeli, J. Saarilahti, A. Haara, H. Harma, T. Soukka, and P. Tolonen, "Electrostatic transportation of water droplets on superhydrophobic surfaces," in *Micro Electro Mechanical Systems, 2001. MEMS 2001. The 14th IEEE International Conference on*, pp. 475–478, IEEE, 2001.

[12] N. Gaber, M. Malak, X. Yuan, K. N. Nguyen, P. Basset, E. Richalot, D. Angelescu, and T. Bourouina, "On the free-space gaussian beam coupling to droplet optical resonators," *Lab on a Chip*, vol. 13, no. 5, pp. 826–833, 2013.

[13] K. Nguyen, P. Basset, F. Marty, Y. Leprince-Wang, and T. Bourouina, "On the optical and morphological properties of microstructured black silicon obtained by cryogenic-enhanced plasma reactive ion etching," *Journal of Applied Physics*, vol. 113, no. 19, p. 194903, 2013.

[14] F.-Y. Zhu, Q.-Q. Wang, X.-S. Zhang, W. Hu, X. Zhao, and H.-X. Zhang, "3D nanostructure reconstruction based on the sem imaging principle, and applications," *Nanotechnology*, vol. 25, no. 18, p. 185705, 2014.

[15] L. Holzer and M. Cantoni, "Review of FIB-tomography," in *Nanofabrication using focused ion and electron beams: Principles and applications* (I. Utke, S. Moshkalev, and P. Russell, eds.), pp. 410–435, New York: Oxford University Press, 2012.

[16] M. Kroll, T. Käsebier, M. Otto, R. Salzer, R. Wehrspohn, E.-B. Kley, A. Tünnermann, and T. Pertsch, "Optical modeling of needle like silicon surfaces produced by an ICP-RIE process," in *Photonics for Solar Energy Systems III*, vol. 7725, pp. 772505–772505–10, 2010.

[17] C. Chiu, P. Yu, H. Kuo, C. Chen, T. Lu, S. Wang, S. Hsu, Y. Cheng, and Y. Chang, "Broadband and omnidirectional antireflection employing disordered GaN nanopillars," *Optics express*, vol. 16, no. 12, pp. 8748–8754, 2008.

[18] D. Lehr, M. Helgert, M. Sundermann, C. Morhard, C. Pacholski, J. P. Spatz, and R. Brunner, "Simulating different manufactured antireflective sub-wavelength structures considering the influence of local topographic variations," *Optics express*, vol. 18, no. 23, pp. 23878–23890, 2010.

[19] H. Jansen, M. de Boer, R. Legtenberg, and M. Elwenspoek, "The black silicon method: a universal method for determining the parameter setting of a fluorine-based reactive ion etcher in deep silicon trench etching with profile control," *Journal of Micromechanics and Microengineering*, vol. 5, no. 2, p. 115, 1995.

[20] G. Kumaravelu, M. Alkaisi, and A. Bittar, "Surface texturing for silicon solar cells using reactive ion etching technique," in *Photovoltaic Specialists Conference, 2002. Conference Record of the Twenty-Ninth IEEE*, pp. 258–261, IEEE, 2002.

[21] R. Dussart, X. Mellhaoui, T. Tillocher, P. Lefaucheux, M. Volatier, C. Socquet-Clerc, P. Brault, and P. Ranson, "Silicon columnar microstructures induced by an $SF_6/O_2$ plasma," *Journal of Physics D: Applied Physics*, vol. 38, no. 18, p. 3395, 2005.

[22] C. Teichert, J. MacKay, D. Savage, M. Lagally, M. Brohl, and P. Wagner, "Comparison of surface roughness of polished silicon wafers measured by light scattering topography, soft-x-ray scattering, and atomic-force microscopy," *Applied physics letters*, vol. 66, no. 18, pp. 2346–2348, 1995.

[23] A. A. Abouelsaood, S. El-Naggar, and M. Ghannam, “Shape and size dependence of the anti-reflective and light-trapping action of periodic grooves,” *Progress in Photovoltaics: Research and Applications*, vol. 10, no. 8, pp. 513–526, 2002.

[24] D. H. Raguin and G. M. Morris, “Subwavelength structured surfaces and their applications,” in *NASA CONFERENCE PUBLICATION*, pp. 87–97, DTIC Document, 1993.

[25] S. M. Pompea and R. P. Breault, “Black surfaces for optical systems,” *Handbook of Optics*, vol. 2, pp. 37–1, 2004.

[26] Z.-P. Yang, L. Ci, J. A. Bur, S.-Y. Lin, and P. M. Ajayan, “Experimental observation of an extremely dark material made by a low-density nanotube array,” *Nano letters*, vol. 8, no. 2, pp. 446–451, 2008.

[27] P. Spinelli, M. Verschuuren, and A. Polman, “Broadband omnidirectional antireflection coating based on subwavelength surface mie resonators,” *Nature communications*, vol. 3, p. 692, 2012.

[28] M. D. Kelzenberg, S. W. Boettcher, J. A. Petykiewicz, D. B. Turner-Evans, M. C. Putnam, E. L. Warren, J. M. Spurgeon, R. M. Briggs, N. S. Lewis, and H. A. Atwater, “Enhanced absorption and carrier collection in si wire arrays for photovoltaic applications,” *Nature materials*, vol. 9, no. 3, pp. 239–244, 2010.

[29] K. Nguyen, D. Abi-Saab, P. Basset, E. Richalot, F. Marty, D. Angelescu, Y. Leprince-Wang, and T. Bourouina, “Black silicon with sub-percent reflectivity: influence of the 3D texturization geometry,” in *Solid-State Sensors, Actuators and Microsystems Conference (TRANSDUCERS), 2011 16th International*, pp. 354–357, IEEE, 2011.

[30] H. Craighead, R. Howard, and D. Tennant, “Textured thin-film Si solar selective absorbers using reactive ion etching,” *Applied Physics Letters*, vol. 37, no. 7, pp. 653–655, 1980.

[31] T. Wells, M. El-Gomati, and J. Wood, “Low temperature reactive ion etching of silicon with $SF_6/O_2$ plasmas,” *Journal of Vacuum Science & Technology B: Microelectronics and Nanometer Structures*, vol. 15, no. 2, pp. 434–438, 1997.

[32] M. Schnell, R. Ludemann, and S. Schaefer, “Plasma surface texturization for multicrystalline silicon solar cells,” in *Photovoltaic Specialists Conference, 2000. Conference Record of the Twenty-Eighth IEEE*, pp. 367–370, IEEE, 2000.

[33] H. Jansen, M. De Boer, H. Wensink, B. Kloeck, and M. Elwenspoek, “The black silicon method. VIII. a study of the performance of etching silicon using $SF_6/O_2$-based chemistry with cryogenical wafer cooling and a high density ICP source,” *Microelectronics Journal*, vol. 32, no. 9, pp. 769–777, 2001.

[34] C. Lee, S. Y. Bae, S. Mobasser, and H. Manohara, “A novel silicon nanotips antireflection surface for the micro sun sensor,” *Nano letters*, vol. 5, no. 12, pp. 2438–2442, 2005.

[35] P. Garabedian, P. Pagnod-Rossiaux, and M. Puech, “Removable shield arrangement for ICP-RIE reactors,” 12 2002.

[36] R. Dussart, T. Tillocher, P. Lefaucheux, and M. Boufnichel, “Plasma cryogenic etching of silicon: from the early days to today’s advanced technologies,” *Journal of Physics D: Applied Physics*, vol. 47, no. 12, p. 123001, 2014.

[37] E. S. Kolesar Jr, V. M. Bright, and D. M. Sowders, “Optical reflectance reduction of textured silicon surfaces coated with an antireflective thin film,” *Thin Solid Films*, vol. 290, pp. 23–29, 1996.

[38] X. Li and P. Bohn, “Metal-assisted chemical etching in $HF/H_2O_2$ produces porous silicon,” *Applied Physics Letters*, vol. 77, no. 16, pp. 2572–2574, 2000.

[39] L. Ma, Y. Zhou, N. Jiang, X. Lu, J. Shao, W. Lu, J. Ge, X. Ding, and X. Hou, “Wide-band “black silicon” based on porous silicon,” *Applied physics letters*, vol. 88, no. 17, p. 171907, 2006.

[40] M. Lipiński, “Macroporous texturing of multicrystalline silicon for cells,” *Archives of Metallurgy and Materials*, vol. 53, pp. 185–187, 2008.

[41] K. Nishioka, S. Horita, K. Ohdaira, and H. Matsumura, “Antireflection subwavelength structure of silicon surface formed by wet process using catalysis of single nano-sized gold particle,” *Solar Energy Materials and Solar Cells*, vol. 92, no. 8, pp. 919–922, 2008.

[42] H. M. Branz, V. E. Yost, S. Ward, K. M. Jones, B. To, and P. Stradins, “Nanostructured black silicon and the optical reflectance of graded-density surfaces,” *Applied Physics Letters*, vol. 94, no. 23, p. 231121, 2009.

[43] C. H. Crouch, J. E. Carey, J. M. Warrender, M. J. Aziz, E. Mazur, and F. Y. Génin, “Comparison of structure and properties of femtosecond and nanosecond laser-structured silicon,” *Applied Physics Letters*, vol. 84, no. 11, pp. 1850–1852, 2004.

[44] M. Shen, C. H. Crouch, J. E. Carey, and E. Mazur, “Femtosecond laser-induced formation of submicrometer spikes on silicon in water,” *Applied Physics Letters*, vol. 85, no. 23, pp. 5694–5696, 2004.

[45] M. Shen, J. E. Carey, C. H. Crouch, M. Kandyla, H. A. Stone, and E. Mazur, “High-density regular arrays of nanometer-scale rods formed on silicon surfaces via femtosecond laser irradiation in water,” *Nano letters*, vol. 8, no. 7, pp. 2087–2091, 2008.

[46] A. Krotkus, K. Grigoras, V. Pačebutas, I. Barsony, E. Vazsonyi, M. Fried, J. Szlufcik, J. Nijs, and C. Levy-Clement, “Efficiency improvement by porous silicon coating of multicrystalline solar cells,” *Solar Energy Materials and Solar Cells*, vol. 45, no. 3, pp. 267–273, 1997.

[47] S. A. Boden and D. M. Bagnall, “Bio-mimetic nanostructured surfaces for near-zero reflection sunrise to sunset,” in *INTERNATIONAL SOLAR ENERGY SOCIETY UK SECTION-CONFERENCE-C*, vol. 88, p. 59, 2007.

[48] H. Sai, H. Fujii, K. Arafune, Y. Ohshita, Y. Kanamori, H. Yugami, and M. Yamaguchi, “Wide-angle antireflection effect of subwavelength structures for solar cells,” *Japanese journal of applied physics*, vol. 46, no. 6R, p. 3333, 2007.

[49] A. Burgers, C. Tool, J. Hylton, A. Weeber, A. Verholen, J. Gardeniers, M. de Boer, and M. Elwenspoek, "Silicon solar cells textured by reactive ion etching and processed with screen printing," in *2nd Photovoltaic World Conf., Vienna, Austria*, 1998.

[50] B. M. Damiani, R. Ludemann, D. S. Ruby, S. Zaidi, and A. Rohatgi, "Development of RIE-textured silicon solar cells," in *Photovoltaic Specialists Conference, 2000. Conference Record of the Twenty-Eighth IEEE*, pp. 371–374, IEEE, 2000.

[51] J. Yoo, G. Yu, and J. Yi, "Black surface structures for crystalline silicon solar cells," *Materials Science and Engineering: B*, vol. 159, pp. 333–337, 2009.

[52] J.-M. Shim, H.-W. Lee, K.-Y. Cho, J.-K. Seo, J.-S. Kim, E.-J. Lee, J.-Y. Choi, D.-J. Oh, J.-E. Shin, J.-S. Kim, *et al.*, "17.6% conversion efficiency multicrystalline silicon solar cells using the reactive ion etching with the damage removal etching," *International Journal of Photoenergy*, vol. 2012, 2012.

[53] E. Garnett and P. Yang, "Light trapping in silicon nanowire solar cells," *Nano letters*, vol. 10, no. 3, pp. 1082–1087, 2010.

[54] S. Jeong, M. D. McGehee, and Y. Cui, "All-back-contact ultra-thin silicon nanocone solar cells with 13.7% power conversion efficiency," *Nature communications*, vol. 4, 2013.

[55] J. Oh, H.-C. Yuan, and H. M. Branz, "An 18.2%-efficient black-silicon solar cell achieved through control of carrier recombination in nanostructures," *Nature nanotechnology*, vol. 7, no. 11, pp. 743–748, 2012.

[56] M. Otto, M. Kroll, T. Käsebier, R. Salzer, A. Tünnermann, and R. B. Wehrspohn, "Extremely low surface recombination velocities in black silicon passivated by atomic layer deposition," *Applied Physics Letters*, vol. 100, no. 19, p. 191603, 2012.

[57] A. Burgers, J. Bultman, C. Beneking, W. Nositschka, O. Voigt, and H. Kurz, "Silicon solar cells textured by reactive ion etching with natural lithography," in *Proc. 16th Euro. Photovoltaic Solar Energy Conf. Glasgow, U.K*, pp. 1427–1430, 2000.

[58] J. Yoo, I. Parm, U. Gangopadhyay, K. Kim, S. Dhungel, D. Mangalaraj, and J. Yi, "Black silicon layer formation for application in solar cells," *Solar energy materials and solar cells*, vol. 90, no. 18, pp. 3085–3093, 2006.

[59] H.-C. Yuan, V. E. Yost, M. R. Page, P. Stradins, D. L. Meier, and H. M. Branz, "Efficient black silicon solar cell with a density-graded nanoporous surface: Optical properties, performance limitations, and design rules," *Applied Physics Letters*, vol. 95, no. 12, p. 123501, 2009.

[60] M. A. Sheehy, L. Winston, J. E. Carey, C. M. Friend, and E. Mazur, "Role of the background gas in the morphology and optical properties of laser-microstructured silicon," *Chemistry of Materials*, vol. 17, no. 14, pp. 3582–3586, 2005.

[61] M. Steglich, D. Lehr, S. Ratzsch, T. Käsebier, F. Schrempel, E.-B. Kley, and A. Tünnermann, "An ultra-black silicon absorber," *Laser & Photonics Reviews*, vol. 8, no. 2, pp. L13–L17, 2014.

[62] C. Black, K. Guarini, K. Milkove, S. Baker, T. Russell, and M. Tuominen, “Integration of self-assembled diblock copolymers for semiconductor capacitor fabrication,” *Applied Physics Letters*, vol. 79, no. 3, pp. 409–411, 2001.

[63] W.-C. Feng, C.-W. Hsu, H.-C. Liu, and G.-J. Wang, “A cost effective and highly sensitive glucose biosensor based on a 3D silicon nanowire array electrode,” in *Design, Test, Integration and Packaging of MEMS/MOEMS (DTIP), 2014 Symposium on*, pp. 114–118, IEEE, 2014.

[64] Y.-L. Deng and Y.-J. Juang, “Black silicon SERS substrate: Effect of surface morphology on SERS detection and application of single algal cell analysis,” *Biosensors and Bioelectronics*, vol. 53, pp. 37–42, 2014.

[65] G. Scotti, P. Kanninen, T. Kallio, and S. Franssila, “Symmetric silicon micro fuel cell with porous electrodes,” in *Solid-State Sensors, Actuators and Microsystems Conference, 2009. TRANSDUCERS 2009. International*, pp. 1401–1404, IEEE, 2009.

[66] M. Mehran, Z. Sanaee, M. Abdolahad, and S. Mohajerzadeh, “Controllable silicon nanograss formation using a hydrogenation assisted deep reactive ion etching,” *Materials Science in Semiconductor Processing*, vol. 14, no. 3, pp. 199–206, 2011.

[67] C.-H. Choi and C.-J. Kim, “Large slip of aqueous liquid flow over a nanoengineered superhydrophobic surface,” *Physical review letters*, vol. 96, no. 6, p. 066001, 2006.

[68] V. Jokinen, L. Sainiemi, and S. Franssila, “Complex droplets on chemically modified silicon nanograss,” *Advanced Materials*, vol. 20, no. 18, pp. 3453–3456, 2008.

[69] G. Sun, T. Gao, X. Zhao, and H. Zhang, “Fabrication of micro/nano dual-scale structures by improved deep reactive ion etching,” *Journal of Micromechanics and Microengineering*, vol. 20, no. 7, p. 075028, 2010.

[70] M. Stubenrauch, M. Fischer, C. Kremin, S. Stoebenau, A. Albrecht, and O. Nagel, “Black silicon—new functionalities in microsystems,” *Journal of Micromechanics and Microengineering*, vol. 16, no. 6, p. S82, 2006.

[71] H. K. Elminir, A. E. Ghitas, R. Hamid, F. El-Hussainy, M. Beheary, and K. M. Abdel-Moneim, “Effect of dust on the transparent cover of solar collectors,” *Energy conversion and management*, vol. 47, no. 18, pp. 3192–3203, 2006.

[72] M. Mani and R. Pillai, “Impact of dust on solar photovoltaic (pv) performance: research status, challenges and recommendations,” *Renewable and Sustainable Energy Reviews*, vol. 14, no. 9, pp. 3124–3131, 2010.

[73] J. Goldstein, D. E. Newbury, D. C. Joy, C. E. Lyman, P. Echlin, E. Lifshin, L. Sawyer, and J. R. Michael, *Scanning electron microscopy and X-ray microanalysis*. Springer, 2003.

[74] J. Stampfl, S. Scherer, M. Gruber, and O. Kolednik, “Reconstruction of surface topographies by scanning electron microscopy for application in fracture research,” *Applied Physics A*, vol. 63, no. 4, pp. 341–346, 1996.

[75] M. Ritter and P. Midgley, "A practical approach to test the scope of FIB-SEM 3D reconstruction," in *Journal of Physics: Conference Series*, p. 012081, IOP Publishing, 2010.

[76] L. Holzer, F. Indutnyi, P. Gasser, B. Münch, and M. Wegmann, "Three-dimensional analysis of porous $BaTiO_3$ ceramics using FIB nanotomography," *Journal of Microscopy*, vol. 216, no. 1, pp. 84–95, 2004.

[77] R. Bansal, A. Kubis, R. Hull, and J. Fitz-Gerald, "High-resolution three-dimensional reconstruction: A combined scanning electron microscope and focused ion-beam approach," *Journal of Vacuum Science & Technology B*, vol. 24, no. 2, pp. 554–561, 2006.

[78] A. Deinega, I. Valuev, B. Potapkin, and Y. Lozovik, "Minimizing light reflection from dielectric textured surfaces," *JOSA A*, vol. 28, no. 5, pp. 770–777, 2011.

[79] C.-H. Sun, P. Jiang, and B. Jiang, "Broadband moth-eye antireflection coatings on silicon," *Applied Physics Letters*, vol. 92, no. 6, p. 061112, 2008.

[80] K. Han and C.-H. Chang, "Numerical modeling of sub-wavelength anti-reflective structures for solar module applications," *Nanomaterials*, vol. 4, no. 1, pp. 87–128, 2014.

[81] K. Nguyen, D. Abi-Saab, P. Basset, E. Richalot, M. Malak, N. Pavy, F. Flourens, F. Marty, D. Angelescu, Y. Leprince-Wang, and T. Bourouina, "Study of black silicon obtained by cryogenic plasma etching: approach to achieve the hot spot of a thermoelectric energy harvester," *Microsystem Technologies*, vol. 18, no. 11, pp. 1807–1814, 2012.

[82] Y.-P. Zhao, J. T. Drotar, G.-C. Wang, and T.-M. Lu, "Roughening in plasma etch fronts of Si (100)," *Physical review letters*, vol. 82, no. 24, p. 4882, 1999.

[83] J. H. Yao and H. Guo, "Shadowing instability in three dimensions," *Physical Review E*, vol. 47, no. 2, p. 1007, 1993.

[84] J. T. Drotar, Y.-P. Zhao, T.-M. Lu, and G.-C. Wang, "Surface roughening in shadowing growth and etching in 2+ 1 dimensions," *Physical Review B*, vol. 62, no. 3, p. 2118, 2000.

[85] M. Pelliccione, T. Karabacak, C. Gaire, G.-C. Wang, and T.-M. Lu, "Mound formation in surface growth under shadowing," *Physical Review B*, vol. 74, no. 12, p. 125420, 2006.

[86] H. Anzai, M. Saikawa, Y. Naito, and T. Mizumoto, "The equivalent representation of pyramidal absorbers and its application to the analysis of electromagnetic wave absorber's characteristics," in *Electromagnetic Compatibility, 1995. Symposium Record. 1995 IEEE International Symposium on*, pp. 563–567, IEEE, 1995.

[87] D. A. Clugston and P. A. Basore, "Pc1d version 5: 32-bit solar cell modeling on personal computers," in *Photovoltaic Specialists Conference, 1997., Conference Record of the Twenty-Sixth IEEE*, pp. 207–210, IEEE, 1997.

[88] P. J. Frey and P.-L. George, *Maillages: applications aux éléments finis.* Hermès Science Publications, 1999.

[89] J. Orloff, L. Swanson, and M. Utlaut, *High Resolution Focused Ion Beams: FIB and its Applications: The Physics of Liquid Metal Ion Sources and Ion Optics and Their Application to Focused Ion Beam Technology.* Springer, 2003.

[90] J. M. Palmer, "The measurement of transmission, absorption, emission, and reflection," in *Handbook of Optics*, vol. 2, McGraw-Hill, New York, 1995.

[91] OceanOptics, "Products catalog." http://www.oceanoptics.com, 2012.

[92] J. Maxwell Garnett, "Colours in metal glasses, in metallic films, and in metallic solutions. ii," *Philosophical Transactions of the Royal Society of London. Series A, Containing Papers of a Mathematical or Physical Character*, pp. 237–288, 1906.

[93] R. Hull, *Properties of Crystalline Silicon.* INSPEC, 1999.

[94] S. Mostarshedi, E. Richalot, and O. Picon, "Semi-infinite reflection model of a multilayered dielectric through equivalent permittivity calculation," *Microwave and Optical Technology Letters*, vol. 51, no. 2, pp. 290–294, 2009.

[95] S. J. Orfanidis, *Electromagnetic waves and antennas.* Rutgers University, 2002.

[96] Y. Ouattara, S. Mostarshedi, E. Richalot, J. Wiart, and O. Picon, "Near-and far-field models for scattering analysis of buildings in wireless communications," *Antennas and Propagation, IEEE Transactions on*, vol. 59, no. 11, pp. 4229–4238, 2011.

[97] K. N. Nguyen, *Étude et caractérisation des propriétés d'absorption électromagnétique du silicium micro/nano-structuré.* PhD thesis, Université Paris-Est, 2012.

[98] L. Sainiemi, *Cryogenic deep reactive ion etching of silicon micro and nanostructures.* PhD thesis, Helsinki University of Technology, 2009.

[99] X. Mellhaoui, *Mécanismes physico-chimiques dans le procédé de gravure plasma du Silicium.* PhD thesis, Université d'Orléans, 2006.

[100] B. E. Deal and A. Grove, "General relationship for the thermal oxidation of silicon," *Journal of Applied Physics*, vol. 36, no. 12, pp. 3770–3778, 1965.

[101] R. A. Sinton and A. Cuevas, "Contactless determination of current–voltage characteristics and minority-carrier lifetimes in semiconductors from quasi-steady-state photoconductance data," *Applied Physics Letters*, vol. 69, no. 17, pp. 2510–2512, 1996.

[102] J. Nelson, *The physics of solar cells*, vol. 57. World Scientific, 2003.

# Appendix A

# Black Silicon Formation Matlab Code

In this document we describe the Matlab program developed for the BSi formation simulation presented in Chapter 4 with the parameters values used to simulate the structures from polished Si surfaces.

The program consists in one main procedure file and several function files to accomplish specific tasks, which are described in the following Sections.

## A.1 Main procedure (BSi_sim.m)

The main procedure of the BSi formation simulation program includes the global steps of the BSi formation mechanism. It starts by assigning the input parameters values, followed by processing the Si input substrate according to the established process time, and finalizes by storing the obtained BSi surface in a file.

The function files required by the main procedure are the following:

- Fourier filter function (F_filter.m)
- Gaussian filter function (G_filter.m)
- Automatic bi-dimensional mesh grid function (Mesh_grid.m)
- Surface occlusion calculation function (Occlusion.m)
- Surface normal angle calculation function (Surf_norm_circ.m)
- Surface plot visualization function (Surf_plot.m)
- Symmetry boundaries function (Sym_bound.m)
- Surface height scaling function (Z_scale.m)

The input parameters required by the program are the following:

- Initial silicon surface bi-dimensional array (ZSI_0)
- Initial passivation layer thickness bi-dimensional array (ZPL_0)
- Passivation layer formation rate in micrometre per second (v_pf)
- Passivation layer etching rate in micrometres per second (v_pe)
- Silicon etching rate in micrometres per second (v_se)
- Maximum passivation layer thickness in micrometres (Z_max)
- Process time in minutes (t_proc)
- Step time duration in seconds (delta_t)
- Occlusion radius evaluation length in pixels (O_margin)
- Normal surface angle evaluation length in pixels (N_margin)
- Gaussian filter size in pixels (gf_size)
- Gaussian filter standard deviation (gf_sigma)
- Passivation layer formation Fourier filter size in pixels (ff_pf)
- Passivation layer etching Fourier filter size in pixels (ff_pe)
- Silicon etching Fourier filter size in pixels (ff_se)
- Passivation layer formation linear function slope (alpha_pf)
- Passivation layer formation linear function intercept (beta_pf)
- Passivation layer etching linear function slope (alpha_pe)
- Passivation layer etching linear function intercept (beta_pe)
- Silicon etching linear function slope (alpha_se)
- Silicon etching linear function intercept (beta_se)
- Planar Si surface roughness amplitude (na)
- Visualization tilt angle (theta)
- Si surface size in micrometres (ss)
- Si surface pixel resolution (res)
- Option to select same or different Si surface seed (option)

The output parameters given by the program are the following:

- Final silicon surface bi-dimensional array (ZSI_1)
- Final passivation layer thickness bi-dimensional array (ZPL_1)

A commented version of the main procedure file (bsi_sim.m) to simulate BSi formation from polished Si substrate is shown below:

```
% Simulation parameters used to form BSi sample shown in Chapter 5:
v_pf = 0.0025; v_pe = 0.003; v_se = 0.03; Z_max = 0.03; t_proc = 10;
delta_t = 10; O_margin = 52; N_margin = 15; gf_size = 3; gf_sigma = 0.5;
ff_pf = 200;  ff_pe = 100;  ff_se = 200;  alpha_pf = 0; beta_pf = 2.4;
alpha_pe = 0; beta_pe = 1; alpha_se = 0.3; beta_se = 0.7; na = 0.0005;
theta = 30;   ss = 3;       res = 0.01;   option = 1;

% Main procedure:

% Convert t_proc to seconds
tproc_sec = t_proc * 60;
% Determine Si surface array size
dim = ss / res;
% Set same or different seed
if option, rng(’default’); end
% Determine initial Si substrate
ZSI_0 = rand(dim) .* na;
% Reset initial passivation layer thickness
ZPL_0 = zeros(dim);
% Repeat until t_proc is reached
while tproc_sec >= 0
   % Filter Si surface
   ZSI_0 = G_filter(ZSI_0, gf_size, gf_sigma);
   % Filter passivation layer
   ZPL_0 = G_filter(ZPL_0, gf_size, gf_sigma);
   % Calculate occlusion of Si surface
   O = Occlusion(ZSI_0, O_margin, res);
   % Apply linear function to calculate new passivation layer formed
   O_pf = ( alpha_pf + beta_pf * O );
   % Reset negative values
   O_pf( O_pf < 0 ) = 0;
   % Calculate new linear passivation layer formed
   Pf = O_pf * v_pf;
   % Filter noise from new linear passivation layer formed
   Pf = F_filter(Pf, ff_pf);
   % Calculate linear value of pre-existing passivation layer thickness
   ZPL_0a = -Z_max / 2 .* log(2 ./ (ZPL_0 ./ Z_max + 1) - 1);
   % Add new passivation layer to previous passivation layer
   ZPL_0b = ZPL_0a + Pf * delta_t;
   % Calculate effective thickness based on self-limiting passivation grow
   ZPL_0c = Z_max * (2 ./ (1 + exp(-ZPL_0b ./ (Z_max ./ 2))) - 1);
   % Calculate surface normal angle of silicon surface
   N = Surf_norm_circ(ZSI_0, N_margin, res);
   % Apply linear function to calculate amount of passivation etch
```

```matlab
N_pe = ( alpha_pe + beta_pe * N );
% Reset negative numbers
N_pe(N_pe < 0) = 0;
% Subtract silicon consumed based on amount of new passivation formed
ZSI_0a = ZSI_0 - (ZPL_0c - ZPL_0) ./ N_pe;
% Calculate amount of passivation layer etch
Pe = N_pe * v_pe;
% Filter noise from amount of passivation layer etch
Pe = F_filter(Pe, ff_pe);
% Calculate remaining passivation layer thickness
ZPL_1 = ZPL_0c - Pe * delta_t;
% Store ZPL_1 value for later use
ZPL_1a = ZPL_1;
% Find areas where passivation layer was completely removed
ind = (ZPL_1a < 0);
% Reset negative passivation layer values
ZPL_1a(ind) = 0;
% If passivation layer etching rate is greater than 0
if v_pe ~= 0
   % Calculate delta time of silicon etching
   dt_se = abs(ZPL_1) ./ v_pe;
   % Reset values where passivation layer was not completely removed
   dt_se(~ind) = 0;
else
   % Set delta time of silicon etching to 1
   dt_se = ones(size(ZPL_1a));
   % Reset values where passivation layer is present
   dt_se(ZPL_1 ~= 0) = 0;
end
% Apply linear function to calculate amount of silicon etch
O_se = ( alpha_se + beta_se * O );
% Reset negative values
O_se(O_se < 0) = 0;
% Calculate amount of silicon etched
Se = O_se * v_se;
% Filter noise from amount of silicon etched
Se = F_filter(Se, ff_se);
% Subtract amount of silicon etched from Si substrate
ZSI_1 = ZSI_0a - (dt_se .* Se);
% If initial step create visualization window
if t_proc-tproc_sec/60 == 0
   % Create visualization window
   h_prev = Surf_plot(ZSI_0, res, 30, 1, 0, t_proc - tproc_sec / 60);
   pause(5);
end
% Update visualization window
h_prev = Surf_plot(ZSI_1, res, 30, 0, h_prev, t_proc - tproc_sec / 60);
% Update initial parameters for following step
ZSI_0 = ZSI_1;
ZPL_0 = ZPL_1a;
% Subtract delta time from process timer
tproc_sec = tproc_sec - delta_t;
% Save results of each step
```

```
   save(['pt', num2str((t_proc - tproc_sec / 60) * 1e2, '%04.0f'), '.mat'],...
      'ZSI_1');
end
% Save final result
save(['vpe', num2str(v_pe * 1e5, '%03.0f'), '_vpf', num2str(v_pf * 1e5,...
   '%03.0f'), '.mat'], 'ZSI_1');
```

## A.2 Surface occlusion calculation function (Occlusion.m)

This function calculates the occlusion of each point of a bi-dimensional array. It returns an array with same dimensions as the input surface array with occlusion values. Symmetry boundaries are applied to avoid edge effects.

This function requires the Symmetry boundaries function (sym_bound.m). The input parameters consist of the input bi-dimensional array (S0), the occlusion evaluation length in pixels (margin), the pixel size value (res) and the differential azimuth angle for occlusion evaluation (delta_phi), which is set by default to 10°.

```
function [O] = Occlusion(S0, margin, res, delta_phi)
   if (nargin < 4), dphi = 10; end
   dim1 = size(S0, 1);
   dim2 = size(S0, 2);
   S0exp = Sym_bound(S0, margin);
   oo = 1;
   angle = zeros(dim1, dim2, 360/dphi);
   for phi = 0:dphi:359
      for r = 1:margin
         xx = round(r * cosd(phi));
         yy = round(r * sind(phi));
         if r == 1
            box = S0exp(margin+1+yy:dim1+margin+yy,...
               margin+1+xx:dim2+margin+xx);
            dz = box - S0;
            tan0 = dz / r;
         else
            box = S0exp(margin+1+yy:dim1+margin+yy,...
               margin+1+xx:dim2+margin+xx);
            dz = box - S0;
            tan1 = dz / r;
            ind = find(tan0 < tan1);
            tan0(ind) = tan1(ind);
         end
      end
   angle(:,:,oo) = 90 - atand(tan0 / res);
   oo = oo + 1;
```

```
  end
  O=(1 - cosd(sum(angle, 3) .* dphi / 360));
end
```

## A.3 Normal angle calculation function (Surf_norm_circ.m)

This function calculates the surface normal angle of each point of a bi-dimensional array. It returns an array with same dimensions as the input surface array with the normal angle values. Symmetry boundaries are applied to avoid edge effects.

This function requires the Symmetry boundaries function (sym_bound.m) and the Surface height scaling function (Z_scale.m). The input parameters consist of the input bi-dimensional array (S0), the surface normal angle evaluation length in pixels (margin) and the pixel size value (res).

```
function [N] = Surf_norm_circ(S0, margin, res)
  dim1=size(S0,1);
  dim2=size(S0,2);
  S0exp = Sym_bound(S0, margin);
  Disco = fspecial('disk', margin);
  Disco = Z_scale(Disco);
  Disco = im2bw(Disco, 0.25);
  ind = find(Disco);
  [xbox,ybox] = meshgrid(0 : res : res * (margin * 2));
  Xbox=[ones(length(ind), 1), xbox(ind), ybox(ind)];
  N=zeros(dim1, dim2);
  U = [0, 0, 1];
  for n1 = 1:dim1
    for n2 = 1:dim2
      Ybox = S0exp(n1 : n1 + 2 * margin, n2 : n2 + 2 * margin);
      Ybox = Ybox(ind);
      beta = (Xbox' * Xbox)^-1 * Xbox' * Ybox;
      V = [beta(2, 1), beta(3, 1), 1];
      N(n1,n2) = dot(U,V)/(sqrt(U(1)^2+U(2)^2+U(3)^2)*...
        sqrt(V(1)^2+V(2)^2+V(3)^2));
    end
  end
end
```

## A.4 Additional functions

### A.4.1 Surface mesh grid function (Mesh_grid.m)

This function automatically creates a Cartesian bi-dimensional grid based on a surface array size and the pixel size value. The input parameters are the bi-dimensional array (z) and the pixel size value (res). The output parameters are the X and Y axes mesh grid arrays.

```
function [X, Y] = Mesh_grid(z, res)
   dimy = size(z, 1);
   dimx = size(z, 2);
   ssy = dimy * res;
   ssx = dimx * res;
   if mod(dimx,2)
      x = -(ssx-res)/2:res:(ssx-res)/2;
   else
      x = -ssx/2+res/2:res:ssx/2-res/2;
   end
   if mod(dimy,2)
      y = (ssy-res)/2:-res:-(ssy-res)/2;
   else
      y = ssy/2-res/2:-res:-ssy/2+res/2;
   end
   [X,Y] = meshgrid(x,y);
end
```

### A.4.2 Surface array scaling function (Z_scale.m)

This function process an input bi-dimensional array (a) producing an output array (b) with same dimensions and its values scaled between 0 and 1.

```
function [b] = Z_scale(a)
   a = a - min(a(:));
   b = a ./ max(a(:));
end
```

### A.4.3 Gaussian filter function (G_filter.m)

This function applies a Gaussian filter to an input bi-dimensional array (S0), and the result is stored in an output variable (S1). Symmetry boundaries are applied to avoid edge effects, therefore requiring the symmetry boundary function (Sym_bound.m). Additional input parameters values are required such as the Gaussian filter size in pixels (siz) and the Gaussian filter standard deviation (sigma).

```
function [S1] = G_filter(S0, siz, sigma)
   dim1 = size(S0, 1);
   dim2 = size(S0, 2);
   S0exp = Sym_bound(S0, siz);
   H = fspecial('gaussian', siz, sigma);
   S0a = imfilter(S0exp ,H ,'conv', 'circular');
   S1 = S0a(siz + 1 : dim1 + siz, siz + 1 : dim2 + siz);
end
```

### A.4.4 Fourier filter function (F_filter.m)

This function applies a low-pass Fourier filter to a bi-dimensional array (a) and storing the result in an output variable (b). The function requires the surface array scaling function (Z_scaling.m) and the mask size input parameter in pixels (siz).

```
function [b] = F_filter(a, siz)
   a = fft2(a);
   a = fftshift(a);
   h1 = fspecial('gaussian', size(a, 1), siz / 6);
   h1 = Z_scale(h1);
   a = a .* h1;
   a = ifftshift(a);
   b = real(ifft2(a));
end
```

### A.4.5 Symmetry boundaries function (Sym_bound.m)

This function process an input bi-dimensional array (S0) creating an expanded array (S0exp) consisting of the original array with symmetry boundaries. The size of the boundary is controlled by the boundary length variable (margin).

```
function [S0exp] = Sym_bound(S0, margin)
    dim1 = size(S0,1);
    dim2 = size(S0,2);
    S0exp = zeros(dim1*3-2,dim2*3-2);
    S0exp(1:dim1-1,1:dim2-1) = rot90(S0(2:dim1,2:dim2),2);
    S0exp(1:dim1-1,dim2:2*dim2-1) = flipud(S0(2:dim1,:));
```

```
    S0exp(1:dim1-1,2*dim2:3*dim2-2) = rot90(S0(2:dim1,1:dim2-1),2);
    S0exp(dim1:2*dim1-1,1:dim2-1) = fliplr(S0(1:dim1,2:dim2));
    S0exp(dim1:2*dim1-1,dim2:2*dim2-1) = S0;
    S0exp(dim1:2*dim1-1,2*dim2:3*dim2-2) = fliplr(S0(1:dim1,1:dim2-1));
    S0exp(2*dim1:3*dim1-2,1:dim2-1) = rot90(S0(1:dim1-1,2:dim2),2);
    S0exp(2*dim1:3*dim1-2,dim2:2*dim2-1) = flipud(S0(1:dim1-1,1:dim2));
    S0exp(2*dim1:3*dim1-2,2*dim2-1+1:3*dim2-2) = rot90(S0(1:dim1-1,1:dim2-1),2);
    S0exp = S0exp(dim1-margin:2*dim1+margin-1,dim2-margin:2*dim2+margin-1);
end
```

### A.4.6 Surface plot visualization function (Surf_plot.m)

This function creates a surface plot window of a bi-dimensional array (z). It allows updating the surface data in the same window in order to produce an animated visualization of the surface evolution in time.

This function requires the mesh grid function (mesh_grid.m) and several input parameters such as the pixel size (res), the visualization tilt angle (angle) the control variable (init) that allows to choose between a new window or update the surface of a previous created window, the previous window plot handle (h_prev) and the process time parameter (t_proc) for visualization.

```
function [h0] = Surf_plot(z, res, angle, init, h_prev, time)
   [x, y] = Mesh_grid(z, res);
   if init == 1
      set1 = {'DefaultTextFontname','Times New Roman',...
         'DefaultAxesFontname','Times New Roman'};
      hh = figure(set1{:});
      set(gcf, 'color', [1 1 1]);
      set(gca, 'FontSize', 14);
      axis off
      zoom off
      daspect([1 1 1]);
      hold on
      colormap gray
      view(0, 90 - angle);
      zlim([-3.5 0]);
      xlabel('\mum');
      ylabel('\mum');
      zlabel('\mum');
      pause(0.0001);
   else
      hh = 0;
      delete(h_prev);
   end
   h0 = surf(x,y,z,'EdgeColor','none');
   shading interp;
```

```
    title(['t = ',num2str(time,'%10.2f'),' min.']);
    pause(0.0001);
end
```

**Résumé:**

Dans le cadre de cette thèse, nous présentons un aperçu général des surfaces du silicium micro et nano structurées, appelées silicium noir (BSi), et obtenues par la gravure ionique réactive cryogénique (cryo-DRIE). Ces surfaces auto-générées peuvent être fabriquées dans un procédé en une seule étape fournissant de grandes surfaces à faible réflectivité sur une large gamme de longueurs d'onde et d'angles d'incidence. Nous examinons plusieurs aspects des surfaces du BSi, incluant les méthodes de fabrication, les applications, les méthodes de caractérisation de sa topographie, les techniques de modélisation pour les simulations optiques, et les mécanismes de croissance. Nous développons ensuite trois principales contributions que cette thèse apporte à l'état de l'art : une meilleure compréhension de la topographie du BSi, la modélisation de son comportement optique et un aperçu de ses mécanismes de formation. Nous développons une nouvelle technique de caractérisation topographique du BSi, utilisant un faisceau ionique localisé dans le plan de l'échantillon pour réaliser une nanotomographie qui reproduit les détails de structure avec une précision inférieure au micron. Nous présentons ensuite différentes méthodes de modélisation de cellules unitaires du BSi basées soit sur la topographie de la surface réelle obtenue, ou sur des formes géométriques équivalentes qui sont statistiquement représentatives de la topographie du BSi. Nous sommes capables d'obtenir une excellente concordance entre les simulations et les données expérimentales. Nous présentons également un modèle capable de simuler toute l'évolution de la surface du BSi allant d'un substrat plat jusqu'à sa topographie entièrement développée, en concordance avec des données obtenues expérimentalement. On produit un diagramme de phase qui saisit les combinaisons de paramètres responsables de la formation du BSi. Nous sommes en mesure de reproduire dans notre modèle, un certain nombre d'effets subtils qui mènent à la densification du motif observé, responsable de la formation du BSi pendant cryo-DRIE.

**Mots clés:** *silicium noir, gravure ionique réactive, nanostructure, simulation optique, modélisation de la croissance*

**Abstract:**

In this thesis, we present a general overview of silicon micro and nanostructured surfaces, known as black silicon (BSi), fabricated with cryogenic deep reactive ion etching (cryo-DRIE). These self-generated surfaces can be fabricated in a single step procedure and provide large surfaces with reduced reflectance over a broad range of wavelengths and angles of incidence. We review several aspects of BSi surfaces, such as its fabrication methods, applications, topography characterization methods, modelling techniques for optical simulations, and growth mechanisms. We then develop three main contributions that this thesis brings to the state of the art: a better understanding of BSi topography, modelling of its optical behaviour and insights into its formation mechanism. We develop a novel BSi topographical characterisation technique which is based on in-plane focused ion beam nanotomography and can reproduce sample details with submicron accuracy. We then present different methods of modelling BSi unit cells, based either on real surface topography obtained using the aforementioned technique, or on equivalent geometric shapes that are statistically representative for BSi topography. We are capable to obtain excellent matching between simulations and experimental data. Finally, we present an experimentally-backed phenomenological model that is capable of simulating the entire evolution of a surface from a planar substrate to fully developed BSi topography. We produce a phase diagram which captures the parameter combinations responsible for BSi formation. We also observe experimentally, and are able to reproduce within our model, a number of subtle effects that lead to the observed pattern densification that is responsible for BSi formation during cryo-DRIE.

**Keywords:** *black silicon, reactive ion etching, nanostructure, optical simulation, growth modelling*